
Masters

Engineering

2008-04-01

Numerical Prediction of Primary and Secondary Flows in a Ranque-Hilsch Vortex Tube

Ronan Oliver

Technological University Dublin, ronan.oliver@tudublin.ie

Follow this and additional works at: <https://arrow.tudublin.ie/engmas>



Part of the [Mechanical Engineering Commons](#)

Recommended Citation

Oliver, R. (2008). *Numerical prediction of primary and secondary flows in a Ranque-Hilsch vortex tube*. Masters dissertation. Technological University Dublin. doi:10.21427/D7ZG8R

This Theses, Masters is brought to you for free and open access by the Engineering at ARROW@TU Dublin. It has been accepted for inclusion in Masters by an authorized administrator of ARROW@TU Dublin. For more information, please contact arrow.admin@tudublin.ie, aisling.coyne@tudublin.ie, vera.kilshaw@tudublin.ie.

**NUMERICAL PREDICTION OF PRIMARY
AND SECONDARY FLOWS IN A
RANQUE – HILSCH VORTEX TUBE**

Ronán Oliver, B.Eng.

A thesis submitted to the Dublin Institute of Technology
in fulfilment of the requirements for the Degree of

MASTERS OF PHILOSOPHY
IN
MECHANICAL ENGINEERING

Department of Mechanical Engineering
School of Mechanical and Transport Engineering
Dublin Institute of Technology

April 2008

Supervisors of Research: Dr Fergal Boyle, Dr David Kennedy

Advisory Supervisor: Dr Anthony Reynolds

Abstract

The primary aim of this project is to obtain a fundamental understanding of the fluid dynamics and thermodynamics of the primary and secondary flows in a Ranque-Hilsch Vortex Tube (RHVT). These flows are highly complex and are three-dimensional, compressible, and viscous in nature. To obtain an understanding of these, a state-of-the-art Computational Fluid Dynamics (CFD) software package is applied for flow prediction with advanced turbulence models, and is employed to predict the primary and secondary flows in a RHVT. The models that are used include: the $k-\varepsilon$ model, the SST model by Menter, and the Reynolds Stress Model. The results from the turbulence models are analysed and compared to establish how accurate they are at computing this type of flow field.

In this CFD study of the RHVT, the flow fields and temperature outputs are investigated. This study begins with the appropriate selection of experimental results from a range of authors for similar vortex tubes. These results are collated and a three dimensional model of a similar experimental RHVT is drawn, upon which an unstructured tetrahedral mesh is developed using the CAD and meshing facilities of the CFD package respectively. This model is developed in such a way that components of the RHVT could be easily adjusted in size in order to carry out small scale parametric studies of the vortex tube.

The analysis moves on to the correct stipulation of suitable and accurate boundary conditions. Once a set of appropriate and realistic boundary conditions is established, the flow fields within the RHVT are captured. Initially the $k - \varepsilon$ turbulence model is utilised to perform a mesh element density convergence study with the cold static and total temperature outputs of the RHVT as the measured criteria. Once mesh independent results are established, additional turbulence models such as the SST model by Menter and the Reynolds Stress model are run on this mesh to ascertain the performance of each turbulence model. When the optimum turbulence model is ascertained an investigation was carried out into the source of heat migration in the RHVT. This began by varying the tube geometry, i.e. the cold outlet diameter, and analysing its influence on the presence of secondary flow and therefore the influence of secondary flow on the heat transfer within the RHVT. An additional

analysis of the work due to friction within the vortex tube is also performed in order to verify the presence of such work within the RHVT.

Finally a recommendation is made within the conclusion of this thesis as to a method of how to take the study of work due to friction within the vortex tube forward for further analysis.

Declaration

I certify that this thesis which I now submit for examination for the award of MPhil in Mechanical Engineering, is entirely my own work and has not been taken from the work of others save and to the extent that such work has been cited and acknowledged within the text of my work.

This thesis was prepared according to the regulations for postgraduate study by research of the Dublin Institute of Technology and has not been submitted in whole or in part for an award in any other Institute or University.

The work reported on in this thesis conforms to the principles and requirements of the Institute's guidelines for ethics in research.

The Institute has permission to keep, to lend or to copy this thesis in whole or in part, on condition that any such use of the material of the thesis be duly acknowledged.

Signature *Seán Oliver* Date *29/04/08*

Acknowledgements

I wish to thank those who have helped me with my work in completing this study including my colleagues in the Department of Mechanical Engineering and the Engineering Faculty itself which supplied all funds necessary for computer hardware/software and college facilities. Considerable appreciation goes to the Embark Initiative managed by the IRCSET as part of the National Development Plan, Ireland 2000 – 2006, who provided the scholarship grant paramount to the viability of this work. Special gratitude goes to Dr. Fergal Boyle who conceived the project idea and provided substantial direction and support throughout. Finally to my support base of Ann-Marie, my family and friends without whom none of this would have been possible.

Nomenclature

A	area	m^2
C	constant (arbitrary)	
c_p	specific heat capacity at constant pressure	J/kgK
c_v	specific heat capacity at constant volume	J/kgK
d_c	diameter of the cold outlet	m
D	diameter of the RHVT	m
f	frequency	kHz
h_o	total specific enthalpy	J/kg
h_s	static specific enthalpy	J/kg
i	internal energy per unit mass	J/kg
k	turbulent kinetic energy	$(m/s)^2$
L	length of the RHVT	m
L	reference length for the Reynolds Number	m
m	mass	kg
\dot{m}	mass flux	kg/s
n	outward surface vector	
P	pressure	N/m^2
Pr	Prandtl number	
Pr_t	turbulent Prandtl number	
Q	heat energy	J
\dot{Q}	heat flux	W
r, θ	polar coordinates	
R	universal gas constant	J/molK
Re	Reynolds number	
s	entropy	J/kgK
T_o	total temperature	K
T_s	static temperature	K
t	time	s
\mathbf{U}	velocity vector	m/s
u	x - component of the velocity vector (axial velocity)	m/s

u'	fluctuating x - component of the velocity vector	m/s
U	mean x - component of the velocity vector	m/s
V	volume	m^3
v	y - component of the velocity vector (tangential velocity)	m/s
v'	fluctuating y - component of the velocity vector	m/s
V	mean y - component of the velocity vector	m/s
W	mean z - component of the velocity vector	m/s
W	work (for Section 1.5.1 only)	J
\dot{W}	work flux	W
\ddot{W}	work flux per unit area	W/m^2
w	z - component of the velocity vector (radial velocity)	m/s
w'	fluctuating z - component of the velocity vector	m/s
x,y,z	cartesian coordinates	
Z	height above a datum level	m

Greek Symbols

Γ	diffusivity	m^2/s
Γ_{eff}	effective turbulent diffusivity	m^2/s
Γ_t	turbulent diffusivity	m^2/s
γ	ratio of specific heat capacities	
ε	rate of turbulent dissipation per unit mass	m^2/s^3
λ	thermal conductivity	W/mK
μ	viscosity	kg/ms
μ_c	cold gas fraction	
μ_{eff}	effective turbulent viscosity	kg/ms
μ_t	turbulent viscosity	kg/ms
ν_t	turbulent kinematic viscosity	m^2/s
ρ	density	kg/m^3
τ	viscous shear stress	N/m^2
τ^R	Reynolds shear stress	N/m^2
ω	inverse time scale associated with turbulence	1/s

Subscripts

c	cold outlet of Ranque-Hilsch Vortex Tube
-----	--

<i>h</i>	hot outlet of Ranque-Hilsch Vortex Tube
<i>in</i>	inlet of Ranque-Hilsch Vortex Tube
<i>i,j</i>	tensor notation
<i>ip</i>	integration point
<i>s</i>	surface region of integration

Superscripts

<i>o</i>	old time level
----------	----------------

Table of Contents

Abstract.....	i
Declaration.....	iii
Acknowledgements.....	iv
Nomenclature.....	v
Table of Contents.....	viii
List of Figures.....	xi
List of Tables.....	xvii
1 The Ranque – Hilsch Vortex Tube.....	1
1.1 Introduction.....	1
1.2 The Ranque - Hilsch Vortex Tube.....	1
1.3 Ranque’s Contribution.....	2
1.4 Hilsch’s Contribution.....	4
1.5 Fundamentals of the Ranque-Hilsch Vortex Tube.....	5
1.5.1 Thermodynamics of the Ranque – Hilsch Vortex Tube.....	5
1.5.2 Fluid Dynamics of the Ranque – Hilsch Vortex Tube.....	8
1.6 Commercial Vortex Tubes.....	10
1.6.1 Spot Cooling Applications.....	11
1.6.2 Spot Heating Applications.....	12
1.6.3 Experimental Ranque-Hilsch Vortex Tube Equipment.....	12
1.6.4 Personal Air Conditioners.....	13
1.7 Current Energy Separation Theory.....	13
1.8 Summary.....	13
2 Literature Review.....	14
2.1 Introduction.....	14
2.2 Velocity Profiles in the Ranque – Hilsch Vortex Tube.....	14
2.3 Experimental Proof of Secondary Flow.....	16
2.3.1 Secondary Flow working as a Refrigeration Cycle.....	17
2.4 Frictional Heat Transfer.....	18
2.4.1 Flow of Work in the Ranque – Hilsch Vortex Tube.....	20
2.5 Acoustic Streaming in Vortex Tubes.....	20

2.6	Previous CFD Studies.....	23
2.7	Summary.....	24
3	Computational Fluid Dynamics.....	25
3.1	Introduction.....	25
3.2	The History of CFD.....	25
3.2.1	Uses of CFD.....	25
3.3	Navier – Stokes Equations.....	26
3.4	Governing Equations of CFD.....	27
3.4.1	Discretisation of the Governing Equations of CFD.....	28
3.5	Boundary Conditions.....	32
3.6	Solution Strategy of the ANSYS CFX 10 Solver.....	33
3.7	CFD Methodology.....	34
3.7.1	Creating the Geometry and Mesh.....	34
3.7.2	Definition of the Physics of the Fluid Flow.....	35
3.7.3	Solving for a Solution of the Fluid Flow.....	35
3.7.4	Post-Processing of the Results.....	35
3.8	Summary.....	36
4	CFD Analysis of the RHVT.....	37
4.1	Introduction.....	37
4.2	Procedure Adopted.....	37
4.3	Utilised Experimental Results.....	38
4.4	RHVT CFD Model.....	39
4.5	Boundary Conditions.....	42
4.5.1	Nozzle Inlet.....	42
4.5.2	Cold Outlet.....	42
4.5.3	Hot Outlet.....	43
4.5.4	Periodic Boundaries.....	43
4.6	Mesh Convergence Study.....	44
4.7	Turbulence Model Performance.....	49
4.7.1	Thermal Performance.....	49
4.7.2	Reynolds Stress Model Performance.....	56
4.7.3	Flowfield Performance.....	56
4.8	Summary.....	58
5	Investigation into the Mode of Heat Transfer.....	59

5.1	Introduction	59
5.2	Secondary Flow	59
5.2.1	Relationship to Temperature Output	60
5.2.2	Thermodynamic Influence of Secondary Flow	62
5.3	Rotary Work due to Friction	64
6	Conclusions	67
6.1	Recommendations for Future Work	68
7	References	69
A	Turbulence and Turbulence Modelling	71
A.1	Introduction	71
A.2	Turbulence	71
A.3	Turbulence Modelling	74
A.3.1	Boussinesq Hypothesis	75
A.3.2	Prandtl's Mixing Length Model	76
A.3.3	The $k - \epsilon$ Model	78
A.3.4	The $k - \omega$ Model	83
A.3.5	SST Model by Menter	84
A.3.6	Reynolds Stress Equation Models	86
A.4	Summary	88
B	CFD Analysis of Flat Plate Boundary Layers	90
B.1	Introduction	90
B.2	Boundary Layers	90
B.2.1	The Laminar Boundary Layer Equations	91
B.2.2	Turbulent Flat Plate Boundary Layer	97
B.3	CFD Solution	98
B.3.1	The Flow Domain	98
B.3.2	The Mesh	100
B.3.3	The Boundary Conditions	103
B.3.4	Convergence	105
B.4	The Results	107
B.5	Summary	109
C	Solver Output File for Mesh No. 2	110
C.1	Introduction	110

List of Figures

Fig. 1-1: Typical Operation of a Modern Counter-Flow RHVT [3].	2
Fig. 1-2: Cross-Section of Ranque's Vortex Tube Design [4].	2
Fig. 1-3: Commercial RHVT by Exair [5].	3
Fig. 1-4: Cross Section of a Uniflow RHVT [7].	4
Fig. 1-5: System Boundary applied to RHVT.	5
Fig. 1-6: Complete Ranque-Hilsch Vortex Tube System Including Compressed Air Supply [9].	7
Fig. 1-7: Variation of $\Delta T_{o,c}$ with μ_c for typical RHVT [10,11].	8
Fig. 1-8: Axial velocity streamline plot and graphs of tangential and axial velocity and their distribution along the central axis of the RHVT.	9
Fig. 1-9: Cold Air Gun by ITW Vortec [13].	11
Fig. 1-10: Control Cabinet RHVT by Exair [5].	11
Fig. 1-11: Explanation of Control Cabinet Cooling RHVT by Exair [5].	12
Fig. 1-12: Experimental RHVT Equipment, by P.A. Hilton Ltd [14].	12
Fig. 1-13: Personal Air Conditioner by ITW Vortec [13].	13
Fig. 2-1: Experimental Set-Up to measure flows internal to the RHVT [7].	15
Fig. 2-2: Experimental results of internal normalised tangential velocities at normalised radial and axial locations within a RHVT for $P_{in}=6\text{bar}$, $L/D=65$, and $\mu_c=0.4$ [7].	15
Fig. 2-3: Experimental results of internal normalised axial velocities at normalised radial and axial locations within a RHVT for $P_{in}=6\text{bar}$, $L/D=65$ and $\mu_c=0.4$ [7].	16
Fig. 2-4: Primary and Secondary circulation within the RHVT [15].	16
Fig. 2-5: Heat pump cycle within a RHVT [16].	17
Fig. 2-6: Schematic Flow Pattern of a RHVT.	19
Fig. 2-7: Forced Vortex and Free Vortex.	19
Fig. 2-8: The spectral density of the acoustic signal obtained by Kurosaka [24].	21
Fig. 2-9: Graph illustrating the behaviour of the energy separation, and the acoustical output from Kurosaka's tube as the excitation frequency is increased [24].	22
Fig. 2-10: Streamline plot of axial velocity on the central axis of a RHVT with $d_c/D = 0.417$ near the cold end exit zone [29].	24

Fig. 2-11: Flow pattern near cold end exit for $d_c/D = 0.323$ showing secondary circulation flow; (b) flow pattern near cold end exit for $d_c/D = 0.58$ showing no secondary circulation flow [29].	24
Fig. 3-1: Cell Vertex Finite Volume Scheme [33].	29
Fig. 3-2: Isolated mesh element and its associated integration points [33].	30
Fig. 3-3: Solver solution procedure for a steady, compressible, turbulent flow with thermal gradients [33].	33
Fig. 3-4: Software modules available in ANSYS CFX 10 [35].	34
Fig. 4-1: Experimental results of internal normalised tangential and axial velocities at normalised radial locations from [7] at the inlet region within the RHVT.	39
Fig. 4-2: Isometric view of the CFD model of the 3D RHVT with two inlet nozzles, cold outlet and a conical hot outlet.	40
Fig. 4-3: Plan view of the CFD model of the 3D RHVT with two inlet nozzles, cold outlet and a conical hot outlet.	40
Fig. 4-4: Hot outlet end view of the CFD model of the 3D RHVT with two inlet nozzles and a conical hot outlet.	41
Fig. 4-5: Cold outlet end view of the CFD model of the 3D RHVT with two inlet nozzles and the cold outlet.	41
Fig. 4-6: Utilised CFD model of the halved RHVT highlighting the rotational periodicity property of a vortex tube with an even number inlet nozzles and the periodic faces on the central axis of the RHVT.	43
Fig. 4-7: Flow chart of the procedure used to ascertain a mesh independent solution.	44
Fig. 4-8: Axial view of Mesh No. 1 from the mesh convergence study of Table 4-2.	46
Fig. 4-9: Axial view of Mesh No. 5 from the mesh convergence study of Table 4-2.	46
Fig. 4-10: Zoomed view of Mesh No. 5 when viewed from the right hand side of the RHVT as shown in Fig: 4-9.	46
Fig. 4-11: Isometric view of Mesh No. 5 when viewed from the left hand side of the RHVT as shown in Fig: 4-9.	47
Fig. 4-12: CFD mesh convergence study for a RHVT similar to [10] and [11]. The graph shows the variance of the cold outlet total temperature drop ($T_{o,c} - T_{in,c}$) and cold static temperature difference ($T_{s,c} - T_{in,c}$) versus the mesh density in the form of	

the average control volume at each node. The targeted computed total temperature drop from the experimental results of [10] and [11] are highlighted along with the utilised RAM for each CFD run.	48
Fig. 4-13: Total temperature contour plot along the central axis of the RHVT, for Mesh No.1 containing 1,705 nodes, $\mu_c=0.4$, $P_{in}=2\text{Bar}$ and $L/D=10$, using the $k - \varepsilon$ turbulence model.	50
Fig. 4-14: Total temperature contour plot along the central axis of the RHVT, for Mesh No.5 containing 1,522,948 nodes, $\mu_c=0.4$, $P_{in}=2\text{Bar}$ and $L/D=10$, using the $k - \varepsilon$ turbulence model.	50
Fig. 4-15: Total temperature contour plot along the central axis of the RHVT, for Mesh No.5 containing 1,522,948 nodes, $\mu_c=0.4$, $P_{in}=2\text{Bar}$ and $L/D=10$, using the SST turbulence model.	50
Fig. 4-16: Static temperature contour plot along the central axis of the RHVT, for Mesh No.1 containing 1,705 nodes, $\mu_c=0.4$, $P_{in}=2\text{Bar}$ and $L/D=10$, using the $k - \varepsilon$ turbulence model.	51
Fig. 4-17: Static temperature contour plot along the central axis of the RHVT, for Mesh No.5 containing 1,522,948 nodes, $\mu_c=0.4$, $P_{in}=2\text{Bar}$ and $L/D=10$, using the $k - \varepsilon$ turbulence model.	51
Fig. 4-18: Static temperature contour plot along the central axis of the RHVT, for Mesh No.5 containing 1,522,948 nodes, $\mu_c=0.4$, $P_{in}=2\text{Bar}$ and $L/D=10$, using the SST turbulence model.	51
Fig. 4-19: Density contour plot along the central axis of the RHVT, for Mesh No.1 containing 1,705 nodes, $\mu_c=0.4$, $P_{in}=2\text{Bar}$ and $L/D=10$, using the $k - \varepsilon$ turbulence model.	52
Fig. 4-20: Density contour plot along the central axis of the RHVT, for Mesh No.5 containing 1,522,948 nodes, $\mu_c=0.4$, $P_{in}=2\text{Bar}$ and $L/D=10$, using the $k - \varepsilon$ turbulence model.	52
Fig. 4-21: Density contour plot along the central axis of the RHVT, for Mesh No.5 containing 1,522,948 nodes, $\mu_c=0.4$, $P_{in}=2\text{Bar}$ and $L/D=10$, using the SST turbulence model.	52
Fig. 4-22: Axial velocity contour plot along the central axis of the RHVT, for Mesh No.1 containing 1,705 nodes, $\mu_c=0.4$, $P_{in}=2\text{Bar}$ and $L/D=10$, using the $k - \varepsilon$ turbulence model.	53

Fig. 4-23: Axial velocity contour plot along the central axis of the RHVT, for Mesh No.5 containing 1,522,948 nodes, $\mu_c=0.4$, $P_{in}=2\text{Bar}$ and $L/D=10$, using the $k - \varepsilon$ turbulence model.....	53
Fig. 4-24: Axial velocity contour plot along the central axis of the RHVT, for Mesh No.5 containing 1,522,948 nodes, $\mu_c=0.4$, $P_{in}=2\text{Bar}$ and $L/D=10$, using the SST turbulence model.....	53
Fig. 4-25: Tangential velocity contour plot along the central axis of the RHVT, for Mesh No.1 containing 1,705 nodes, $\mu_c=0.4$, $P_{in}=2\text{Bar}$ and $L/D=10$, using the $k - \varepsilon$ turbulence model.....	54
Fig. 4-26: Tangential velocity contour plot along the central axis of the RHVT, for Mesh No.5 containing 1,522,948 nodes, $\mu_c=0.4$, $P_{in}=2\text{Bar}$ and $L/D=10$, using the $k - \varepsilon$ turbulence model.....	54
Fig. 4-27: Tangential velocity contour plot along the central axis of the RHVT, for Mesh No.5 containing 1,522,948 nodes, $\mu_c=0.4$, $P_{in}=2\text{Bar}$ and $L/D=10$, using the SST turbulence model.....	54
Fig. 4-28: Radial velocity contour plot along the central axis of the RHVT, for Mesh No.1 containing 1,705 nodes, $\mu_c=0.4$, $P_{in}=2\text{Bar}$ and $L/D=10$, using the $k - \varepsilon$ turbulence model.....	55
Fig. 4-29: Radial velocity contour plot along the central axis of the RHVT, for Mesh No.5 containing 1,522,948 nodes, $\mu_c=0.4$, $P_{in}=2\text{Bar}$ and $L/D=10$, using the $k - \varepsilon$ turbulence model.....	55
Fig. 4-30: Radial velocity contour plot along the central axis of the RHVT, for Mesh No.5 containing 1,522,948 nodes, $\mu_c=0.4$, $P_{in}=2\text{Bar}$ and $L/D=10$, using the SST turbulence model.....	55
Fig. 4-31: Residual plot of mass and velocity components for the failed Reynolds Stress Model.....	56
Fig. 4-32: Comparison of the computed variation of internal normalised axial velocity at normalised radial locations with experimental results from [7] at the inlet region within the RHVT, using both the $k-\varepsilon$ and SST turbulence models respectively.....	57
Fig. 4-33: Comparison of the computed variation of internal normalised tangential velocity at normalised radial locations with experimental results from [7] at the inlet region within the RHVT, using both the $k-\varepsilon$ and SST turbulence models respectively.....	58

Fig. 5-1: Predicted streamline plot along the central axis show a successfully captured secondary flow within the RHVT, for $\mu_c=0.4$, $P_{in}=2\text{Bar}$ and $L/D=10$.	59
Fig. 5-2: Zoomed in view of the secondary flow within the RHVT, for $\mu_c=0.4$, $P_{in}=2\text{Bar}$ and $L/D=10$.	60
Fig. 5-3: Secondary flow captured at the entrance region of similar vortex tubes and the same original boundary conditions of Section 6.3 for (a) $d_c/D=0.4$, (b) $d_c/D=0.5$ and (c) $d_c/D=0.6$.	60
Fig. 5-4: Total temperature contour plot along the central axis of the RHVT, for $d_c/D=0.4$, $\mu_c=0.38$, $P_{in}=2\text{Bar}$ and $L/D=10$.	61
Fig. 5-5: Total temperature contour plot along the central axis of the RHVT, for $d_c/D=0.5$, $\mu_c=0.38$, $P_{in}=2\text{Bar}$ and $L/D=10$.	61
Fig. 5-6: Total temperature contour plot along the central axis of the RHVT, for $d_c/D=0.6$, $\mu_c=0.42$, $P_{in}=2\text{Bar}$ and $L/D=10$.	62
Fig. 5-7: Density contour plot along the central axis at the entrance region of the RHVT, for $\mu_c=0.4$, $P_{in}=2\text{Bar}$, $L/D=10$ and $d_c/D=0.5$, with streamlines of the secondary flow superimposed on the plot.	62
Fig. 5-8: Static temperature, total temperature, density and pressure contour plots along the central axis of the RHVT, for $\mu_c=0.4$, $P_{in}=2\text{Bar}$, $L/D=10$ and $d_c/D=0.5$.	63
Fig. 5-10: Rotational shear stress along the central axis of the RHVT for $\mu_c=0.4$, $P_{in}=2\text{Bar}$, $L/D=10$ and $d_c/D=0.5$.	65
Fig. 5-10: Rotational flow of work per unit area along the central axis of the RHVT for $\mu_c=0.4$, $P_{in}=2\text{Bar}$, $L/D=10$ and $d_c/D=0.5$.	65
Fig. A-1: Laminar and Turbulent Flows of Water from a tap.	71
Fig. A-2: Magnified view of a Turbulent Boundary Layer [32]	72
Fig. A-3: Mean velocity U and fluctuating velocity u' of the total velocity u .	73
Fig. A-4: Dye trace injected into a parallel mean flow. In the developing turbulent flow eddies of many sizes are superimposed onto the mean flow. An example of the turbulent length scale has been highlighted.	76
Fig. B-1: Boundary layer formation over a flat plate.	90
Fig. B-2: Axial and vertical velocity distributions versus Blasius similarity variable.	95
Fig. B-3: Spalding's law of the wall distribution.	98
Fig. B-4: The flow domain.	99

Fig. B-5: Close up of the final mesh for the laminar solution showing the inflationary layer and course inviscid region cells.....	100
Fig. B-6: Inflation layer of the initial mesh used for the laminar solution. Total number of elements = 161560.....	101
Fig. B-7: Inflation layer of an intermediate mesh used for the laminar solution. Total number of elements = 390076.....	101
Fig. B-8: Inflation layer of the final mesh used for the laminar solution. Total number of elements = 882324.....	101
Fig. B-9: Panned out view of the final mesh, as an illustration of the density of elements required for a very accurate solution.....	102
Fig. B-10: Inflation layer of the final mesh used for the turbulent solution. Total number of elements = 330538.....	102
Fig. B-11: Panned out view of the final mesh used for the turbulent solution.....	102
Fig. B-12: Axial velocity contours for a very narrow bandwidth of 1.98 to 2.031m/s for (a) free slip and (b) outlet, inviscid region boundary conditions.....	104
Fig. B-13: Residual plot of mass and velocity components for the final laminar solution.....	106
Fig. B-14: Residual plot of mass and velocity components for the final turbulent solution.....	106
Fig. B-15: Comparison of computed axial velocity profiles with Blasius theoretical profile for laminar flow over a flat plate.....	107
Fig. B-16: Comparison of computed vertical velocity profiles with Blasius theoretical profile for laminar flow over a flat plate.....	107
Fig. B-17: Comparison of the computed skin friction coefficient with the theoretical solution for laminar flow over a flat plate.....	108
Fig. B-18: Comparison of computed axial velocity profiles with Spalding's law of the wall solution for turbulent flow over a flat plate.....	108
Fig. B-19: Comparison of the computed skin friction coefficient with the theoretical solution for turbulent flow over a flat plate.....	109

List of Tables

Table 4-1: Previous publishers of the variation of ΔT_c with μ_c in a RHVT and their respective configurations.....	38
Table 4-2: Mesh convergence study for a RHVT subject to values of $\mu_c=0.4$, $P_{in}=2\text{Bar}$ and $L/D=10$, using the $k-\varepsilon$ turbulence model.....	45
Table 4-3: Thermal output of a RHVT subject to values of $\mu_c=0.4$, $P_{in}=2\text{Bar}$ and $L/D=10$, using the $k-\varepsilon$ and SST turbulence models respectively.....	49
Table 5-1: Thermal output of a RHVT subject to values of $P_{in}=2\text{Bar}$, $L/D=10$, using (a) $d_c/D=0.4$, (b) $d_c/D=0.5$ and (c) $d_c/D=0.6$ respectively.....	61
Table A-1: Advantages and disadvantages of Prandtl's Mixing Length Model [32].....	77
Table A-2: Advantages and disadvantages of the $k - \varepsilon$ model [32].....	83
Table A-3: Advantages and disadvantages of the $k - \omega$ model [32].....	84
Table A-4: Advantages and disadvantages of the Reynolds Stress Equation Model [32].....	88
Table B-1: Solution of the Blasius laminar flat plate boundary layer in similarity variables.....	94

1 The Ranque – Hilsch Vortex Tube

1.1 Introduction

The RHVT is an ingenious invention credited to both Georges Joseph Ranque and Rudolf Hilsch, who contrived the device independently during war torn Europe in the 1940's [1].

A RHVT separates an injected stream of gas into two streams, one significantly hotter along with another substantially colder than the injected stream. This is remarkable considering the absence of any moving parts or work input. While geometrically simple, the fluid dynamic and thermodynamic processes in a RHVT are extremely complex. To experimentally measure and plot velocity, pressure and temperature contours accurately within the tube in order to gain a better insight into the mode of heat migration is very difficult. A simpler alternative is to employ CFD. Currently there is no conclusive evidence as to the mode of energy migration within the RHVT.

1.2 The Ranque - Hilsch Vortex Tube

In the 19th century British physicist James Maxwell suggested that a system of drawing both hot and cold water out of a single pipe might be devised if we could capture a small demon and train him to open and close a tiny valve. The demon would open the valve only when a fast (hot) molecule approached it, and close the valve against slow (cold) molecules [2]. This imaginary device, and with the help of Maxwell's demon, could be a source of hot and cold fluids on demand from ambient temperatures. Although hypothesising, Maxwell may have been startled to know that within the next century such a device would become a reality. This device which initially bared the nickname Maxwell's Demon Tube, was soon to be known as its name today, the RHVT. The cross sectional schematic shown overleaf in Fig. 1-1 illustrates quite clearly that the RHVT is a device that does indeed separate simultaneously a flow of gas into two streams, significantly hotter and cooler than the inlet temperature, despite the absence of any moving parts or work input, electrically or chemically. This lack of a conventional energy source is in principle the core

reason as to why there is so much interest in the device through academics and enthusiasts alike.

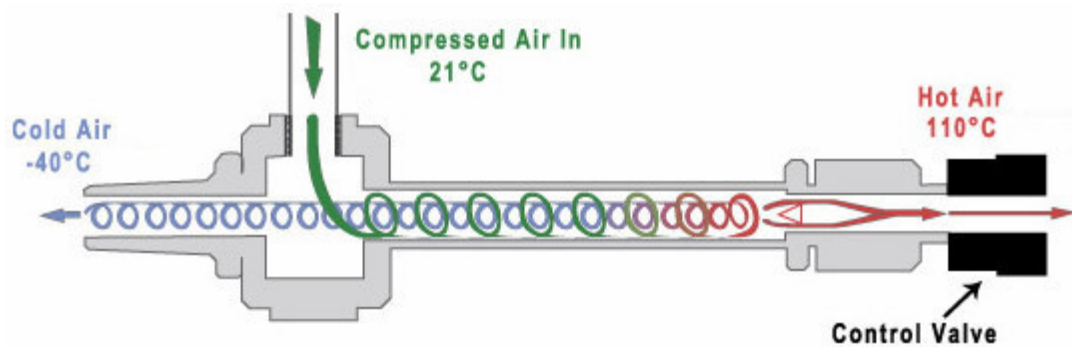


Fig. 1-1: Typical Operation of a Modern Counter-Flow RHVT [3].

As stated previously the origin of the RHVT is accredited to two men during and after war-time Europe circa 1933-1946, namely French man Georges Joseph Ranque and a German called Rudolf Hilsch. Their contributions will now be discussed.

1.3 Ranque's Contribution

One of the most comprehensive historical documents detailing the chain of events leading to and analysing the discovery of the RHVT was documented by C.D. Fulton [1] shortly after Ranque and Hilsch's findings. Fulton ascertained that when "Ranque, the discoverer of this technology, presented himself before the Société Française de Physique in June 1933 and told his audience that hot and cold air came out of opposite ends of a simple piece of pipe, (he) was received with scepticism..... Aerodynamicists at the time simply came to the conclusion that stagnation temperature had been confused with static temperature; the two streams weren't really cold and hot" [1].

The illustration below, along with others in this passage, have been obtained directly from Ranque's patent [4].

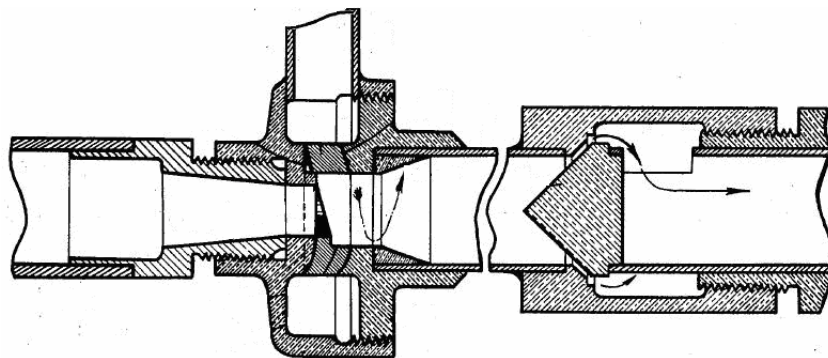


Fig. 1-2: Cross-Section of Ranque's Vortex Tube Design [4].

Notably modern day commercial vortex tubes are fundamentally very similar to the design given in Fig. 1-2 as shown by the exploded parts view of a modern RHVT below in Fig. 1-3.

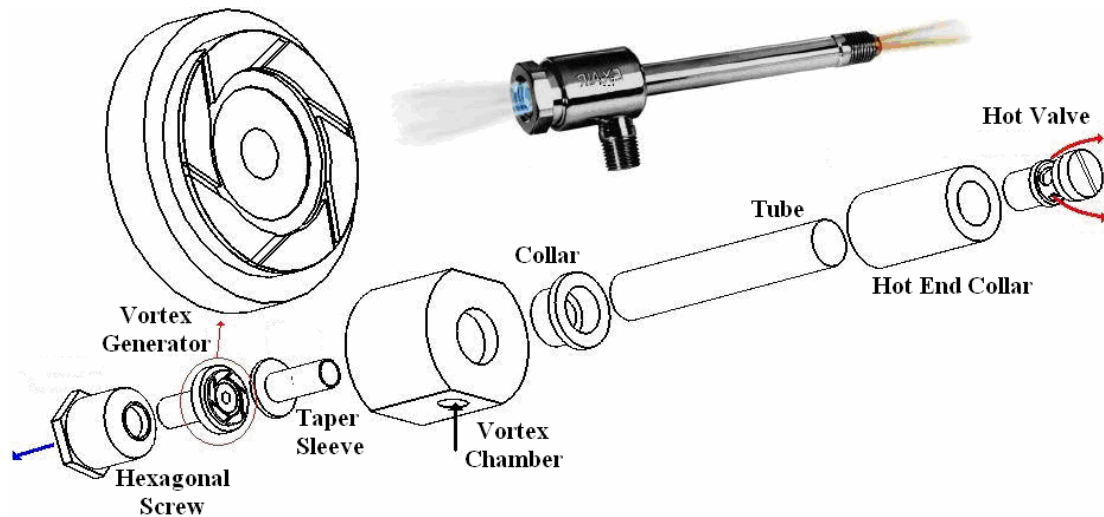


Fig. 1-3: Commercial RHVT by Exair [5].

The first published record of the principle of the RHVT phenomenon occurred on 12th December 1931, when Ranque filed a French patent docket. After the French patent issued in 1931, he filed the same docket in the United States as previously mentioned. In this patent Ranque showed that the tangential entrance may consist of a single nozzle, a plurality of nozzles, or a set of blades. He also described how, by adjusting the size of the cold-air orifice or the restriction at the end of the hot tube, one may obtain a small quantity of moderately cold air, and mentioned that the temperature of the hot tube reaches its maximum when the end of the hot tube is entirely closed, and that the higher the pressure of the air supplied, the colder the cold air will be. Furthermore Ranque spoke of having measured the pressure distribution inside the tube, a task which is very much easier said than done, as illustrated in Fig. 2-1 later in this work.

The theory Ranque gives in the United States patent, was stated as follows, “The rotating gas spreads out in a thick sheet on the wall of the tube and the inner layers of this sheet press upon the outer layers by centrifugal force and compress them, thus heating them. At the same time the inner layers expand and grow cold. Friction between the layers is to be minimised” [4].

1.4 Hilsch's Contribution

It is thought that Hilsch, physicist of the University of Erlangen, got to know of this device due to information supplied to him from occupied France [1]. Hilsch published an article in 1946 [6] and in it he refers briefly to Ranque's paper of 1933 as the source of the idea, but it seems that he had not learned of the patent. He had arrived nevertheless at exactly the same design shown in certain of Ranque's drawings [1].

In this article Hilsch wrote: "The air passing through the orifice has been expanded in the centrifugal field from the region of high pressure at the wall of the tube to a low pressure near the axis. During this expansion it gives considerable part of its kinetic energy to the peripheral layers through increased friction. The peripheral layers then flow away with increased temperature....The internal friction....causes a flow of energy from the axis to the circumference by trying to establish a uniform angular velocity across the entire cross section of the tube" [6].

Following Hilsch, nearly everyone has used similar counter-flow designs to the complete neglect of the uniflow type, as shown for example in Fig. 1-4 below. This is in part to the fact that a counter-flow type is easier to manufacture and offers two distinct hot and cold outlets at opposite ends of the tube where the thermal output of each cannot interfere with each other. As a consequence of this, the counter – flow design is the primary focus of this project.

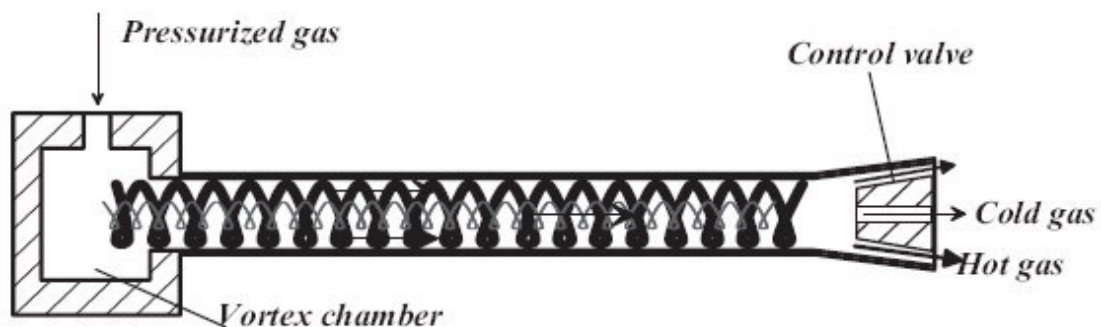


Fig. 1-4: Cross Section of a Uniflow RHVT [7].

1.5 Fundamentals of the Ranque-Hilsch Vortex Tube

Before exploring current published research papers, theses, articles etc. on the RHVT it is important to have the fundamental aspects of the device understood and in place. These basic understandings of the RHVT draw from the well established principles of Thermodynamics and Fluid Dynamics, and it will be shown that the heat migration within the RHVT is not in conflict with long accepted aspects of both these engineering disciplines.

1.5.1 Thermodynamics of the Ranque – Hilsch Vortex Tube

When first introduced to vortex tube technology, it would appear that there has been a violation of the laws of thermodynamics. It would seem that there is an internal heat flux without any work input. As in any refrigeration process, work input is paramount to its operation. Herein lies the crux of the problem, and the almost century long quest to fully understand the operation of the tube.

The First Law of Thermodynamics can be written as follows, “When a system undergoes a thermodynamic cycle then the net heat supplied to the surroundings plus the net work input to the system from its surroundings is equal to zero” [8].

Mathematically this statement is written as:

$$\sum Q + \sum W = 0 \quad (1.1)$$

where Q and W denote the heat supplied and work input to the system respectively. From this First Law the steady flow energy equation can be applied to the RHVT’s boundary as shown in Fig. 1-5.

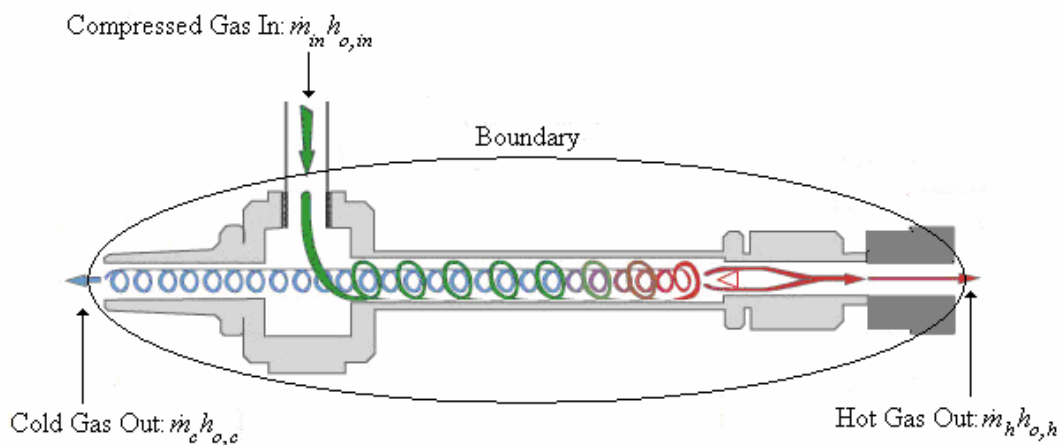


Fig. 1-5: System Boundary applied to RHVT.

Resulting in an equation of the following form:

$$\dot{m}_{in} \left(h_{s,in} + \frac{\mathbf{U}_{in}^2}{2} + Z_{in} \right) + \dot{Q} + \dot{W} = \dot{m}_c \left(h_{s,c} + \frac{\mathbf{U}_c^2}{2} + Z_c \right) + \dot{m}_h \left(h_{s,h} + \frac{\mathbf{U}_h^2}{2} + Z_h \right) \quad (1.2)$$

where \dot{m} , h_o , h_s , \mathbf{U} , Z , \dot{Q} and \dot{W} denote the mass flow rate, the total enthalpy, the static enthalpy, the velocity vector, the height above the datum, the rate of heat and work inputs supplied respectively, and the subscripts in , c and h denote the inlet, cold and hot outlets respectively.

By using some simple elimination of a few equal and negligible terms, the steady – flow energy equation reduces to a reversed adiabatic mixing equation with use of the following steps:

1. Combining static enthalpies and kinetic energies into total enthalpy.
2. Acknowledging that the potential energies at each point are approximately the same.
3. There is no heat or work input.

The reversed adiabatic mixing equation is as follows, and it shows that the RHVT does indeed satisfy the first law, as energy is conserved:

$$\dot{m}_{in} h_{o,in} = \dot{m}_c h_{o,c} + \dot{m}_h h_{o,h} \quad (1.3)$$

This can be reduced further by introducing the ratio used to describe the ratios of cold and hot gas flows as compared to the supplied gas flow; this ratio is called the cold gas fraction:

$$\mu_c = \frac{\dot{m}_c}{\dot{m}_{in}} \quad (1.4)$$

which is easily recognised by dividing Equation (1.3) by the inlet mass flux, \dot{m}_{in} :

$$h_{o,in} = \mu_c h_{o,c} + (1 - \mu_c) h_{o,h} \quad (1.5)$$

If the gas flowing through the RHVT is treated approximately as an ideal gas and changes in kinetic energy are neglected we can write the above conservation equation as follows:

$$c_p T_{o,in} = \mu_c c_p T_{o,c} + (1 - \mu_c) c_p T_{o,h} \quad (1.6)$$

where c_p and T_o are the specific heat capacity at constant pressure and the total temperature respectively. Dividing across by c_p , we get:

$$T_{o,in} = \mu_c T_{o,c} + (1 - \mu_c) T_{o,h} \quad (1.7)$$

results in a rather simplistic energy balance equation, but it does illustrate quite clearly that when considered as a system with boundaries the RHVT does indeed satisfy basic thermodynamic rules.

A much broader perspective of the system needs to be conducted to show that the Second Law of Thermodynamics is satisfied, i.e. that “it is impossible to construct a device that operating in a cycle will produce no effect other than the transfer of heat from a cooler to a hotter body” [8].

As there is no mechanical work input to a RHVT, and yet there is a heat flux, to obey the above two classic laws of thermodynamics; there must be a supply of work of some other form. The source of this work has been the main argument since the establishment of this technology.

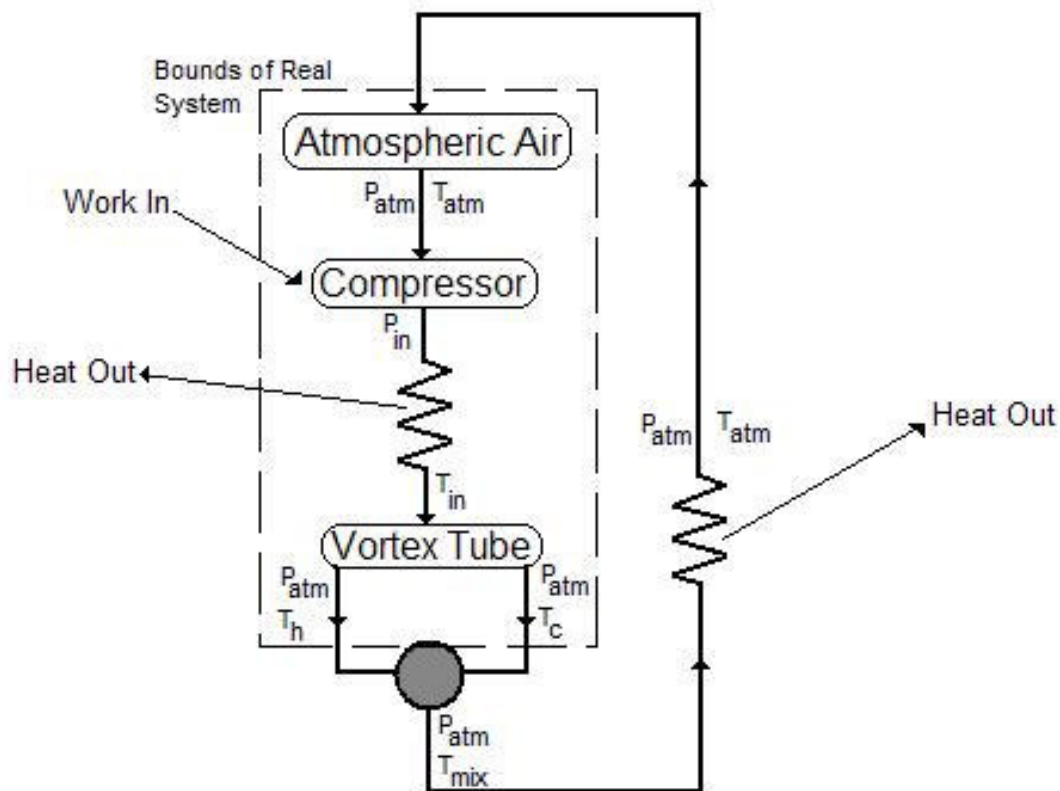


Fig. 1-6: Complete Ranque-Hilsch Vortex Tube System Including Compressed Air Supply [9].

Analysis of the complete RHVT system from the source of the flow potential, as in the compressor supply, to the exit of the two streams of hot and cold air, gains a different perspective. The system is now viewed from the suction of atmospheric air through the compressor, channelled through the supply piping and back to the atmosphere, through both exits of the RHVT. It is now easier to see that the RHVT does indeed satisfy the second law above, and that equilibrium is indeed maintained, in that the compressed air does indeed return to atmospheric conditions, once it has completed its cycle. Fig. 1-6 shows the RHVT as a complete system does indeed satisfy the second law of thermodynamics.

1.5.2 Fluid Dynamics of the Ranque – Hilsch Vortex Tube

In a RHVT a high pressure fluid, mainly compressed air, enters the tube and passes through nozzles achieving a high angular velocity and hence causing a vortex-type flow, as can be seen in Fig. 1-1. There are two outlets to the tube: the hot outlet is placed near the outer radius of the tube at the end away from the inlet nozzles and the cold outlet is placed at the centre of the tube at the same end as the air inlet.

By adjusting a control valve downstream of the hot outlet it is possible to vary the fraction of the incoming flow that leaves through the hot outlet on the periphery of the tube. The proportion of cold gas deflected back through the cold outlet is referred to as the cold fraction, μ_c , previously defined in Equation (1.4). By varying the cold fraction the cold outlet total temperature drop ($\Delta T_{o,c} = T_{o,in} - T_{o,c}$) can be adjusted accordingly, as can be seen for example in the experimental results in Fig. 1-7

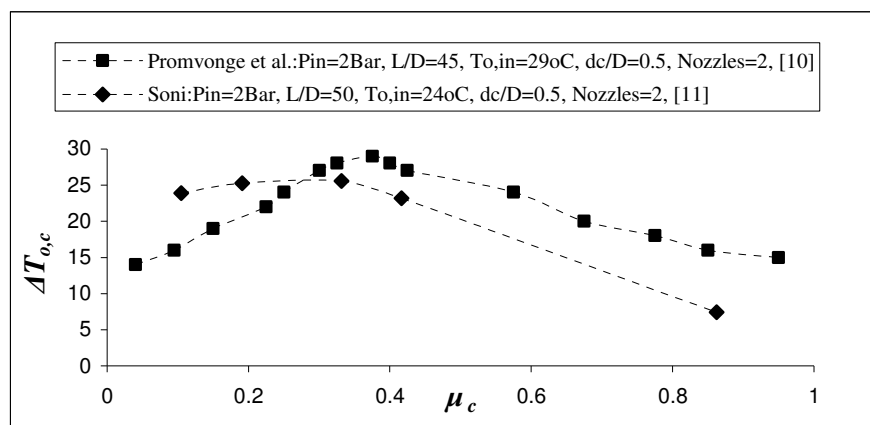


Fig. 1-7: Variation of $\Delta T_{o,c}$ with μ_c for typical RHVT [10,11].

where the terms P_{in} , $T_{o,in}$, L , d_c , and D , denote static gauge pressure and total temperature at the inlet, the length of the RHVT, diameter of the cold outlet and diameter of the RHVT respectively.

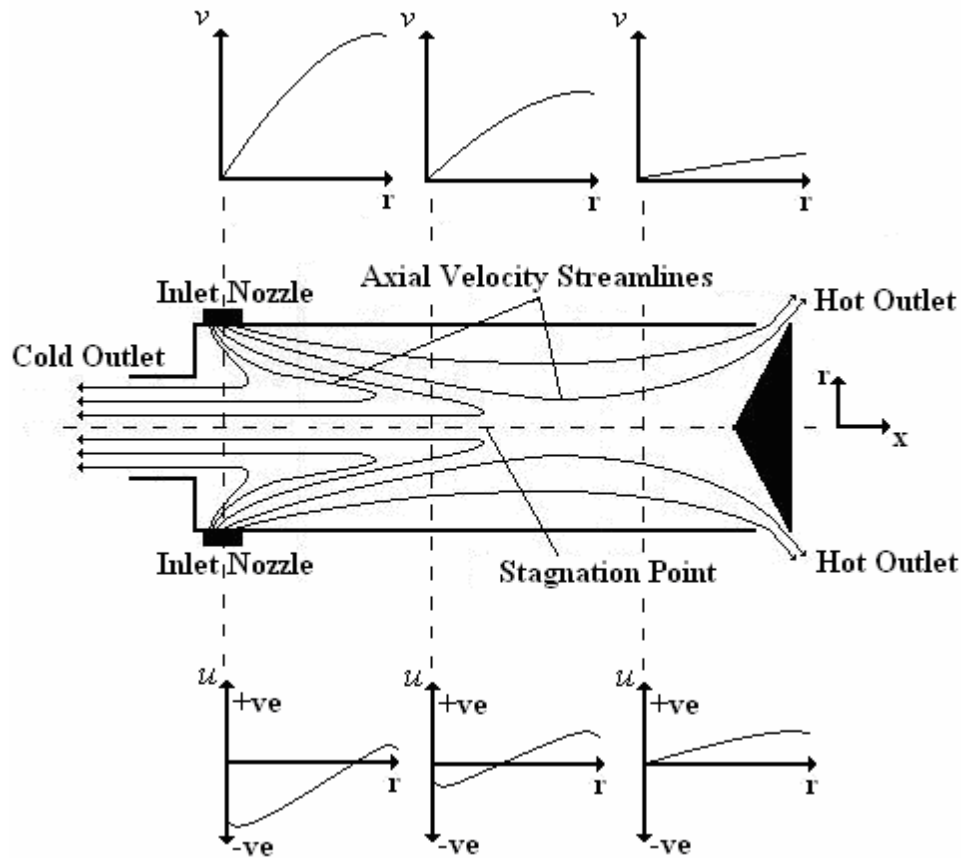


Fig. 1-8: Axial velocity streamline plot and graphs of tangential and axial velocity and their distribution along the central axis of the RHVT.

An analysis of a basic axial velocity streamline plot gives a clearer understanding of the variance of both the axial and indeed the tangential velocities throughout the RHVT. Where, the graphs of the axial and tangential velocities in Fig. 1-8 denote the axial direction and rotational strength of the vortex, at various axial and radial locations along the RHVT. As can be seen Fig. 1-8 in the streamline plot the compressed air enters through the inlet nozzles and a proportion of this flow leaves through the hot and cold outlets respectively. In addition to the streamline plot, graphs of the tangential and axial velocities (denoted by v and u respectively) and their variance along the axial, x – direction, of the RHVT has been shown. These graphs are visual representations of more comprehensive experimental results shown later in Fig. 4–32 and Fig. 4-33.

It can be easily observed from the graphs in Fig. 1-8 the RHVT that the tangential velocity i.e. the swirling/rotating component of the vortex flow is strongest

at the entrance region (i.e. near the inlet nozzles) of the RHVT and decays significantly in magnitude towards the hot outlet. In the lower graphs it can be seen that in the entrance region the axial velocity of the vortex flow is positive (i.e. in a direction towards the hot outlet) at outer radial locations in the RHVT, and moves in a negative direction at inner radial locations of the vortex flow. What this means is that there are two vortices moving in opposite axial directions within this region. This reversal in flow towards the cold exit occurs in the positive x – direction from the inlet nozzles up to a point defined as the stagnation point, as highlighted in Fig. 1-8.

The stagnation point also marks the limiting point where further increases of the vortex tube length beyond this point does not improve the energy separation, as observed by Aljuwayhel et al. [12]. This important aspect has been utilised later on in reducing the length of the computational domain of the vortex tube to that used by researchers in their experiments. Towards the hot outlet the motion is no longer purely rotational due to friction from walls, slowing the tangential components of the flow substantially.

1.6 Commercial Vortex Tubes

Currently there is no conclusive evidence as to the mode of energy migration within the RHVT. However, recently, it has been developed commercially for small-scale spot-cooling applications despite an incomplete understanding of vortex tube physics. There are a range of RHVT manufacturers who have developed and applied RHVT theory into practical and effective cooling solutions for industrial use. Such companies include Exair and ITW Vortec, both in the United States. Locally for the Irish market, Flowtech, UK, supplies Exair RHVTs. They market their product for a range of different applications, based on the following qualities of RHVT technology:

- Clean form of cooling
- Maintenance free – no moving parts
- Stable temperature output
- Cools without electricity or refrigerants
- Exceptionally reliable, compact and lightweight
- Low cost

There is a wide variety of applications for vortex tubes including previously mentioned spot cooling, but also some not so obvious innovative ideas are marketed.

1.6.1 Spot Cooling Applications

RHVTs have a very wide range of application for industrial spot cooling on machines, assembly lines and processes.



Fig. 1-9: Cold Air Gun by ITW Vortec [13].

One such example is the Cold Air Gun with magnet base, shown in Fig. 1-9 above used as a substitute for coolant in machining processes.

Other spot cooling applications include:

- Cool plastic injection moulds
- Dehumidify gas operations
- Cool heat seal operations
- Cooling of control cabinet electrical enclosures, as illustrated below in Fig. 1-10 and overleaf in Fig. 1-11



Fig. 1-10: Control Cabinet RHVT by Exair [5].

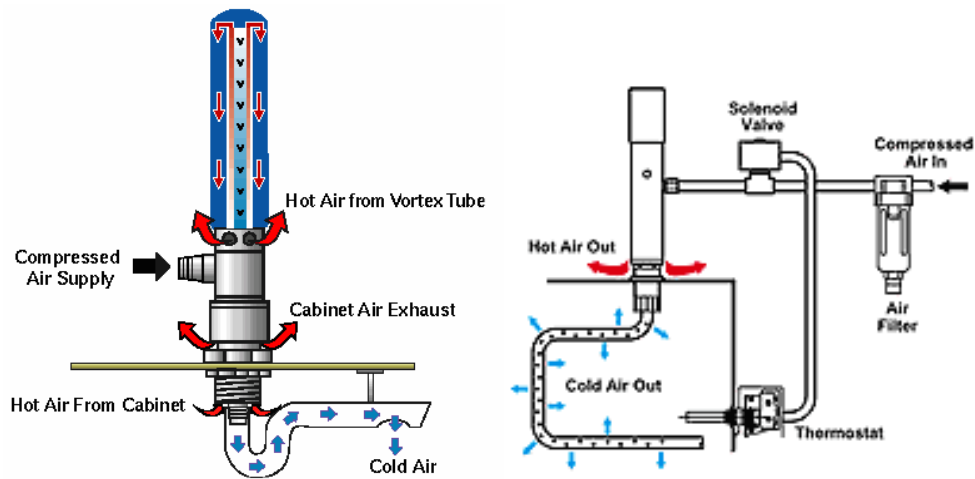


Fig. 1-11: Explanation of Control Cabinet Cooling RHVT by Exair [5].

1.6.2 Spot Heating Applications

Not neglecting the hot air output, spot heating applications include:

- Setting solders and adhesives
- Dry ink on labels and bottles

1.6.3 Experimental Ranque-Hilsch Vortex Tube Equipment

Experimental equipment for use in thermodynamic and fluid dynamic laboratories is available commercially from P.A. Hilton Ltd. in the U.K. A picture of this apparatus is shown in Fig. 1-12 below.



Fig. 1-12: Experimental RHVT Equipment, by P.A. Hilton Ltd [14].

1.6.4 Personal Air Conditioners

RHVTs can be used in an Air Vest, as marketed by ITW Vortec to distribute cooled or heated air over the upper body, as illustrated in Fig. 1-13 below.



Fig. 1-13: Personal Air Conditioner by ITW Vortec [13].

1.7 Current Energy Separation Theory

The longest serving and most established theory was first proposed by Hilsch [6]. He suggested that angular velocity gradients in the radial direction give rise to frictional coupling between different layers of the rotating flow resulting in a migration of energy via shear work from the inner layers to the outer layers. However this theory may not altogether explain the mode of heat transfer within the tube.

To supplement this theory a hypothesis has been forwarded by Ahlborn et al. [15 – 17], that the presence of a secondary flow field contributes to the energy migration within the RHVT. The hypothesis states that a primary fluid flow consisting of outer and inner vortices exists that spans the length of the tube, and that an embedded secondary flow loop exists that convects heat between the two vortex flows, acting as the refrigerant of an open thermodynamic cycle. This theory has since been supported by Gao et al. [18] and it is based on experimental evidence. Capturing this secondary flow and quantifying its influence in relation to the proposed heat pump theory using CFD is just one of the main objectives of this study.

1.8 Summary

In this section the fundamental operation of the RHVT has been introduced along with some examples of applications of the tube within various industries. The next section of this work will develop the current energy separation theory into the mode of heat transfer within the tube.

2 Literature Review

2.1 Introduction

It has already been shown that an external analysis of the RHVT proves that the RHVT obeys both the First and Second Laws of Thermodynamics. However this external perspective does not offer any insight into the internal mechanisms in the RHVT which force the temperature separations to both the hot and cold outlets. Despite the simplicity of the vortex tube's geometry, the energy separation phenomenon within the RHVT is quite complex. The RHVT requires no work or heat interaction with the environment. Consequently, the separation effect must be attributable to an energy interaction that occurs internally between the hot and cold vortices. At present several conflicting theories have been advanced to explain the vortex tube's behaviour since its initial observation by Ranque. Despite the various experimental and analytical investigations that have been carried out on the vortex tube, the mechanism of the temperature separation effect is still in question due in part to a lack of reliable measurements of the internal temperature and velocity distributions.

Unfortunately internal experimental analysis has been shown by Cockerill [9] to distort the flow field through the use of pressure and temperature probes, which can only offer up limited accuracy. Pitot tubes by their very design can only disrupt the flow so as to alter the dynamics of what is happening. Despite these restrictions researchers have not been hindered in discovering important characteristics of the internal flow field of which will provide a basis of comparison to the results found in this CFD study.

2.2 Velocity Profiles in the Ranque – Hilsch Vortex Tube

Useful comparative velocity profiles within the RHVT are available from only a very limited amount of authors including Gao et al. [7], Ahlborn et al. [15] and Bruun [19]. At present Gao et al. [7] results are to the best of the authors knowledge, the most recent and comprehensive results published for both tangential and axial velocities. In order to obtain their data Gao et al. developed the experimental apparatus shown overleaf in Fig. 2-1.

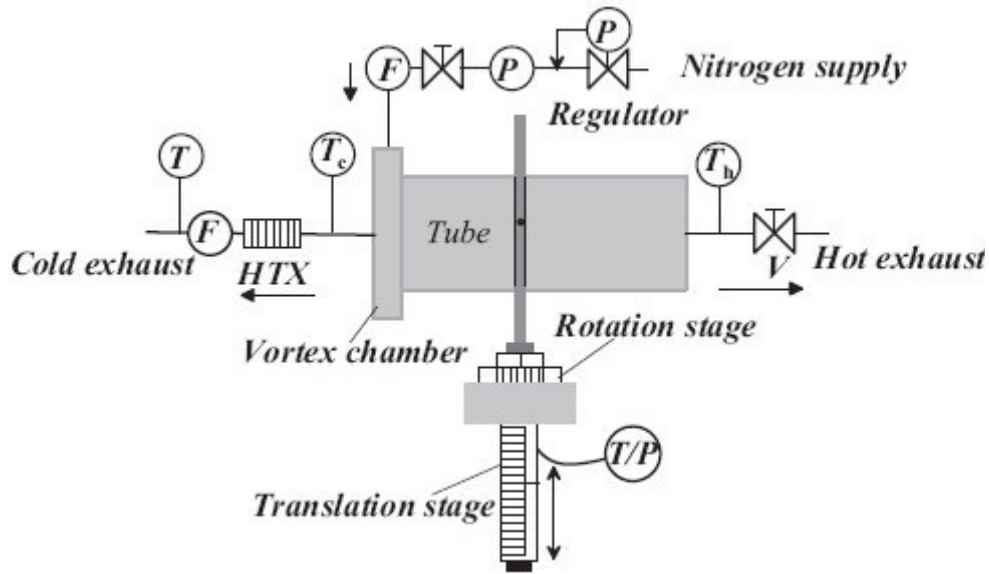


Fig. 2-1: Experimental Set-Up to measure flows internal to the RHVT [7].

The cylindrical pitot device highlighted above can be rotated and translated through radial planes at different axial locations within the RHVT and was used successfully to give the velocity profiles shown in Fig. 2-2 below and Fig. 2-3 overleaf.

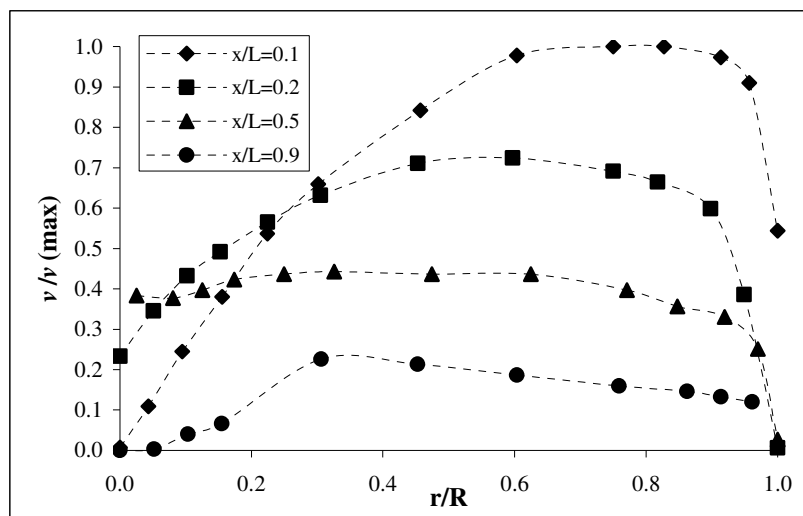


Fig. 2-2: Experimental results of internal normalised tangential velocities at normalised radial and axial locations within a RHVT for $P_{in}=6\text{bar}$, $L/D=65$, and $\mu_c=0.4$ [7].

It should be noted that these experimental results are normalised across radial locations for different axial distances (x/L) from the inlet nozzles and this means that they can be compared to results from similar RHVT with different geometries to that used by Gao et al [7].

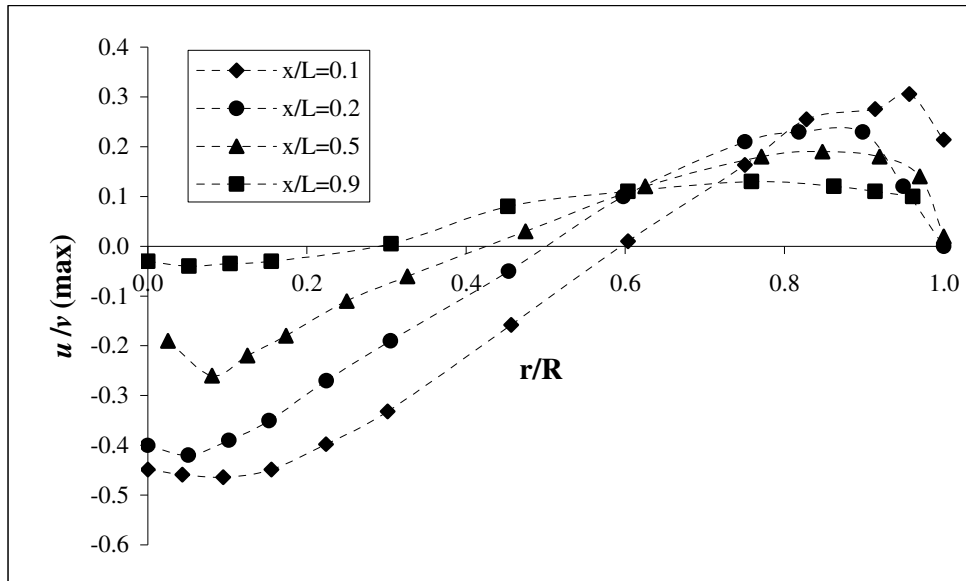


Fig. 2-3: Experimental results of internal normalised axial velocities at normalised radial and axial locations within a RHVT for $P_{in}=6\text{bar}$, $L/D=65$ and $\mu_c=0.4$ [7].

2.3 Experimental Proof of Secondary Flow

Experimental proof of a secondary circulation within the RHVT was first published by Ahlborn et al. [15] and subsequently by Gao et al. [18]. These authors ascertained the presence of this secondary flow by using apparatus such as that shown in Fig. 2-1 and by measuring the axial and tangential velocities in the RHVT. The recirculating region of flow was discovered when it was established that the mass flow returning towards the cold outlet is much larger than the cold mass flow emerging out the cold end. An illustration of both primary and secondary flow is given below in Fig. 2-4.

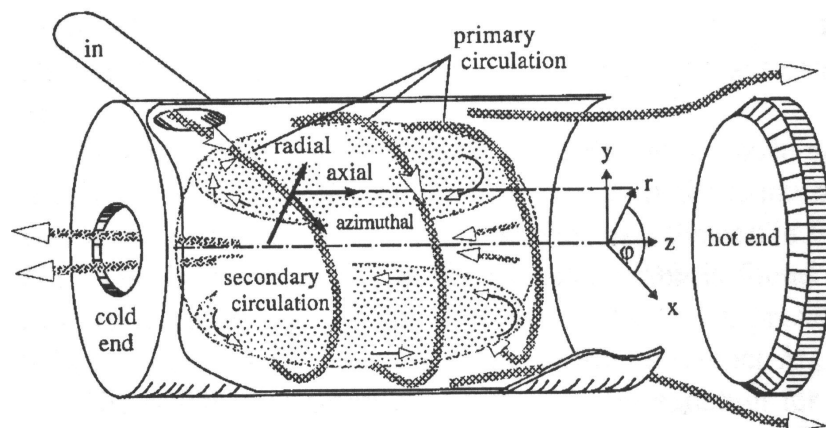


Fig. 2-4: Primary and Secondary circulation within the RHVT [15].

2.3.1 Secondary Flow working as a Refrigeration Cycle

In subsequent publications Ahlborn et al. [16,17] went on to explain the function of secondary flow within the RHVT is to provide a method of temperature separation based on the analogy of conventional heat pump mechanisms, as illustrated in Fig. 2-5 below.

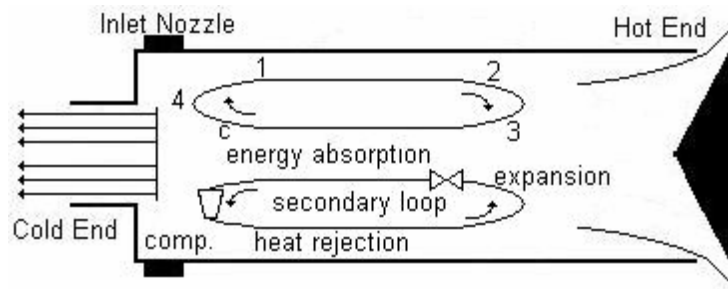


Fig. 2-5: Heat pump cycle within a RHVT [16].

With reference to the diagram above heat pump cycle within the RHVT can be explained as follows:

- From points 4→1 heat is rejected in the vicinity of the entrance nozzle, relatively warm gas in the secondary loop rejects heat to the cooler gas in the primary circulation.
- From points 1 →2 →3 the working fluid adiabatically expands from the high pressure heat exchange region and travels towards the tube's hot end. There it turns inwards at point 2 to join the backflow core at point 3. As there is a sizeable angular velocity remaining, the pressure at point 2 must be higher at point 3, therefore the gas in the secondary loop expands adiabatically.
- From points 3→c energy absorption occurs between these points and as such this is the refrigeration branch in which the gas in the primary loop cools by transferring energy to the secondary circulation. The fluid resistance experienced by the axial flow is not like wall friction in an ordinary pipe, but rather an effect of momentum transfer to the adjacent fluid in the secondary flow, so as energy is pumped from the primary to the secondary loop.
- From points c → 4 adiabatic compression occurs in this region where the secondary circulation is pushed outwards, where it is recompressed as it moves towards point 4.

Although there is experimental evidence of a secondary flow within the RHVT, the analogy of its operation being similar to that of a heat pump contributing to the heat migration is still open to question. In these experimental investigations of secondary flow its presence was numerically deduced from careful analysis of the axial and tangential velocities. These researchers had, and continue to have, no means of visualising this secondary flow. By capturing this secondary flow through the use of CFD, a clearer insight can be gained. A greater foundation for this theory can be quantified if evidence of the heat pump cycle of expansion, heat rejection, compression and energy absorption can be detected.

Comprehensive analysis of evidence of this hypothesis will be conducted, as a core aspect of this project as outlined previously. As this is a new conceptual theory, at present there are few supporting papers on this hypothesis. However a much older theory of frictional heat transfer has numerous supporters and is described below.

2.4 Frictional Heat Transfer

When Hilsch [6] rejected Ranque's hypothesis on the source of the energy migration within the RHVT, he proposed theory that angular velocity gradients in the radial direction give rise to frictional coupling between different layers of the rotating flow resulting in a migration of energy via shear work from the inner layers to the outer layers. This working principle has since been utilised by numerous contributors including Lewins et al. [20], Frohlingsdorf et al. [21], Deissler and Perlmutter [22], and Young and Cutcheon [23].

Comprehensive theory on the frictional heat transfer has been published by Fulton [1] where he describes the main shear stress $\tau_{r\theta}$ as being caused by the turning of one cylinder inside another. This stress according to frictional heat transfer theory given by Fulton is by far the largest shear stress and it is the primary cause of the energy migration within the RHVT. This rotational shear stress is expressed as follows from [1]:

$$\tau_{r\theta} = \mu \left(\frac{\partial v}{\partial r} - \frac{v}{r} \right) \quad (2.1)$$

This shear stress is constantly at work to convert the free vortex into a forced vortex resulting in a free vortex as a peripheral warm stream and a forced vortex as a inner cold stream, as can be seen overleaf in Fig. 2-6.

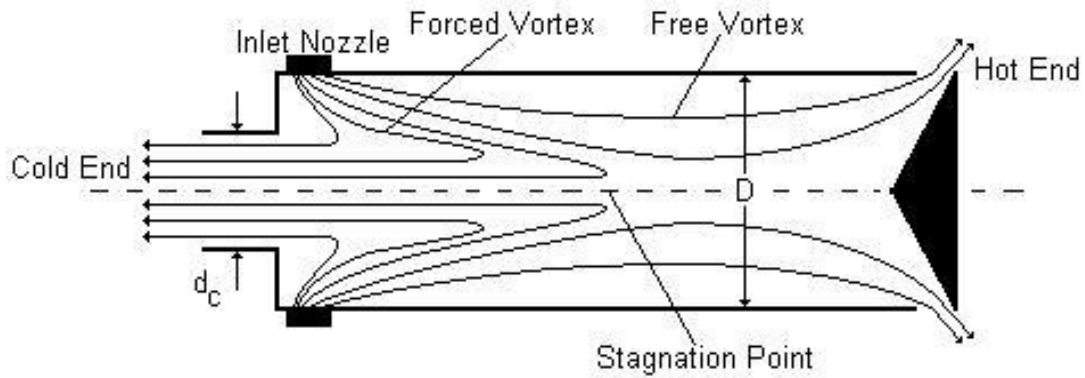


Fig. 2-6: Schematic Flow Pattern of a RHVT.

These vortices are described quite simply below where it can be seen that within a forced vortex the tangential velocity, v , is directly proportional to the radial location r , and the free vortex the tangential velocity is inversely proportional to the radial location r squared.

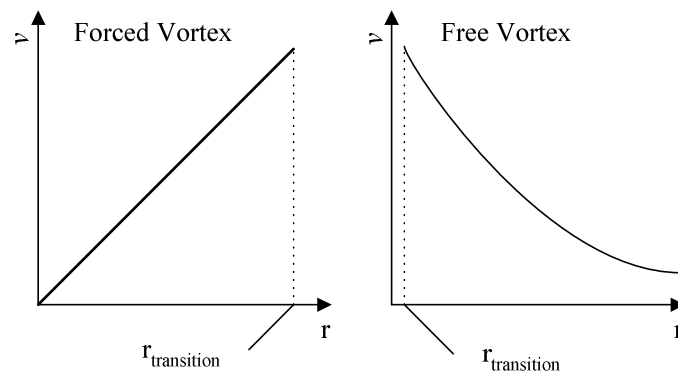


Fig. 2-7: Forced Vortex and Free Vortex.

In frictional heat transfer theory it is this interaction of free and forced vortices that results in a flow of work and hence heat migration in a RHVT.

2.4.1 Flow of Work in the Ranque – Hilsch Vortex Tube

As work is simply force times the distance travelled it can be implied that in a fluid where the shear stress at the surface is τ_{ij} and the velocity of the fluid is \mathbf{U} , the rate of flow of work per unit area of the surface is:

$$\dot{W}_{ij} = \tau_{ij} \mathbf{U} \quad (2.2)$$

This work flows perpendicularly across the surface from the more rapidly moving fluid to the less rapidly moving fluid. Therefore the rotational work per unit area $\dot{W}_{r\theta}$, produced by the main shear stress $\tau_{r\theta}$ is as follows:

$$\dot{W}_{r\theta} = \mu \left(\frac{\partial v}{\partial r} - \frac{v}{r} \right) \mathbf{U} \quad (2.3)$$

This rotational work per unit area is the main source of frictional energy transfer from the cold inner region to the hot peripheral vortex flow.

2.5 Acoustic Streaming in Vortex Tubes

Another explanation worthy of mention as to how the energy separation occurs in a RHVT, is the work of Kurosaka [24] who attributes the energy separation in the RHVT to acoustic streaming (sound waves) caused by the vortex whistle. As the RHVT operating theory mentioned here has little association with theories of CFD, it is presented here in its most basic form, as a means to show that there may be further considerations to take into account when explaining RHVT operation. This published work shows there is evidence of acoustic streaming having a tangible effect on the operation of the RHVT. It does not however conclusively explain the mode of operation of the RHVT in any way.

In his work Kurosaka [24] derived a relationship between the swirl velocity and the expected angular frequencies of disturbances generated by the vortex whistle, and indirectly a means of measuring the performance of the RHVT with a sound spectrum. To investigate his theory, Kurosaka measured the acoustic output of a RHVT. He obtained a series of spectra similar to that shown in Fig. 2-8 overleaf, with peaks at discrete frequencies, clearly showing harmonics.

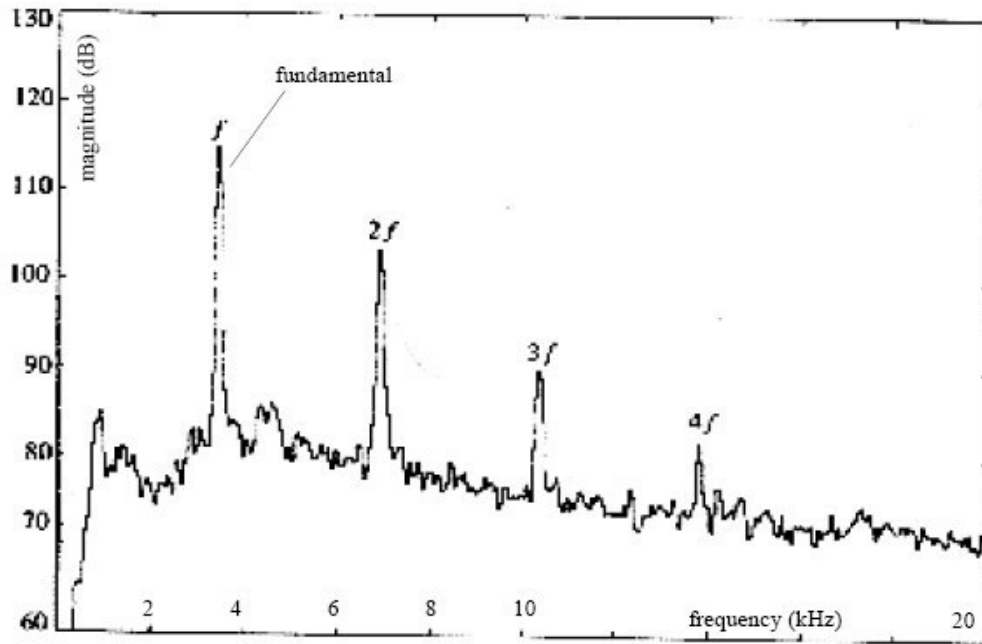


Fig. 2-8: The spectral density of the acoustic signal obtained by Kurosaka [24].

By drilling out the sides of the tube, and installing tuned acoustic suppressors, Kurosaka attempted to attenuate the disturbances at a particular inlet pressure and by gradually increasing this pressure, he observed the energy separation of his tube developed in the normal way, until the pressure was such that acoustic disturbances are attenuated, yielding spectra such as that in Fig. 2-8. At this point there was a fairly substantial drop in the separation performance, as can be seen in Fig. 2-9 overleaf.

The graph overleaf shows that any suppression in the vortex whistle will lead to degradation in the energy separation effect of the RHVT. Cockerill [9] suggests that the general validity of the acoustic streaming explanation has to be questioned as other researchers such as McDuffie [25] also measure the sound output from a vortex tube similar to Kurosaka and find no evidence of the frequencies detected by Kurosaka. Cockerill also tried to measure such spectrums and failed to find such close relationships between temperature lift and sound spectrums.

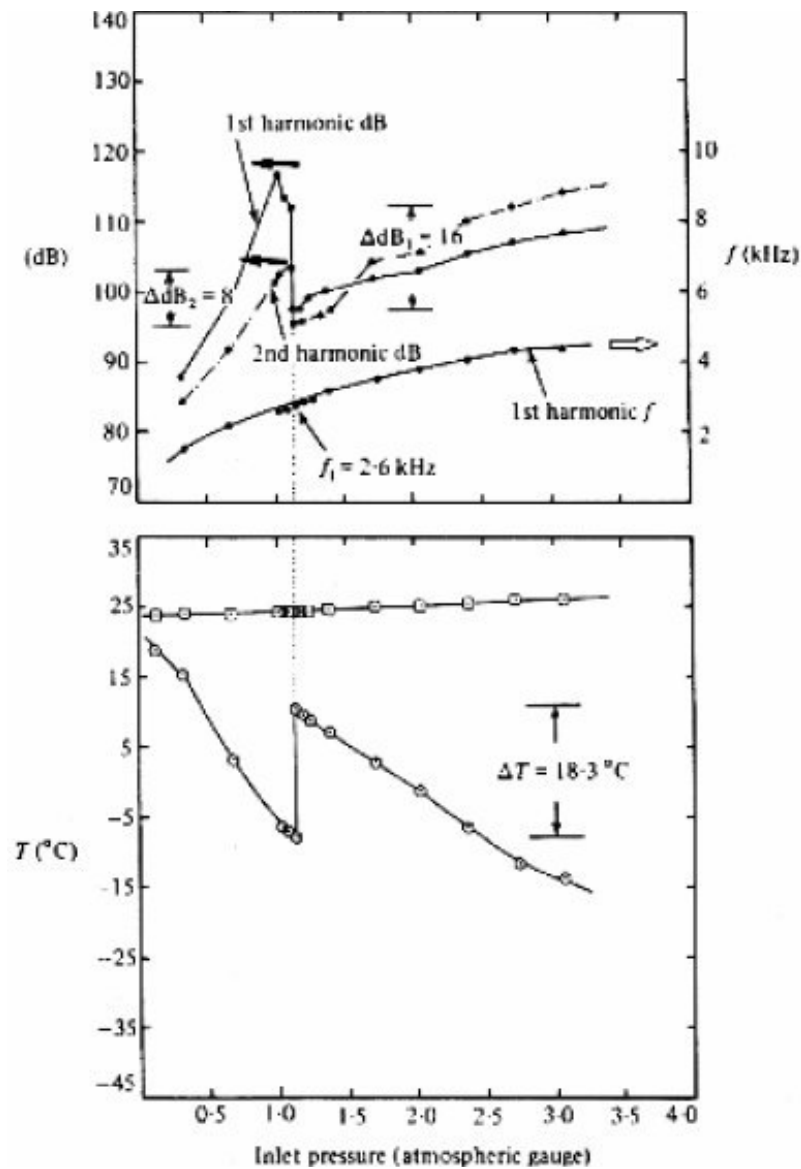


Fig. 2-9: Graph illustrating the behaviour of the energy separation, and the acoustical output from Kurosaka's tube as the excitation frequency is increased [24].

Suffice to say that this is not the limit of published operating theory on the RHVT. Additional conflicting theories have been published including for example, Harnett and Eckert [26] who invoke turbulent eddies, Stephan et al. [27] propose that Görtler vortices form on the inside wall of the vortex tube and drive the fluid motion, Camiré [28] attributes the energy separation to heat transfer from the cold region to the hot flow region during periods where the hot flows static temperature is less than that of the cold flow due to its large kinetic energy.

2.6 Previous CFD Studies.

Contributors to CFD studies on the mode of energy transfer within the RHVT are few. Easily found papers on this subject have been published by Promvong et al. [10], N.F. Aljuwayhel et al. [12], Frohlingsdorf et al. [21], Behera et al. [29] and Skye et al. [30].

N.F. Aljuwayhel et al. suggest that “by sub-dividing the computational region of the numerical model into control volumes associated with the hot and cold fluid streams it is possible to show that a work transfer associated with shears layers occurs”, i.e. frictional heat transfer explained in Section 2.3., of which Frohlingsdorf et al. [21], also agree. N.F. Aljuwayhel et al. also stress that the choice of the turbulence model has a large effect on the vortex tube’s predicted performance but it does not lead them to a different conclusion as to the mode of heat transfer. However Colgate et al. [31] have reservations about Frohlingsdorf and Unger’s work due to the fact that “an artificial enhancement of the Prandtl number by a staggering factor of 10 to fudge the unsteadiness” within their turbulence model.

Only Behera et al. [29] have previously published literature on a RHVT using a complete three dimensional vortex tube. Most researchers have simplified the analysis to either two dimensional models or three dimensional partial sectors of the flow. All previous studies have been small scale parametric studies, and although Behera et al. [29] have successfully captured secondary flow, as can be seen in Fig. 2-10 overleaf, they have not tried to suggest its thermodynamic influence in relation to Ahlborn et al. [17] and Gao et al. [18] heat pump cycle theory. They did however suggest that secondary flow may be a performance degradation mechanism and is best avoided. N.F. Aljuwayhel et al. [12] have also presented results of similar recirculating streamlines.

Behera et al. also found that the presence of secondary flow superimposed on the primary forced vortex for low values of d_c/D as reported by Ahlborn et al. [15]. They have also suggested that the transition to purely primary flow occurs as the d_c/D value is increased whereby the magnitude of secondary flow decreases and is completely eliminated for $d_c/D = 0.58$ (cold end diameter = 7 mm) as shown in Fig. 2-11 overleaf.

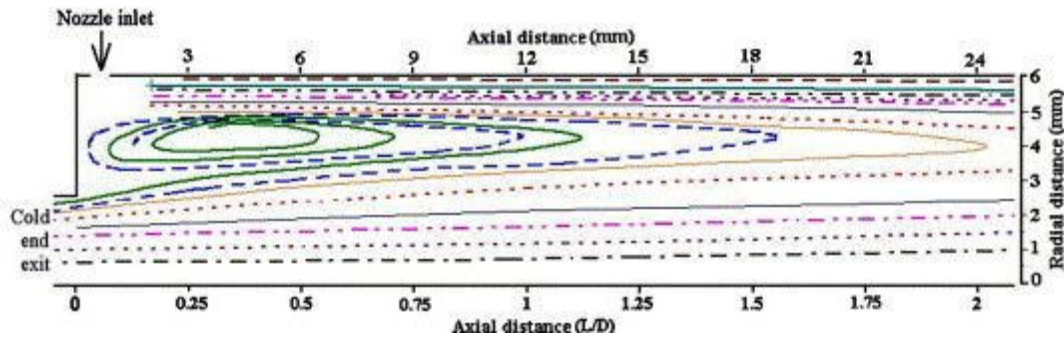


Fig. 2-10: Streamline plot of axial velocity on the central axis of a RHVT with $d_c/D = 0.417$ near the cold end exit zone [29].

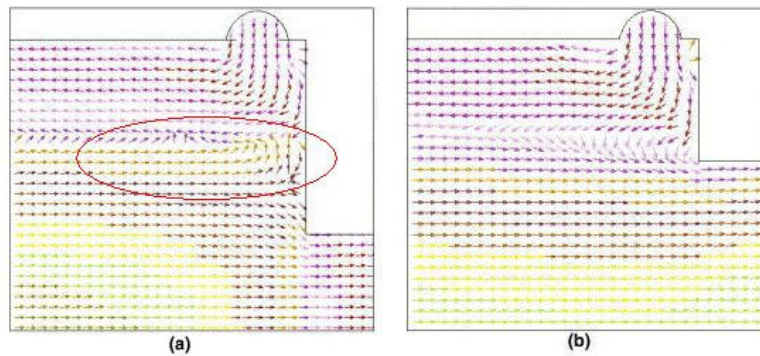


Fig. 2-11: Flow pattern near cold end exit for $d_c/D = 0.323$ showing secondary circulation flow; (b) flow pattern near cold end exit for $d_c/D = 0.58$ showing no secondary circulation flow [29].

2.7 Summary

In this section the current energy separation theory has been presented including heat migration explanations such as secondary flow acting as a heat pump and frictional heat transfer within the RHVT. The section ended with illustrations of CFD results in this area, and as such it marks a suitable point in which to develop the applications and theory of this software technology, which is the content of the next section.

3 Computational Fluid Dynamics

3.1 Introduction

Computational Fluid Dynamics or CFD is a computer-based tool for simulating the behaviour of systems involving fluid flow, heat transfer, and other related physical processes. CFD is now regarded as the “third” technique for the solution of fluid flow problems, complementing, but not replacing, the well-established approaches of theory and experiment. It is a relatively new branch of fluid mechanics and finds its niche in predicting fluid flows that are difficult or impossible to analyse using theory and are complex, time consuming, or expensive to measure experimentally.

3.2 The History of CFD

Computers have been used to solve fluid flow problems for many years. Numerous programs have been written to solve either specific problems, or specific classes of problems. From the mid-1970s, the complex mathematics required to generalise the algorithms began to be understood, and general purpose CFD solvers were developed.

These began to appear in the early 1980s and required what were then very powerful computers, as well as an in-depth knowledge of fluid dynamics, and large amounts of time to set up simulations. Consequently, CFD was a tool used almost exclusively in research. Recent advances in computing power, together with powerful graphics and interactive 3-D manipulation of models have made the process of creating a CFD model and analysing results much less labour intensive, reducing time and, hence, cost. Advanced solvers contain algorithms which enable robust solutions of the flow field in a reasonable time.

As a result of these factors, CFD is now an established industrial design tool, helping to reduce design timescales and improve processes throughout the engineering world. CFD provides a cost-effective and accurate alternative to scale model testing, with variations on the simulation being performed quickly, offering obvious advantages.

3.2.1 Uses of CFD

CFD is used by engineers and scientists in a wide range of fields. Typical applications include:

- **Process industry:** Mixing vessels and chemical reactors
- **Building services:** Ventilation of buildings, such as atria
- **Health and safety:** Investigating the effects of fire and smoke
- **Motor industry:** Combustion modelling, car aerodynamics
- **Electronics:** Heat transfer within and around circuit boards
- **Environmental:** Dispersion of pollutants in air or water
- **Power and energy:** Optimisation of combustion processes
- **Medical:** Blood flow through grafted blood vessels

CFD works by solving the equations of fluid flow (in a special form) over a region of interest, with specified (known) conditions on the boundary of that region. The governing equations of CFD utilise adapted forms of the governing equations of fluid flow and heat transfer which are given below for cartesian co-ordinates.

3.3 Navier – Stokes Equations

The Navier – Stokes equations in cartesian coordinates which govern the time – dependent, three – dimensional fluid flow and heat transfer of a compressible Newtonian fluid are given as follows from [32]:

Continuity Equation:

$$\frac{\partial \rho}{\partial t} + \text{div}(\rho \mathbf{U}) = 0 \quad (3.1)$$

x – momentum Equation:

$$\frac{\partial \rho u}{\partial t} + \text{div}(\rho u \mathbf{U}) = -\frac{\partial P}{\partial x} + \text{div}(\mu \text{ grad } u) \quad (3.2)$$

y – momentum Equation:

$$\frac{\partial \rho v}{\partial t} + \text{div}(\rho v \mathbf{U}) = -\frac{\partial P}{\partial y} + \text{div}(\mu \text{ grad } v) \quad (3.3)$$

z – momentum Equation:

$$\frac{\partial \rho w}{\partial t} + \text{div}(\rho w \mathbf{U}) = -\frac{\partial P}{\partial z} + \text{div}(\mu \text{ grad } w) \quad (3.4)$$

Energy Equation:

$$\frac{\partial \rho h_o}{\partial t} - \frac{\partial P}{\partial t} + \text{div}(\rho h_o \mathbf{U}) = \text{div}(\lambda \text{ grad } T_s) \quad (3.5)$$

Equations of State (ideal gas laws):

$$P = P(\rho, T_s), h_s = h_s(\rho, T_s), P = \rho R T_s, h_s = i + P/\rho, i = C_v T_s \text{ and } h_o = h_s + 1/2 \mathbf{U}^2 \quad (3.6)$$

where ρ , μ , \mathbf{U} , u , v , w , P and i denote density, viscosity, the velocity vector, the x , y and z components of the velocity vector, static pressure and the internal energy per unit mass respectively. When solved, these differential equation yield details about the velocity, density, pressure, etc., at every point throughout an entire flow domain of interest. These equations are coupled, meaning that some of the variables appear in all of the equations. As a result the set of equations must be solved simultaneously for each unknown. In addition boundary conditions for the variables must be specified at all boundaries of the flow domain, including inlets, outlets, and walls.

3.4 Governing Equations of CFD

In CFD however, adapted forms of the Navier – Stokes equations are used in the analysis of turbulent flows, such as those present within the RHVT. The governing equations of CFD are the Reynolds Averaged Navier – Stokes (RANS) equations which are obtained by time – averaging the general form of the Navier – Stokes equations. This process of time averaged equations is discussed in depth in Section A – Turbulence and Turbulence Modelling, where the RANS equations and a general Scalar Transport equation, can be seen. The governing equations of CFD are given as follows from [33]:

Continuity Equation:

$$\frac{\partial \rho}{\partial t} + \text{div}(\rho \mathbf{U}) = 0 \quad (3.7)$$

x – momentum Equation:

$$\frac{\partial \rho U}{\partial t} + \text{div}(\rho U \mathbf{U}) = -\frac{\partial P}{\partial x} + \text{div}(\mu_{\text{eff}} \text{ grad } U) \quad (3.8)$$

y – momentum Equation:

$$\frac{\partial \rho V}{\partial t} + \text{div}(\rho V \mathbf{U}) = -\frac{\partial P}{\partial y} + \text{div}(\mu_{\text{eff}} \text{grad } V) \quad (3.9)$$

z – momentum Equation:

$$\frac{\partial \rho W}{\partial t} + \text{div}(\rho W \mathbf{U}) = -\frac{\partial P}{\partial z} + \text{div}(\mu_{\text{eff}} \text{grad } W) \quad (3.10)$$

Energy Equation:

$$\frac{\partial \rho h_o}{\partial t} + \text{div}(\rho h_o \mathbf{U}) = \text{div}(\Gamma_{\text{eff}} \text{div } h_o) \quad (3.11)$$

where U , V and W are the mean x , y and z components of the velocity vector \mathbf{U} respectively as defined in Section A.2. These simplified equations have been formulated through the use of two new terms called the effective viscosity, μ_{eff} , and effective diffusivity, Γ_{eff} , defined as follows:

$$\mu_{\text{eff}} = \mu + \mu_t \quad (3.12)$$

$$\Gamma_{\text{eff}} = \Gamma + \Gamma_t, \Gamma = \frac{\mu}{\text{Pr}} \text{ and } \Gamma_t = \frac{\mu_t}{\text{Pr}_t} \quad (3.13)$$

where μ , μ_t , Pr and Pr_t are the viscosity, turbulent viscosity, Prandtl number and the turbulent Prandtl number respectively. Equations (3.12) and (3.13) can only express the turbulent fluctuation terms as a function of the mean variables of the RANS if the turbulent viscosity, μ_t , is known. It is the turbulence models, such as the $k - \varepsilon$ and $k - \omega$ models, that provide a value for μ_t , as also discussed in Section A and as can be seen for example in Equation (A.21).

Analytical solutions to these equations, (3.7) - (3.11) exist for only the simplest of flows under ideal conditions. To obtain solutions for real flows a numerical approach must be adopted whereby the equations are replaced by algebraic approximations which may be solved using a numerical method.

3.4.1 Discretisation of the Governing Equations of CFD

The numerical method employed in many CFD software packages, including the ANSYS CFX 10 package used in this study, involves discretising the spatial domain into finite control volumes using a mesh as shown in Fig. 3-1 overleaf. The governing

equations are integrated over each control volume, such that the relevant quantity (mass, momentum, energy etc.) is conserved in a discrete sense for each control volume.

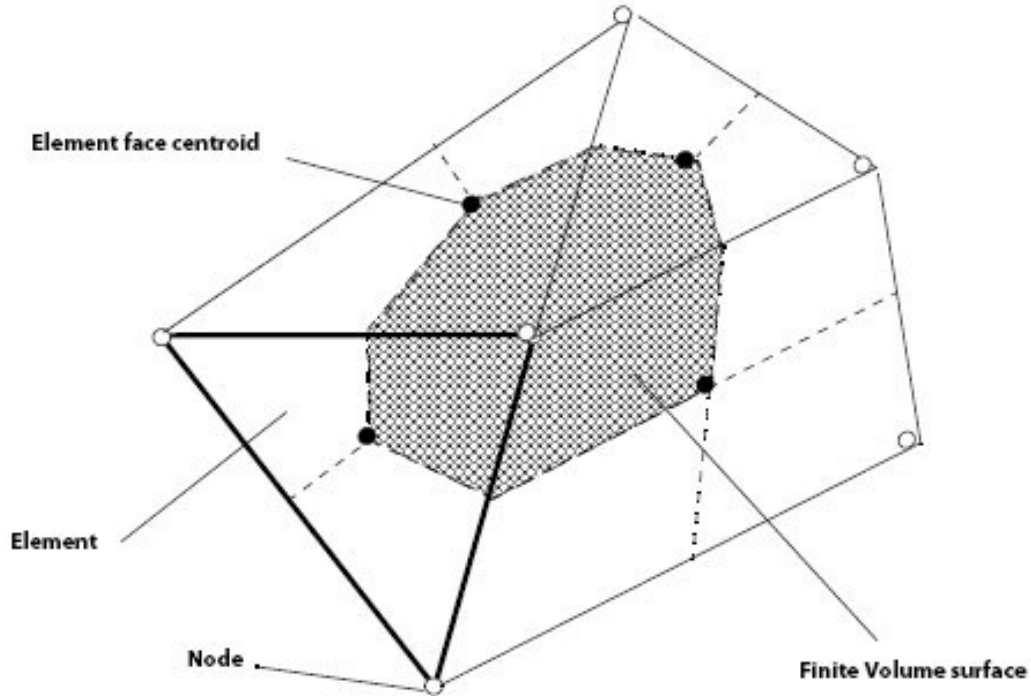


Fig. 3-1: Cell Vertex Finite Volume Scheme [33].

It is clear that each node is surrounded by a set of surfaces which comprise the finite volume, as shown in Fig. 3-1. All the solution variables and fluid properties are stored at the element nodes. The governing equations are integrated over a control volume, and Gauss’ divergence theorem is applied to convert some volume integrals to surface integrals. For control volumes that do not deform in time, the time derivatives can be moved outside of the volume integrals and the equations become:

Continuity Equation:

$$\frac{d}{dt} \int_V \rho dV + \int_s \rho U dn = 0 \tag{3.14}$$

x – momentum Equation:

$$\frac{d}{dt} \int_V U dV + \int_s \text{div}(\rho U U) dn = - \int_s P dn + \int_s \mu_{eff} (\text{grad } U) dn \tag{3.15}$$

y – momentum Equation:

$$\frac{d}{dt} \int_V V dV + \int_s \text{div}(\rho V \mathbf{U}) dn = - \int_s P dn + \int_s \mu_{eff} (\text{grad } V) dn \quad (3.16)$$

z – momentum Equation:

$$\frac{d}{dt} \int_V W dV + \int_s \text{div}(\rho W \mathbf{U}) dn = - \int_s P dn + \int_s \mu_{eff} (\text{grad } W) dn \quad (3.17)$$

Energy Equation:

$$\frac{d}{dt} \int_V h_o dV + \int_s \text{div}(\rho h_o \mathbf{U}) dn = \int_s \Gamma_{eff} (\text{grad } h_o) dn \quad (3.18)$$

where \mathbf{V} (not to be confused with V the y – component of the average velocity) and s respectively denote volume and surface regions of integration, and dn are the differential Cartesian components of the outward normal surface vector in the direction of interest. The first step in solving these continuous equations numerically is to approximate them using discrete functions, an example of which is outlined below.

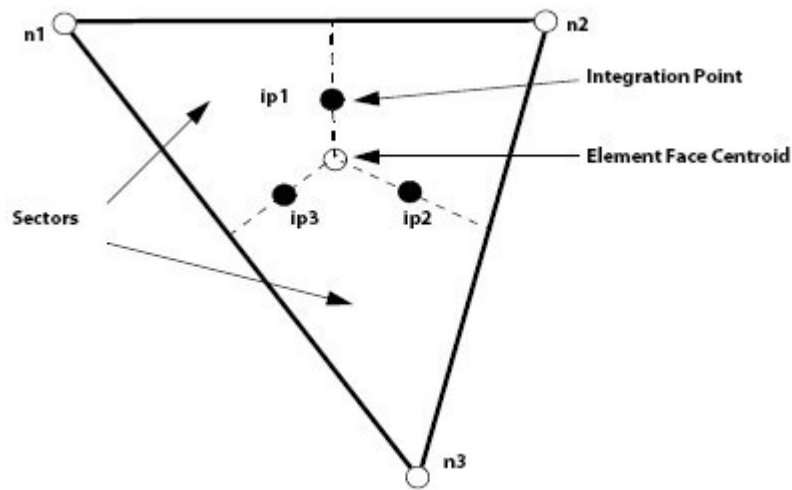


Fig. 3-2: Isolated mesh element and its associated integration points [33].

Considering an isolated mesh element such as the one shown above, the surface fluxes must be discretely represented at the integration points to complete the conversion of the continuous equation into their discrete form. The integration points, ip_n , are located at the centre of each surface segment in a 3D element surrounding the finite volume. Using a First Order Backward Euler scheme the discrete form of the integral equations are written as:

Continuity Equation:

$$\mathbf{V} \left(\frac{\rho - \rho^o}{\Delta t} \right) + \sum_{ip} (\rho \mathbf{U} \Delta n) = 0 \quad (3.19)$$

x – momentum Equation:

$$\mathbf{V} \left(\frac{\rho U - \rho^o U^o}{\Delta t} \right) + \sum_{ip} \dot{m}_{ip} (U) = \sum_{ip} P \Delta n + \sum_{ip} (\mu_{eff} (grad U) \Delta n) \quad (3.20)$$

y – momentum Equation:

$$\mathbf{V} \left(\frac{\rho V - \rho^o V^o}{\Delta t} \right) + \sum_{ip} \dot{m}_{ip} (V) = \sum_{ip} P \Delta n + \sum_{ip} (\mu_{eff} (grad V) \Delta n) \quad (3.21)$$

z – momentum Equation:

$$\mathbf{V} \left(\frac{\rho W - \rho^o W^o}{\Delta t} \right) + \sum_{ip} \dot{m}_{ip} (W) = \sum_{ip} P \Delta n + \sum_{ip} (\mu_{eff} (grad W) \Delta n) \quad (3.22)$$

Energy Equation:

$$\mathbf{V} \left(\frac{\rho h_o - \rho^o h_o^o}{\Delta t} \right) + \sum_{ip} \dot{m}_{ip} (h_o) = \sum_{ip} (\mu_{eff} (grad h_o) \Delta n) \quad (3.23)$$

where the subscript ip denotes an integration point, the summation is over all the integration points of the finite volume, Δn is the discrete outward surface vector and Δt is the time-step. The transient term has no bearing on a steady state solution such as that for a RHVT. After large times, the solution approaches a steady state, where the time derivatives approach zero. This time – marching approach is widely used in modern CFD and provides greater numerical convergence stability and frequently leads to faster convergence to the steady state solution [34]. Indeed for steady state problems the time-step behaves like an ‘acceleration parameter’, to guide the approximate solutions in a physically based manner to a steady-state solution. This reduces the number of iterations required for convergence to a steady state, or to calculate the solution for each time step in a time dependent analysis [33]. Superscripts, o , above refer to the old time level. For the advection terms, ρ , U , V , W and h_o above, there is a choice of different discretisation schemes including an Upwind Differencing Scheme, which is numerically more stable than the choice of a

Higher Resolution Scheme, which may be more accurate. The discrete mass flow through a surface of the finite volume is denoted by and is given by:

$$\dot{m}_{ip} = (\rho \mathbf{U} \Delta n) \quad (3.24)$$

These equations relating to fluid flow can be closed numerically by the specification of conditions on the external boundaries of a domain. It is the boundary conditions that produce different solutions for a given geometry and set of physical models. Hence boundary conditions determine to a large extent the characteristics of the solution obtained. Therefore, it is important to set boundary conditions that accurately reflect the real situation to allow you to obtain accurate results.

3.5 Boundary Conditions

The types of boundary condition that can be applied depend upon what sort of boundary or interface the boundary condition is placed on. The following fluid boundary condition types are available in ANSYS CFX 10:

1. **Inlet** - fluid is constrained to flow into the flow domain only.
2. **Outlet** - fluid is constrained to flow out of the flow domain only.
3. **Opening** - fluid can simultaneously flow both in and out of the flow domain. This is not available for flow domains with more than one fluid present.
4. **Wall** - impenetrable boundary to fluid flow.
5. **Symmetry Plane** - a plane of both geometric and flow symmetry.
6. **Periodic**- In many practical situations, a portion of the flow field is repeated in many identical regions e.g. the flow around a single turbine blade in a rotating machine. These problems are said to exhibit rotational or translational periodicity. Although the complete flow problem can be modelled, it is more efficient to model the flow in a single periodic region and apply periodic boundary conditions at faces which connect them, allowing flow out of one boundary to flow into the corresponding boundary.

In addition to fluid boundaries the following solid boundary condition types are also available in ANSYS CFX 10:

1. **Wall** - impenetrable boundary to fluid flow.
2. **Symmetry Plane** - a plane of both geometric and flow symmetry.

For a given computational domain, boundary conditions can be applied that over-specify or under-specify the problem. This usually results in non-physical solutions or failure of the solution to converge. It is important, therefore, to understand the meaning of well-posed boundary conditions. The best way to determine if the boundary conditions are well posed is to ask the question “Could the problem defined in the CFD study be physically recreated in a laboratory?”. This is why it is so important in any CFD study to have comparative accurate experimental results in order to direct the ANSYS CFX 10 solver to realistic results.

3.6 Solution Strategy of the ANSYS CFX 10 Solver

In order to solve for a flow problem the solver must be supplied with an appropriate flow domain, including a finite volume mesh along with appropriate boundary conditions. When supplied with this information the ANSYS CFX 10 solver employs a solution strategy where the momentum equations are first solved, using a guessed pressure. Because of the ‘guess-and-correct’ nature of the linear system, a large number of iterations are typically required in addition to the need for judiciously selecting relaxation parameters for the variables.

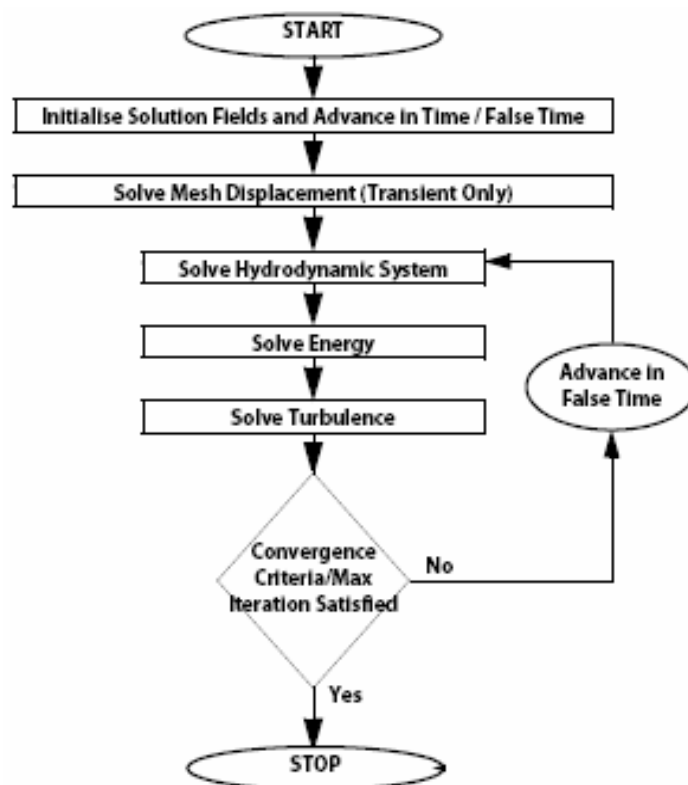


Fig. 3-3: Solver solution procedure for a steady, compressible, turbulent flow with thermal gradients [33].

ANSYS CFX 10 uses a coupled solver, which solves the hydrodynamic equations (for U , V , W , P) as a single system. This solution approach uses a fully implicit discretisation of the equations at any given time step. The flow chart shown in Fig. 3-3 illustrates the general solution procedure. In addition to the general solution procedure utilised by the solver, any user of commercial CFD such as ANSYS CFX 10 must follow standard methodology in order to solve complex fluid dynamic problems with the solver. This methodology normally utilises complementary additional software modules in a process outlined below.

3.7 CFD Methodology

Now that the theoretical aspects of CFD have been covered it can now be shown how the process of performing a single CFD simulation is split into four components which are:

1. Creating the geometry and mesh.
2. Definition of the physics of the fluid flow.
3. Solving for a solution of the fluid flow.
4. Post-processing of the results.

In order to do this, in ANSYS CFX 10 there consists five software modules which are linked by the flow of information required to perform a CFD analysis:

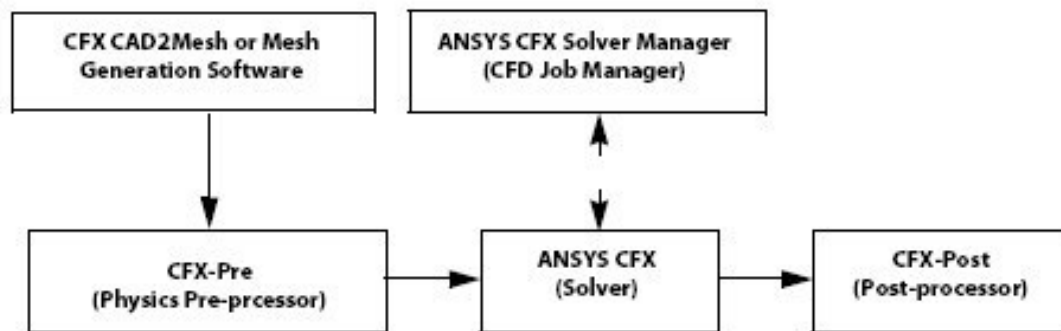


Fig. 3-4: Software modules available in ANSYS CFX 10 [35].

As already stated the process of performing a CFD simulation begins with creating the geometry and a mesh based on this drawn computational flow domain.

3.7.1 Creating the Geometry and Mesh

The first objective is to produce a mesh for input to the physics pre-processor. Before a mesh can be produced, a closed geometric solid is required. The geometry and mesh are created in CAD and meshing packages respectively.

The basic steps involve:

1. Defining the geometry of the region of interest.
2. Creating regions of fluid flow, solid regions and surface boundary names.
3. Setting properties for the mesh.

3.7.2 Definition of the Physics of the Fluid Flow

These mesh files are then loaded into the physics pre-processor, ANSYS CFX 10-Pre along with fluid properties and boundary condition specification.

3.7.3 Solving for a Solution of the Fluid Flow

These physical definitions along with the mesh are then loaded into the solver. The algebraic governing equations of CFD are solved iteratively to satisfy the boundary conditions of the flow domain. An iterative approach is required because of the non-linear nature of the equations, and as the solution approaches the exact solution, it is said to converge.

3.7.3.1 Residuals

For each iteration, an error, or residual, is reported as a measure of the overall conservation of the flow properties. The raw residual is calculated as the imbalance of each governing equation of CFD for each iteration to the next. The raw residuals are then normalised for the purpose of solution monitoring and to obtain a convergence criteria. How close the final solution is to the exact solution depends on a number of factors, including the size and shape of the control volumes and the size of the final residuals. Once a convergence target is met the solver will then produce a results file which is then passed to the post-processor.

3.7.4 Post-Processing of the Results

The post-processor is the module employed to analyse, visualise and present the results of the converged solution interactively. Examples of some important features of post-processors are:

- Visualisation of the geometry and control volumes.
- Vector plots showing the direction and magnitude of the flow.

- Visualisation of the variation of scalar variables (e.g. temperature, pressure and velocity) through the domain.
- Quantitative numerical calculations.
- Animation.
- Charts showing graphical plots of variables.
- Hardcopy output.

3.8 Summary

In this chapter the fundamental principles of CFD have been addressed including an insight into standard CFD methodology and the essential requirements in order to gain a successful solution to a flowfield problem. However, before a CFD analysis of the RHVT was conducted, a preliminary validation of CFD principles was carried out in order to demonstrate the authors proficiency in applying this technology to an established fluid dynamics problem; this study can be seen in Appendix B – Flat Plate Boundary Layers. Following this validation process, the study moved back to the RHVT, where the CFD analysis began with capturing the total temperature distribution within the tube equivalent to that found by experimental researchers. This is the subject of the next chapter of this thesis.

4 CFD Analysis of the RHVT

4.1 Introduction

Now that CFD methodology has been developed and the known characteristics of the RHVT have been established, along with theories advanced by numerous authors into how the tube generates its remarkable temperature drop, can this CFD analysis of the vortex tube begin. But before any conclusions into the mode of heat transfer within the RHVT can be made, known properties of the vortex tube must be verified including:

- Cold outlet temperature drop i.e. $\Delta T_{o,c} = T_{o,in} - T_{o,c}$.
- Tangential velocity profile at the entrance region.
- Axial velocity profile at the entrance region.
- Confirmation of the presence of secondary flow.
- Confirmation of a location of a stagnation point in the flow.

4.2 Procedure Adopted

It will be shown in due course that each of these properties have been confirmed as a result of the following steps undertaken to arrive at a computational model with the ability to satisfy all known RHVT criteria. The steps undertaken in order to accomplish this were as follows:

1. Published experimental results of thermal outputs and internal velocities using similar vortex tubes were found in order to finalise the dimensions of the vortex tube to be modelled.
2. A computational domain was drawn using the dimensions of the experimental vortex tubes with the CAD component of the ANSYS CFX 10 software.
3. Boundary conditions were applied using the known input conditions supplied to the vortex tubes recorded by the experimental authors.
4. A mesh convergence study was performed using the cold outlet total temperatures recorded by the experimental authors as a target for grid convergence.

5. Once a mesh independent solution was obtained, the optimum turbulence model available in ANSYS CFX 10 for analysing vortex tube flows was established.
6. Using this optimum turbulence model an investigation into the mode of heat transfer was conducted.

What follows is the first of the steps above which was establishing comparable experimental results which could be used to throughout this CFD study of the RHVT.

4.3 Utilised Experimental Results

As already stated in Section 3.5 CFD results should never be accepted without validation against available experimental or other CFD data. In order to satisfy this requirement experimental and CFD results of many researchers have been analysed. This selection of comparable results has focused on those authors who have documented the cold thermal output of the RHVT in relation to the cold fraction distribution along with additional information regarding the geometry of the device, and has resulted in the following table of relevant published results.

Author	Research Method	P_{in} (Bar Gauge)	d_c/D	L/D	No. of Nozzles	Ref No.
Gao, C. M.	Expt.	6.5	0.25	13	1	[7]
Promvongse et al.	Expt.	2	0.5	45	1 – 4	[10]
Soni, Y.	Expt.	0.34 – 2.04	0.15–0.55	10-50	2	[11]
Aljuwayhel et al.	CFD	2	0.32	5	1	[12]
Ahlborn et al.	Expt.	3	–	10	–	[15]
Behera et al.	CFD	4.42	0.42-0.625	10 – 35	1 – 6	[29]
Saidi et al.	Expt.	1 – 3	0.5	20 – 55.5	3 – 4	[36]

Table 4-1: Previous publishers of the variation of ΔT_c with μ_c in a RHVT and their respective configurations.

In order to have more than one source of comparison, the results of Promvongse et al. [10] and Soni [11] results have been utilised, as their experimental results have been ascertained from common vortex tube geometry and air supply conditions. From this study, Fig. 1–7 has been produced and these comparative results are used in the mesh convergence studies shown later in Table 4-2 and Fig 4-12 respectively. Internal velocity profiles will be compared to the experimental results published by Gao et al. [7], as their results are, to the best of the author's knowledge, the most recent and

comprehensive results published for both tangential and axial velocities. The profiles from Gao et al. are given below in Fig. 4-1 where, v_{max} is the maximum value of the tangential velocity, v , utilised in order to normalise the results.

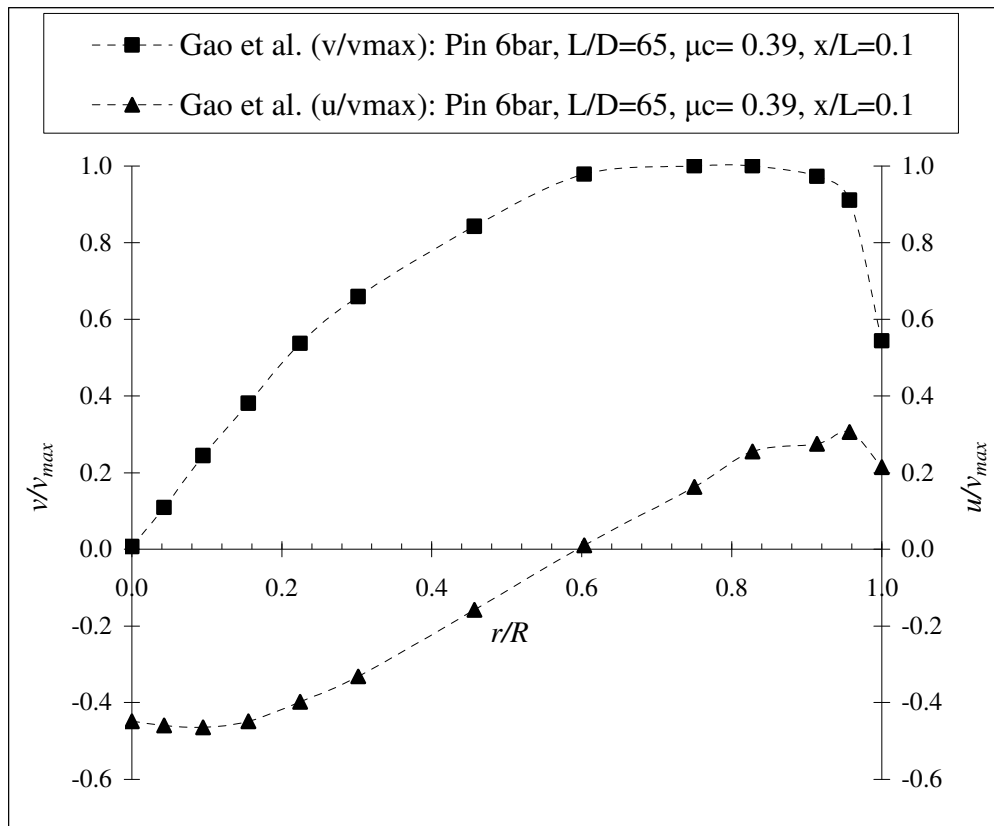


Fig. 4-1: Experimental results of internal normalised tangential and axial velocities at normalised radial locations from [7] at the inlet region within the RHVT.

4.4 RHVT CFD Model

Previously shown in Fig. 1-3 are the components that comprise a commercial RHVT. However, for the purposes of CFD analysis, this complicated shape can be resolved down to a very simple model without the loss of the most important aspects of the device. From the exploded view of a commercial vortex tube in Fig. 1-3 the only elements required are

- A cylindrical tube.
- A vortex generator at the entrance plane.
- A central hole for the cold outlet.
- An outlet on the periphery of the tube for the hot outlet.

These requirements have resulted in the basic shape as shown in Fig. 4-2, Fig. 4-3, Fig. 4-4 and Fig. 4-5 overleaf for analysis by the ANSYS CFX 10 software. The geometry of this RHVT is the same size as that used by Promvonge et al. [10] and

Soni [11] in their experiments. However the length of the tube has been shortened considerably as previously stated in Section 1.5.2. This shortening saves a considerable amount of computational effort, both memory wise and CPU processing time.

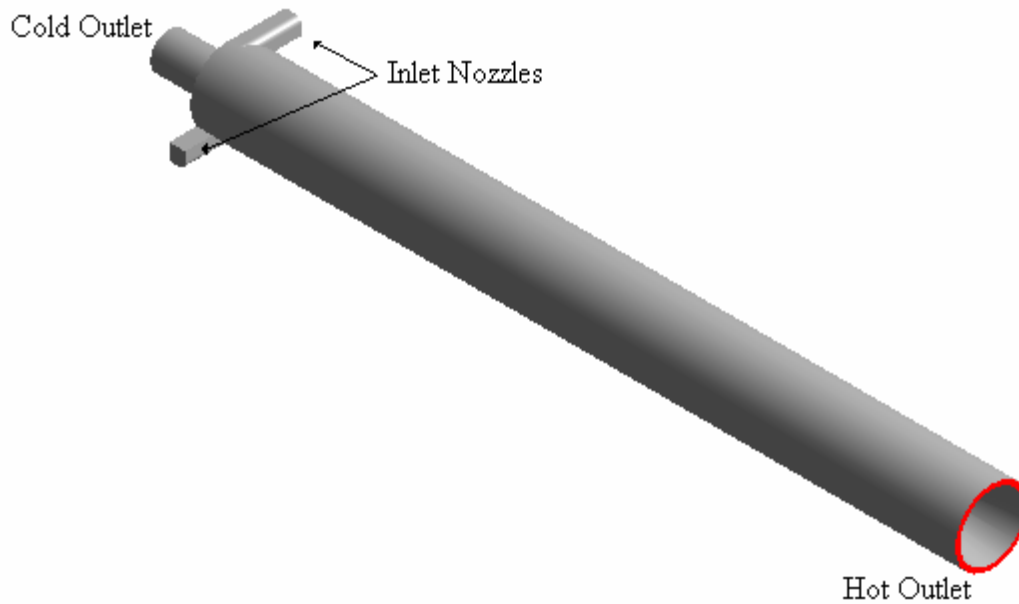


Fig. 4-2: Isometric view of the CFD model of the 3D RHVT with two inlet nozzles, cold outlet and a conical hot outlet.



Fig. 4-3: Plan view of the CFD model of the 3D RHVT with two inlet nozzles, cold outlet and a conical hot outlet.

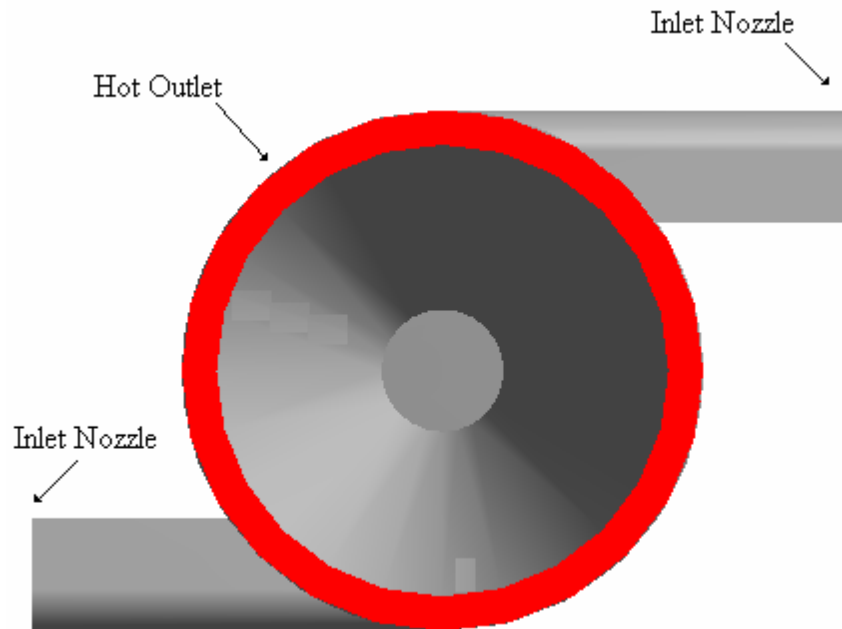


Fig. 4-4: Hot outlet end view of the CFD model of the 3D RHVT with two inlet nozzles and a conical hot outlet.

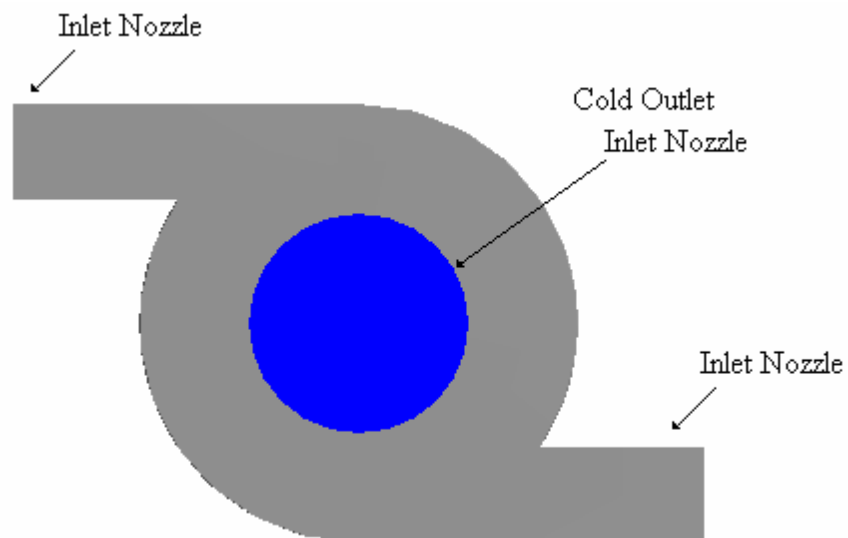


Fig. 4-5: Cold outlet end view of the CFD model of the 3D RHVT with two inlet nozzles and the cold outlet.

The elongated cold outlet as shown in Fig. 4-2 and Fig. 4-3 has been included because of the secondary flow in the RHVT. If the cold outlet was placed on the main body of the RHVT, it could cause significant problems for any outlet boundary condition specified, as secondary flow may recirculate at the outlet. Thus any flow trying to re-enter the domain would affect the solution considerably. Also as can be seen above the vortex generator of Fig. 1-3 has been simplified by only including the relevant nozzles.

4.5 Boundary Conditions

Previous publications have successfully implemented total pressure and static temperature at the inlet nozzles along with static pressures at the outlets as boundary conditions [12, 29, 30]. However to implement these conditions, the total pressure at the inlet must be calculated and as a result a sufficient static pressure drop through the RHVT may not occur. This is because the total pressure specification at the inlet is proportioned out as both static and dynamic pressure and this may mean an insufficient static pressure drop is calculated by the ANSYS CFX 10 solver.

Importantly, experimental researchers recorded information regarding the gauge pressure and temperature at the inlet. It would appear that these recorded values appear to be the most useful boundary conditions at this location. Significantly, the temperature at the outlets of the RHVT published by these researchers is the total/stagnation temperature of the fluid. This is because the temperature measurement probe creates a stagnation point in the high speed air flow, as also concluded by Skye et al. [30]. The resulting boundary conditions that were applied are as follows:

4.5.1 Nozzle Inlet

The static pressure was set to 2 Bar gauge along with a total temperature of 296.5 K at the inlet. This was in conjunction with the utilised experimental results of Promvonge et al. [10] and Soni [11]. The total temperature used at the inlet provides a basis for calculating and limiting the mass flow through the domain.

4.5.2 Cold Outlet

The static pressure at the cold outlet was set to atmospheric pressure (0 Bar gauge) as this outlet is open to the atmosphere.

4.5.3 Hot Outlet

The static pressure at the hot outlet was set to 0.5 Bar gauge. This was in order to obtain a cold fraction, $\mu_c \approx 0.4$, as required in order to compare predicted and experimental results in the mesh convergence study later on in Table 4-2 and Fig 4-12. The pressure at the hot outlet of the computational domain is always above atmospheric. This is because the hot valve in an actual RHVT serves to increase the back pressure at the peripheral outlet before the valve which is where the computational outlet is located.

4.5.4 Periodic Boundaries

Rotational periodic boundary conditions have also been applied to the computational RHVT, at the periodic faces shown in Fig. 4-6. The use of this boundary condition is only applicable to even number inlet nozzle RHVTs, where the flow is periodic in the circumferential direction with a period of $2\pi/n$ where n is the number of inlet nozzles. This rotational periodicity exists about the central axis on boundaries of sectors of the vortex tube defined by each inlet nozzle, as illustrated below in Fig. 4-6. This approach has led to substantial savings in the computational mesh, as the volume of the domain has been halved, resulting in the computational domain below.

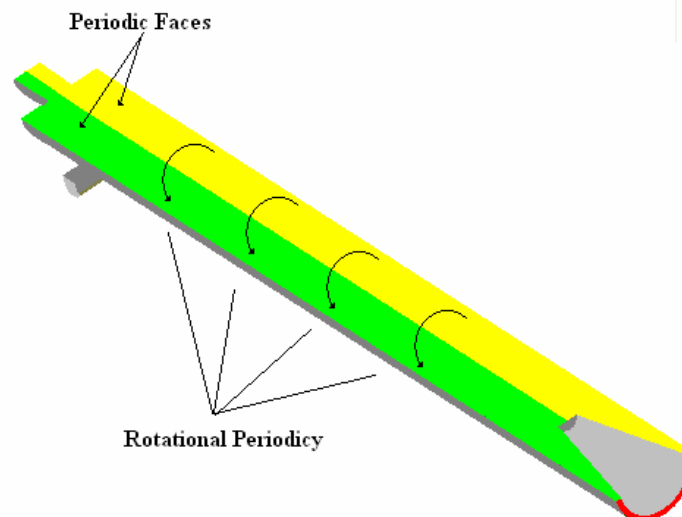


Fig. 4-6: Utilised CFD model of the halved RHVT highlighting the rotational periodicity property of a vortex tube with an even number inlet nozzles and the periodic faces on the central axis of the RHVT.

4.6 Mesh Convergence Study

A mesh convergence study focusing on both the static and total temperature outputs of the RHVT was conducted. The flow chart below summarises the procedure used to perform this mesh convergence study of the computational model of the RHVT.

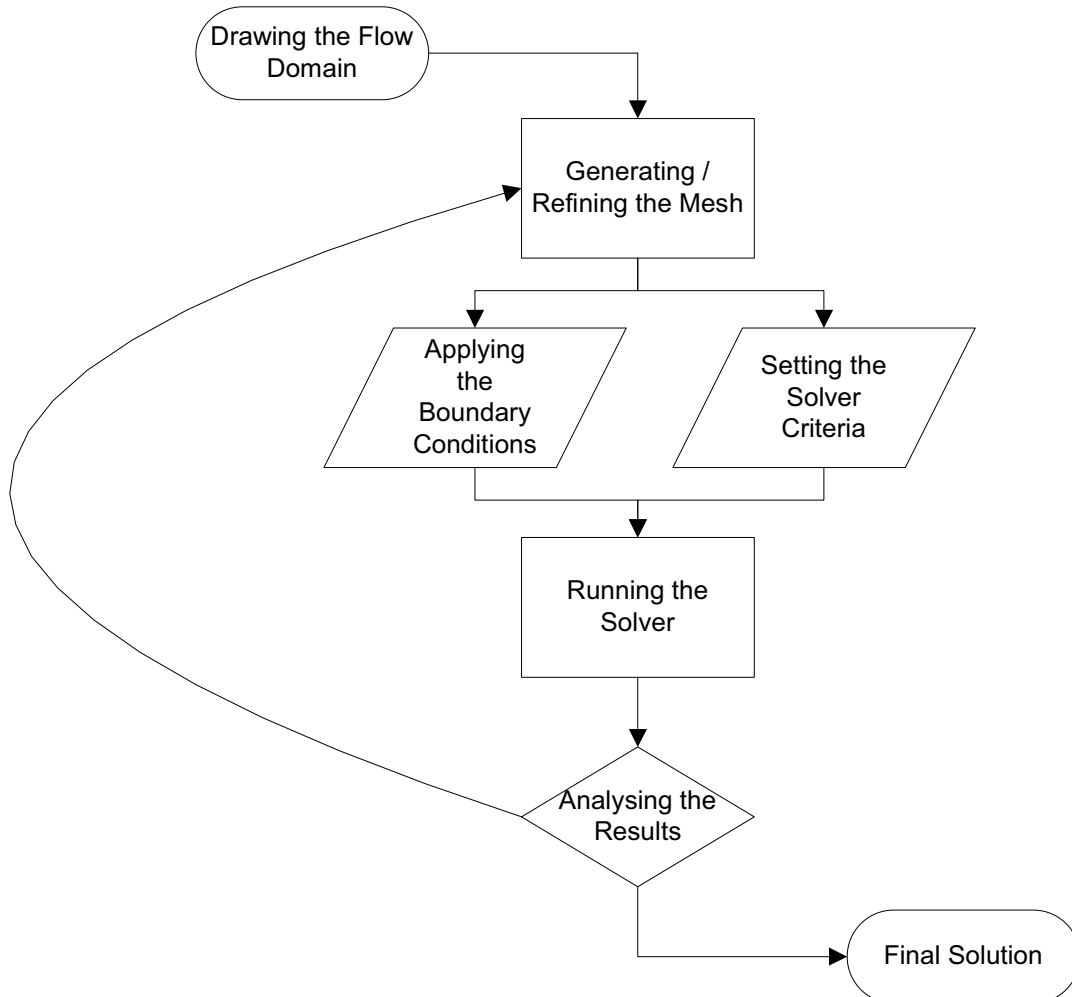


Fig. 4-7: Flow chart of the procedure used to ascertain a mesh independent solution.

This study was carried out in order to ascertain a mesh density such that any potential increase in the number of elements/nodes above the largest solved mesh density would yield a marginal increase in accuracy of CFD results, insufficient to warrant any increase in mesh density. This final mesh density was then used with confidence for comparative and analytical studies of factors such as choice of turbulence model and changes in dimensional variables of the RHVT. The results of this required mesh convergence study are shown overleaf and it has focused on the most important characteristic of the RHVT, i.e. the thermal output.

Mesh	No. of Elements	No. of Nodes	Average Control	Utilised	$T_{s,c} - T_{s,in}$ (K)	$T_{s,h} - T_{s,in}$ (K)	$T_{o,c} - T_{o,in}$ (K)	$T_{o,h} - T_{o,in}$ (K)
			Volume at each Node (mm ³)	RAM (GB)				
1	6902	1705	4.4065	0.02	33.8	34.4	0.0	0.1
2	444770	85863	0.0875	0.2	20.1	23.0	0.0	0.1
3	1567678	285071	0.0264	0.6	10.2	21.1	-4.7	2.9
4	5511274	978352	0.0077	2.0	6.4	19.5	-6.7	4.0
5	8571077	1522948	0.0049	2.9	5.0	20.6	-8.4	4.9

Table 4-2: Mesh convergence study for a RHVT subject to values of $\mu_c=0.4$, $P_{in}=2\text{Bar}$ and $L/D=10$, using the $k-\varepsilon$ turbulence model.

Included in Appendix C – Solver Output File for Mesh No. 2 is a summary of the solver run for Mesh No. 2, where the definition of the fluid flow including the boundary conditions and turbulence model criteria along with an interpolation of the results of Mesh No. 1 as the initial values of Mesh No. 2 and a brief convergence history of this solver run can be seen. The Average Node Density above was used as a means of measuring the average distribution of calculable nodes within the CFD model for performance analysis.

Fig. 4-8 and Fig 4-9 are shown overleaf to illustrate both the density of elements and contrasting difference between the first (Mesh No. 1) and final (Mesh No. 5) meshes utilised in the mesh convergence study of Table 4-2. In the initial mesh of Fig. 4-8 it can be seen that the mesh has been structured in such a way so as to concentrate elements in the entrance and exit regions of the RHVT. The same approach was used to develop the final mesh. However as can be seen in Fig. 4-9, the density of the 8,571,077 elements and 1,522,948 nodes within the RHVT is of such a scale as to make the view of these elements and nodes non-transparent, when the full axial view of the RHVT is displayed. In order to appropriately illustrate Mesh No. 5 zoomed in views from different perspectives of the RHVT have been included in Fig. 4-10 and Fig. 4-11.

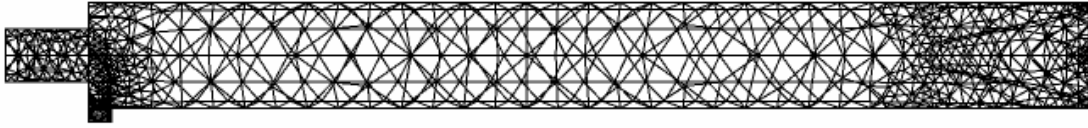


Fig. 4-8: Axial view of Mesh No. 1 from the mesh convergence study of Table 4-2.



Fig. 4-9: Axial view of Mesh No. 5 from the mesh convergence study of Table 4-2.

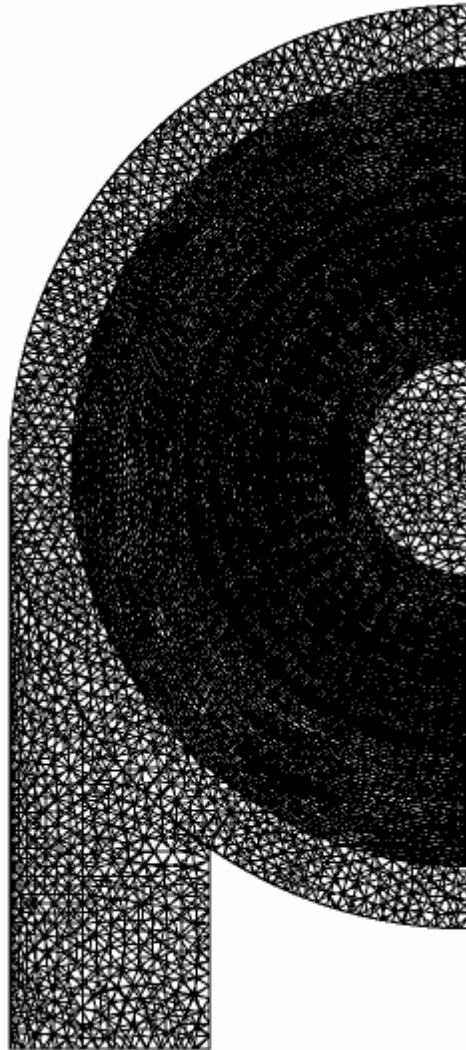


Fig. 4-10: Zoomed view of Mesh No. 5 when viewed from the right hand side of the RHVT as shown in Fig: 4-9.

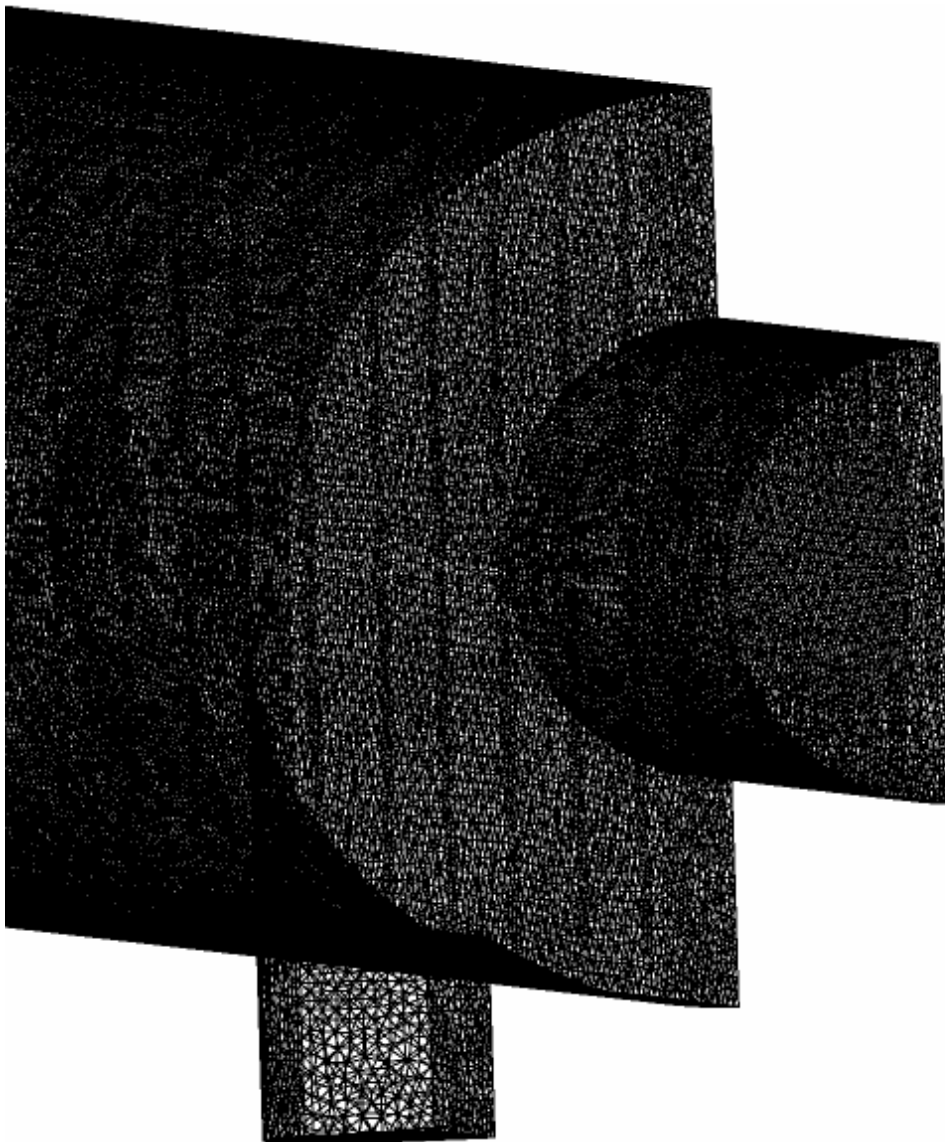


Fig. 4-11: Isometric view of Mesh No. 5 when viewed from the left hand side of the RHVT as shown in Fig: 4-9.

Finally the utilised Random Access Memory (RAM) of each mesh run has been recorded in Table 4-2 above so as to demonstrate the level of RAM addressed by the ANSYS CFX 10 software in order to numerically solve the RHVT problem. A graph of the information within Table 4-2, can be seen in Fig. 4-12, where the total temperature drop ($T_{o,c} - T_{o,in}$) at the cold outlet in the computational RHVT, has developed at quite high mesh densities, but has not yet reached the target temperature drops specified by the experimental results from [10] and [11].

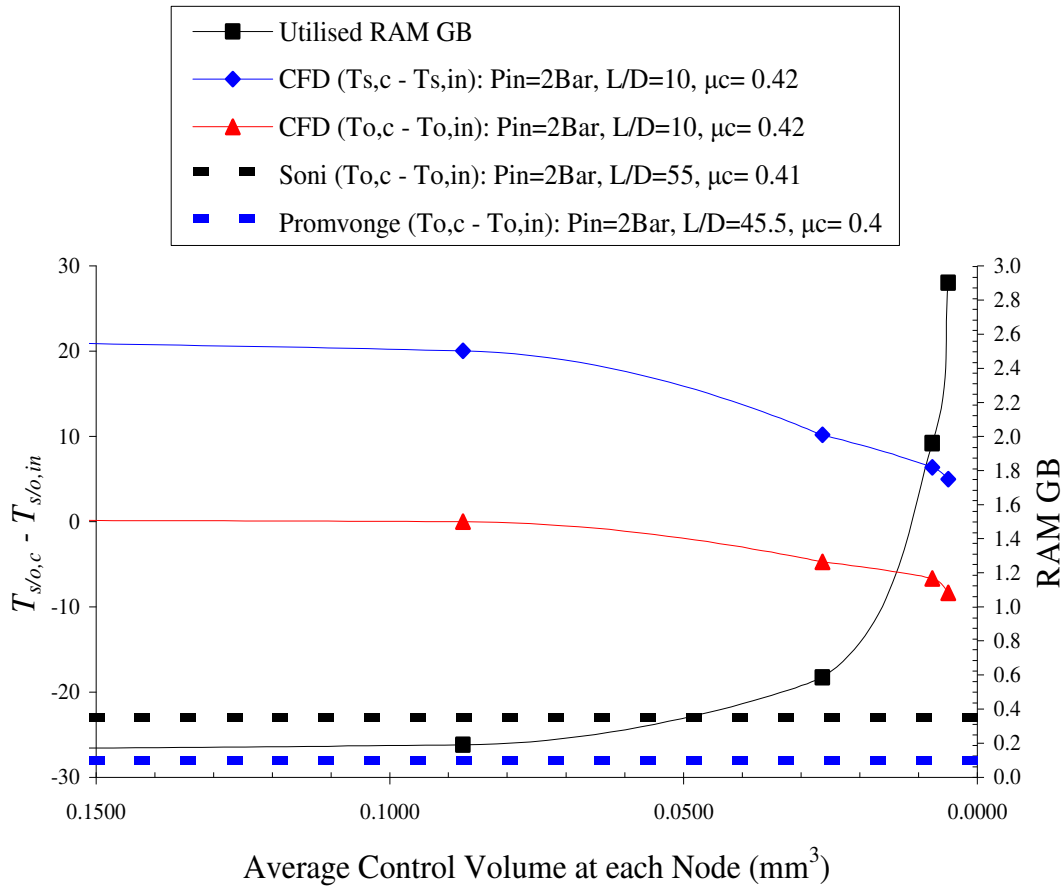


Fig. 4-12: CFD mesh convergence study for a RHVT similar to [10] and [11]. The graph shows the variance of the cold outlet total temperature drop ($T_{o,c} - T_{in,c}$) and cold static temperature difference ($T_{s,c} - T_{in,c}$) versus the mesh density in the form of the average control volume at each node. The targeted computed total temperature drop from the experimental results of [10] and [11] are highlighted along with the utilised RAM for each CFD run.

However, as the RAM, required by the ANSYS CFX 10 software to solve for all the variables in the governing equations of CFD at each node of the computational domain, has risen exponentially, as can be seen in Fig. 4-12, in comparison to small increases in the temperature drop out of the computational RHVT, it was therefore deemed unnecessary to further increase the mesh density of this mesh convergence study. It should be also noted that RAM requirements of this nature are extremely computationally intensive with solver run-times in excess of one week. From this study all further analysis of the RHVT have been conducted on Mesh No. 5 in Table 4-2, which incorporates 8,571,077 elements and 1,522,948 calculable nodal points.

4.7 Turbulence Model Performance

Following the mesh convergence study detailed above, the optimum performing turbulence model was ascertained. In order to do this, the results from each of the utilised turbulence models were compared for their ability to capture total temperature drops at the cold outlet and internal velocity profiles in comparison to the experimental results illustrated previously.

4.7.1 Thermal Performance

Comparative temperature output results for both the $k - \varepsilon$ and SST turbulence models were ascertained relatively easily as can be seen in the table below, where the $k - \varepsilon$ turbulence model outperformed the SST model substantially. This can be seen in Table 4-3 below, where the total temperature drop ($T_{o,c} - T_{o,in}$) at the cold outlet, from the results of the $k - \varepsilon$ turbulence model are much closer to that of the experimental results of Fig. 4-12.

Turbulence Model	$T_{s,c} - T_{s,in}$ (K)	$T_{s,h} - T_{s,in}$ (K)	$T_{o,c} - T_{o,in}$ (K)	$T_{o,h} - T_{o,in}$ (K)
$k - \varepsilon$	5.0	20.6	-8.4	4.9
SST	9.9	18.4	-2.9	2.0

Table 4-3: Thermal output of a RHVT subject to values of $\mu_c=0.4$, $P_{in}=2\text{Bar}$ and $L/D=10$, using the $k-\varepsilon$ and SST turbulence models respectively.

Despite this the contour plots of total temperature from both of these turbulence model runs are quite similar in distribution as can be seen in Fig 4-14 and Fig. 4-15 overleaf. What can be seen is the vast difference in the total temperatures at the cold outlet. Additional contour plots of static temperature, density, axial velocity, tangential velocity and radial velocity are also illustrated from the same results of the $k - \varepsilon$ and SST turbulence models using Mesh No. 5 of Table 4-2 in Fig. 4-17, Fig. 4-18, Fig. 4-20, Fig. 4-21, Fig. 4-23, Fig. 4-24, Fig. 4-26, Fig. 27, Fig. 29 and Fig. 4-30; where again all respective contour plot have similar characteristics. The same contour plots from the results of Mesh No.1 using the $k - \varepsilon$ turbulence model have also been included in Fig. 4-13, Fig. 4-16, Fig. 4-19, Fig. 4-22, Fig. 25 and Fig. 28, so as to demonstrate the development of the flowfield within the RHVT from the mesh convergence study of Table 4-2. In Fig. 4-13, Fig. 4-14 and Fig. 4-15 it can be easily shown that the total temperature distribution in each contour plot follows the adiabatic

mixing equation of Equation (1.7), approximately with negligible numerical error, e.g. for Fig. 4-13:

$$T_{o,in} = \mu_c T_{o,c} + (1 - \mu_c) T_{o,h}$$

$$296.5K \approx 0.4(281K) + 0.6(302K)$$

$$296.5K \approx 293.6K$$

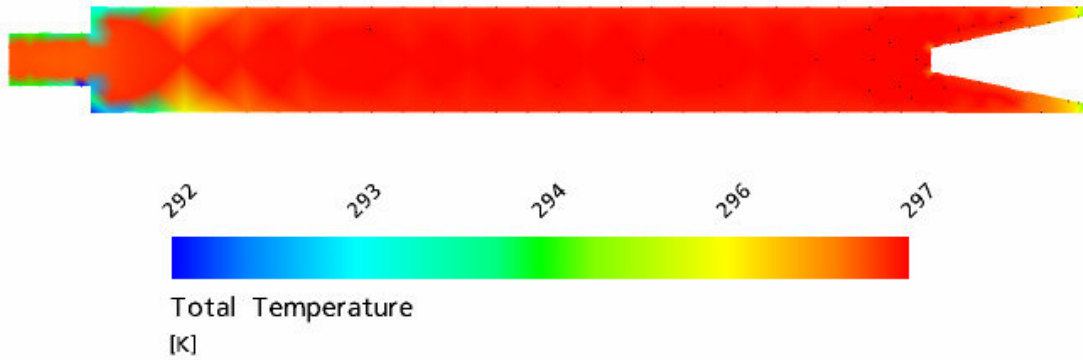


Fig. 4-13: Total temperature contour plot along the central axis of the RHVT, for Mesh No.1 containing 1,705 nodes, $\mu_c=0.4$, $P_{in}=2\text{Bar}$ and $L/D=10$, using the $k - \epsilon$ turbulence model.

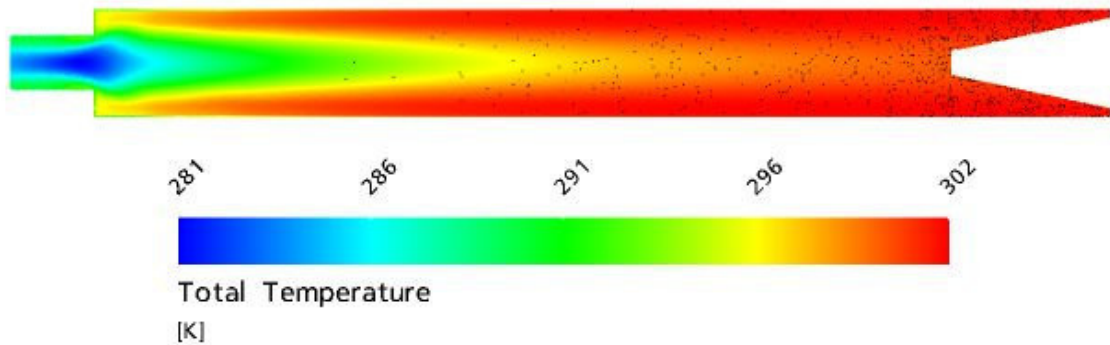


Fig. 4-14: Total temperature contour plot along the central axis of the RHVT, for Mesh No.5 containing 1,522,948 nodes, $\mu_c=0.4$, $P_{in}=2\text{Bar}$ and $L/D=10$, using the $k - \epsilon$ turbulence model.

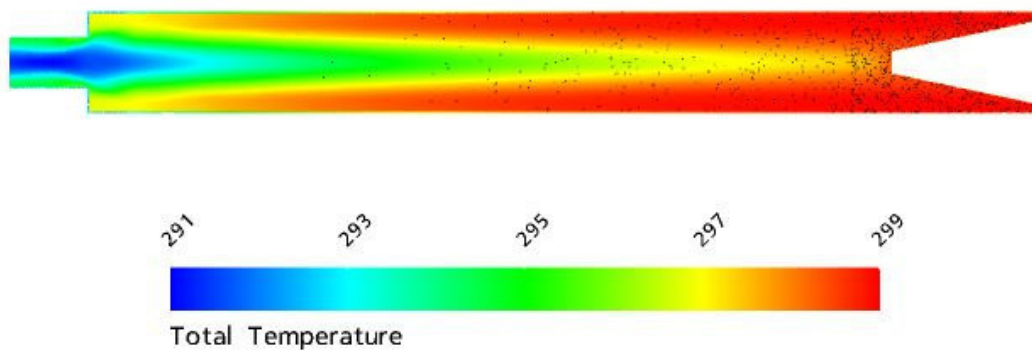


Fig. 4-15: Total temperature contour plot along the central axis of the RHVT, for Mesh No.5 containing 1,522,948 nodes, $\mu_c=0.4$, $P_{in}=2\text{Bar}$ and $L/D=10$, using the SST turbulence model.

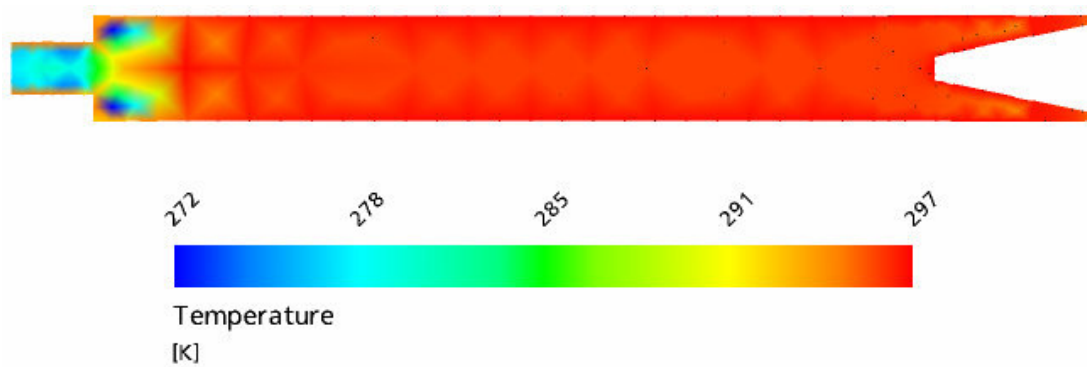


Fig. 4-16: Static temperature contour plot along the central axis of the RHVT, for Mesh No.1 containing 1,705 nodes, $\mu_c=0.4$, $P_{in}=2\text{Bar}$ and $L/D=10$, using the $k - \varepsilon$ turbulence model.

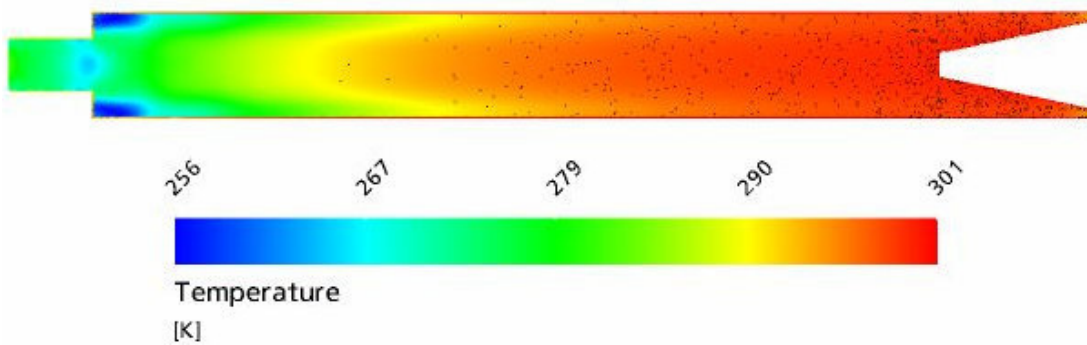


Fig. 4-17: Static temperature contour plot along the central axis of the RHVT, for Mesh No.5 containing 1,522,948 nodes, $\mu_c=0.4$, $P_{in}=2\text{Bar}$ and $L/D=10$, using the $k - \varepsilon$ turbulence model.

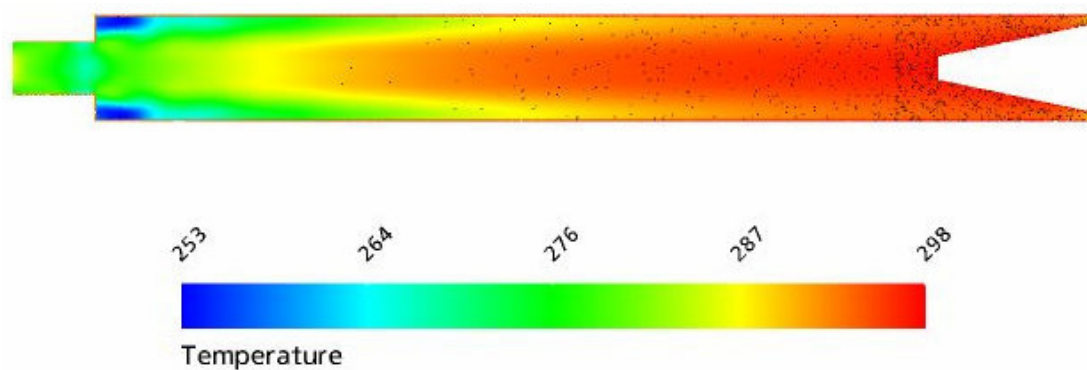


Fig. 4-18: Static temperature contour plot along the central axis of the RHVT, for Mesh No.5 containing 1,522,948 nodes, $\mu_c=0.4$, $P_{in}=2\text{Bar}$ and $L/D=10$, using the SST turbulence model.

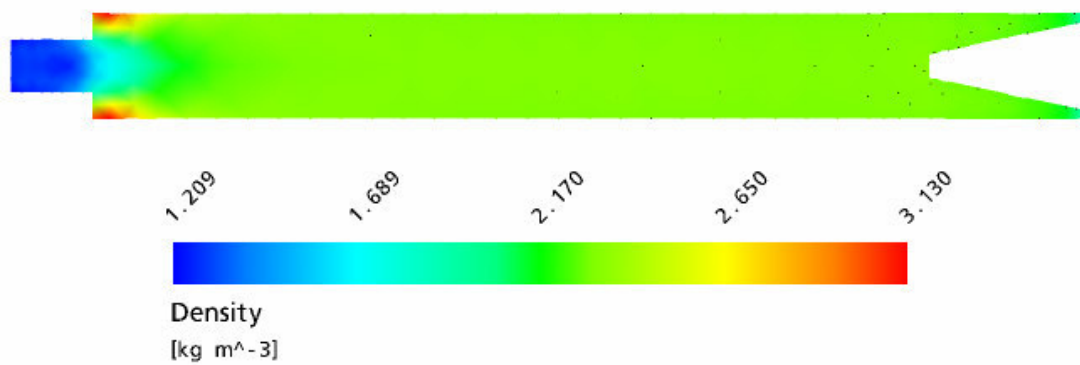


Fig. 4-19: Density contour plot along the central axis of the RHVT, for Mesh No.1 containing 1,705 nodes, $\mu_c=0.4$, $P_{in}=2\text{Bar}$ and $L/D=10$, using the $k - \varepsilon$ turbulence model.

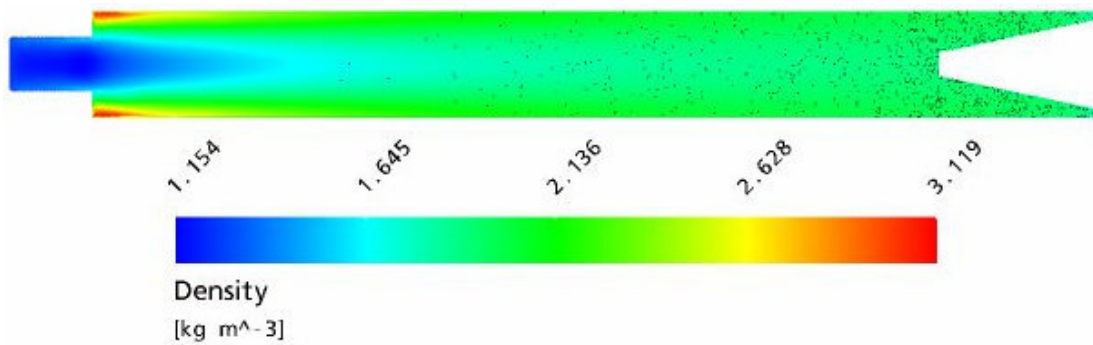


Fig. 4-20: Density contour plot along the central axis of the RHVT, for Mesh No.5 containing 1,522,948 nodes, $\mu_c=0.4$, $P_{in}=2\text{Bar}$ and $L/D=10$, using the $k - \varepsilon$ turbulence model.

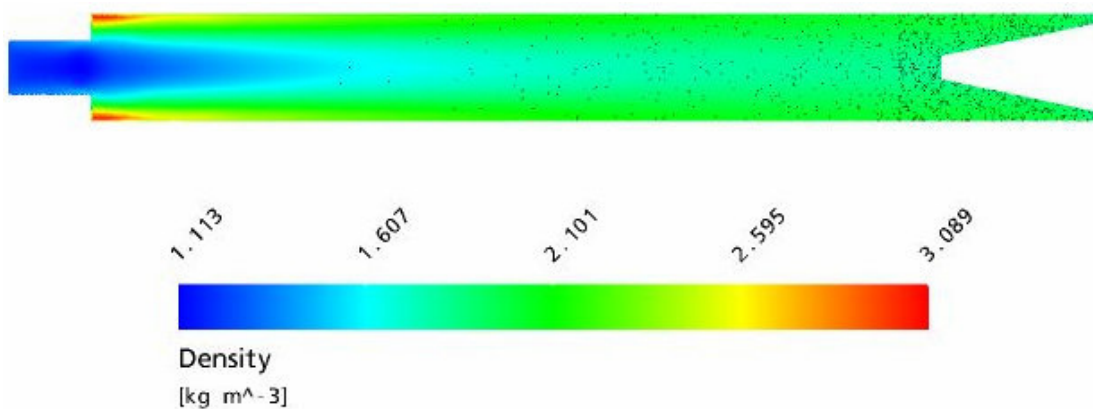


Fig. 4-21: Density contour plot along the central axis of the RHVT, for Mesh No.5 containing 1,522,948 nodes, $\mu_c=0.4$, $P_{in}=2\text{Bar}$ and $L/D=10$, using the SST turbulence model.

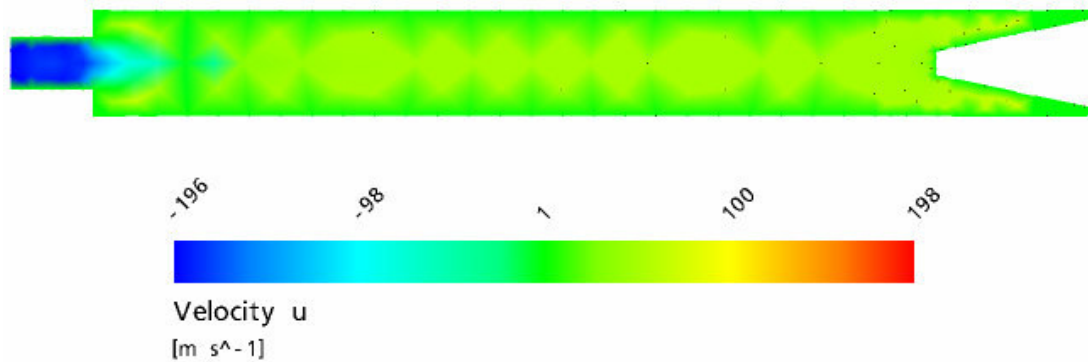


Fig. 4-22: Axial velocity contour plot along the central axis of the RHVT, for Mesh No.1 containing 1,705 nodes, $\mu_c=0.4$, $P_{in}=2\text{Bar}$ and $L/D=10$, using the $k - \varepsilon$ turbulence model.

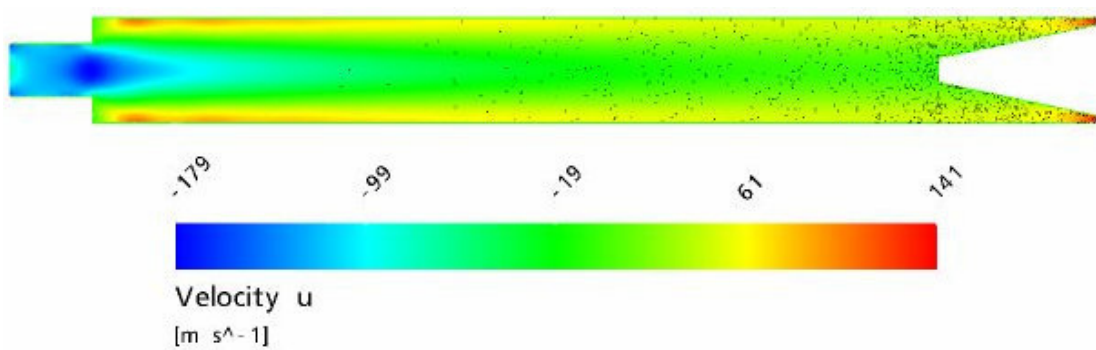


Fig. 4-23: Axial velocity contour plot along the central axis of the RHVT, for Mesh No.5 containing 1,522,948 nodes, $\mu_c=0.4$, $P_{in}=2\text{Bar}$ and $L/D=10$, using the $k - \varepsilon$ turbulence model.

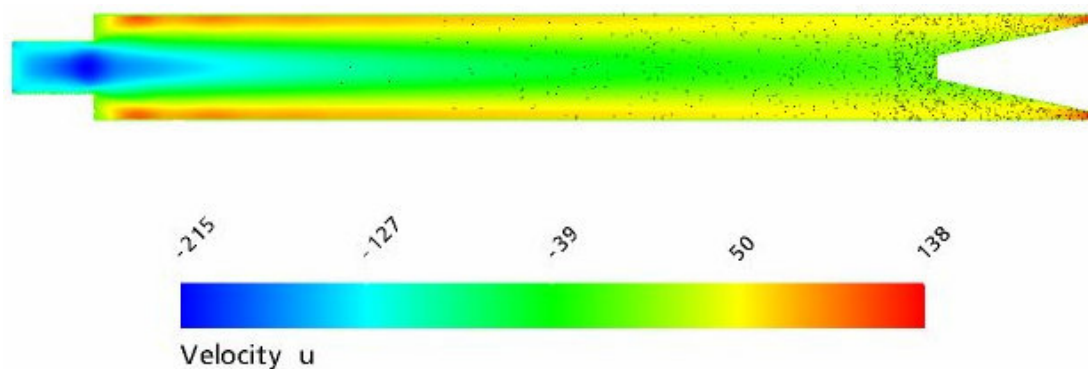


Fig. 4-24: Axial velocity contour plot along the central axis of the RHVT, for Mesh No.5 containing 1,522,948 nodes, $\mu_c=0.4$, $P_{in}=2\text{Bar}$ and $L/D=10$, using the SST turbulence model.

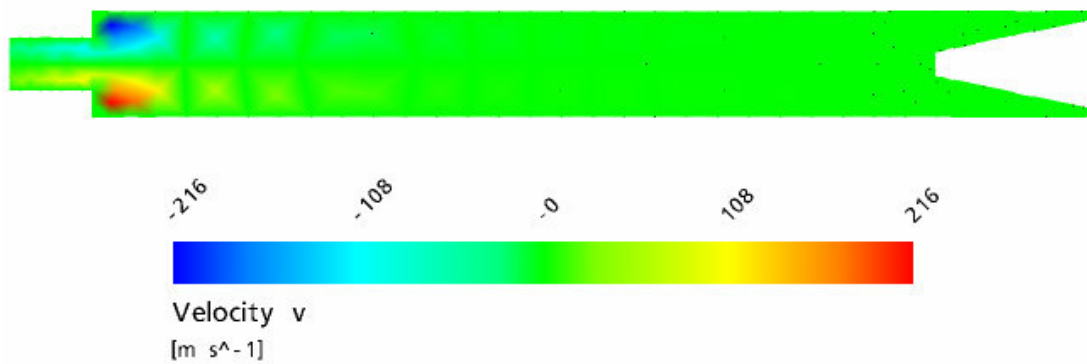


Fig. 4-25: Tangential velocity contour plot along the central axis of the RHVT, for Mesh No.1 containing 1,705 nodes, $\mu_c=0.4$, $P_{in}=2\text{Bar}$ and $L/D=10$, using the $k - \varepsilon$ turbulence model.

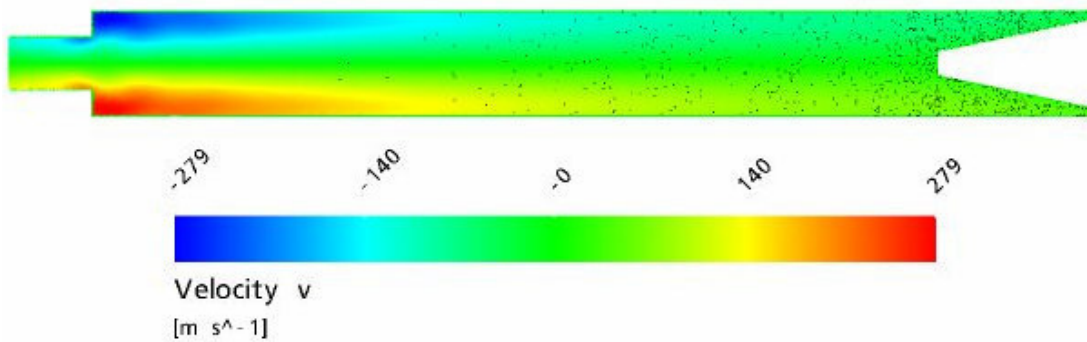


Fig. 4-26: Tangential velocity contour plot along the central axis of the RHVT, for Mesh No.5 containing 1,522,948 nodes, $\mu_c=0.4$, $P_{in}=2\text{Bar}$ and $L/D=10$, using the $k - \varepsilon$ turbulence model.

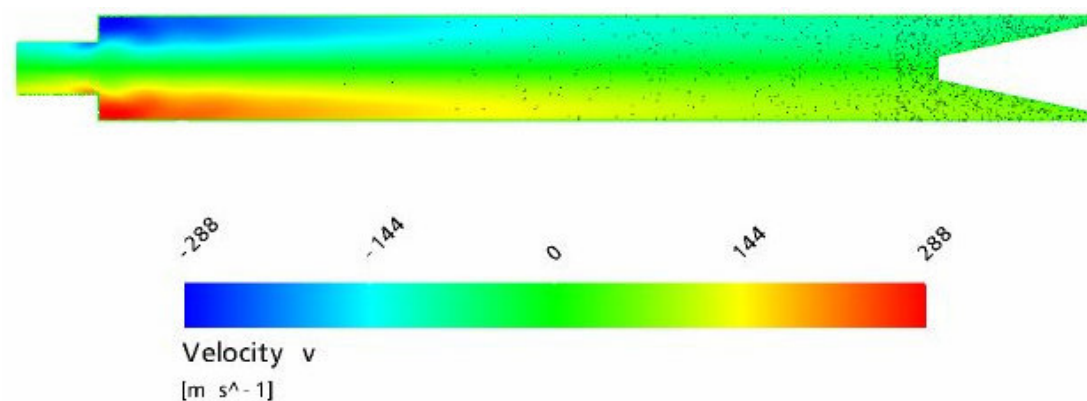


Fig. 4-27: Tangential velocity contour plot along the central axis of the RHVT, for Mesh No.5 containing 1,522,948 nodes, $\mu_c=0.4$, $P_{in}=2\text{Bar}$ and $L/D=10$, using the SST turbulence model.

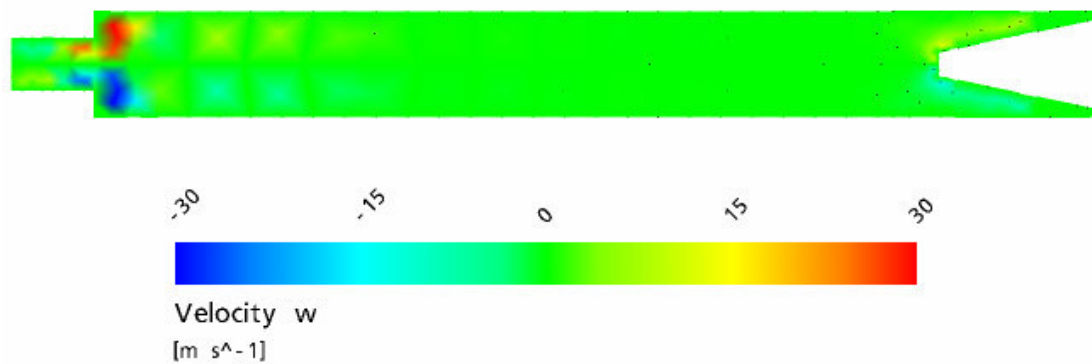


Fig. 4-28: Radial velocity contour plot along the central axis of the RHVT, for Mesh No.1 containing 1,705 nodes, $\mu_c=0.4$, $P_{in}=2\text{Bar}$ and $L/D=10$, using the $k - \varepsilon$ turbulence model.

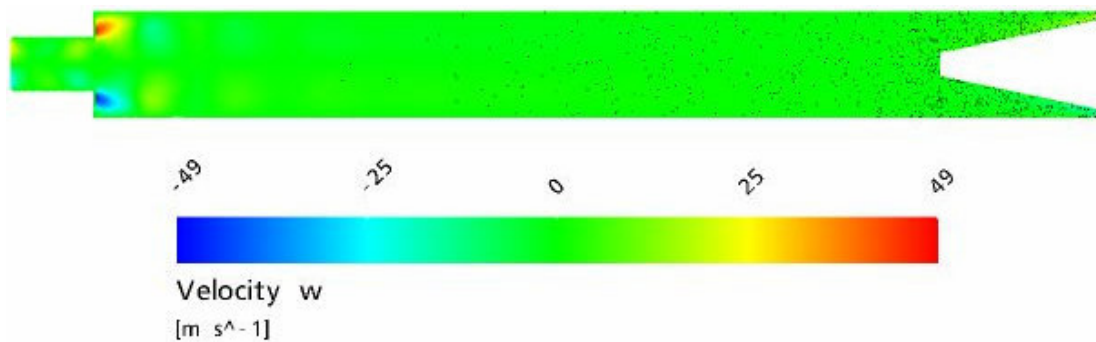


Fig. 4-29: Radial velocity contour plot along the central axis of the RHVT, for Mesh No.5 containing 1,522,948 nodes, $\mu_c=0.4$, $P_{in}=2\text{Bar}$ and $L/D=10$, using the $k - \varepsilon$ turbulence model.

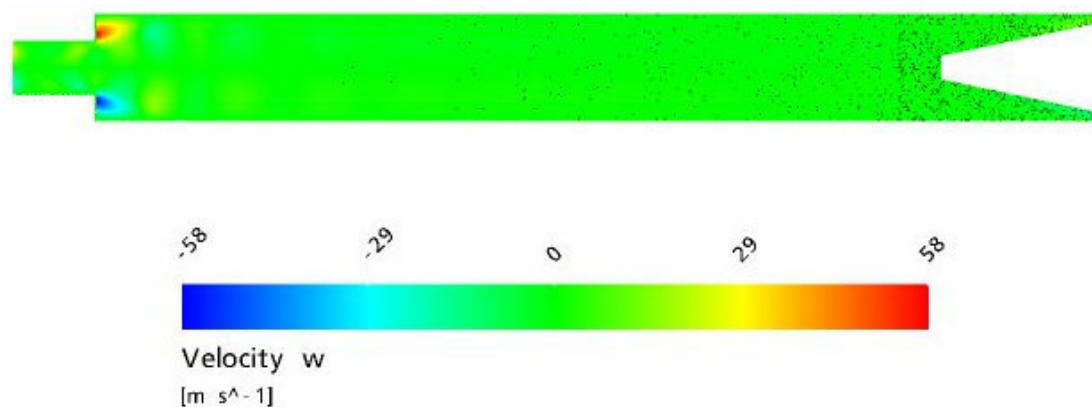


Fig. 4-30: Radial velocity contour plot along the central axis of the RHVT, for Mesh No.5 containing 1,522,948 nodes, $\mu_c=0.4$, $P_{in}=2\text{Bar}$ and $L/D=10$, using the SST turbulence model.

4.7.2 Reynolds Stress Model Performance

Such results as those in Fig. 4-12 to Fig. 4-30 were not possible using the Reynolds Stress turbulence model as it failed to converge to a final solution, even though it had been provided with a starting point of the results obtained from the $k - \varepsilon$ turbulence model. Proof of this can be seen in the residual convergence plot provided below, where it can be seen that this model is inherently unstable and crashed after only a few time-steps. Such a result is not unsurprising as this turbulence model contains several extra partial differential equations as detailed in Section A.3.6. Where these extra equations have an associated computation cost both in processing time and stability.

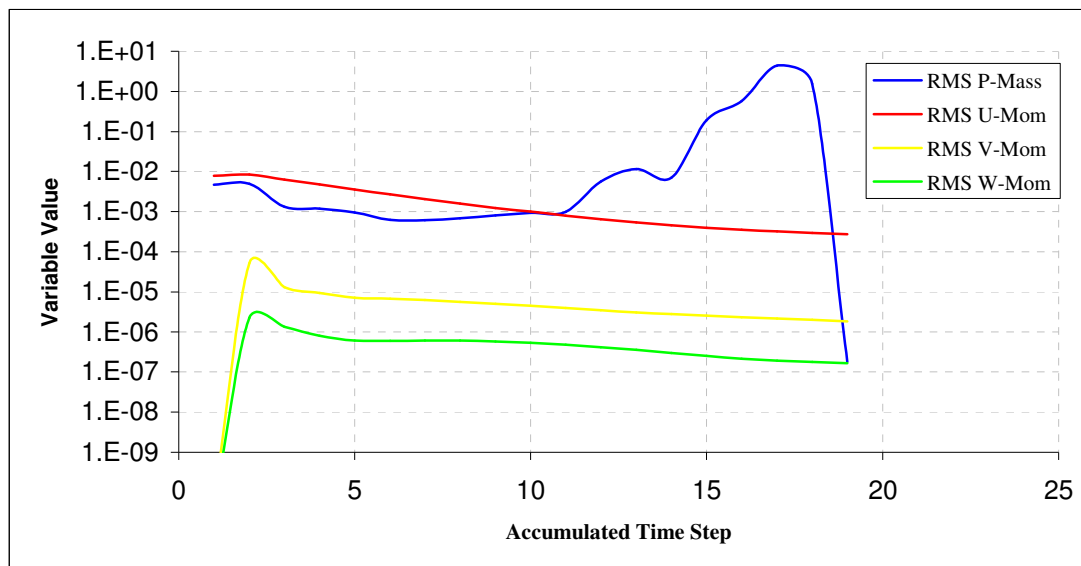


Fig. 4-31: Residual plot of mass and velocity components for the failed Reynolds Stress Model.

4.7.3 Flowfield Performance

Internal velocity profiles have been compared to the experimental results published by Gao et al. [7]. Although Gao et al used a different vortex tube configuration to that used by Promvong et al. and Soni, Gao et al's experimental results are non-dimensionalised and can therefore be compared to results from similar vortex tubes shown overleaf in Fig. 4-32 and Fig. 4-33. Similar plots to those of Fig. 4-32 and Fig. 4-33 cannot be recreated for different axial (x/L) locations, as already stated in Section 4.4, the RHVT CFD model developed for this analysis has been shortened considerably in comparison to experimental researchers such as Gao et al. [7], hence

rendering the entrance region the only comparable axial location for these velocity distributions. The comparison between measured and predicted normalised velocity distributions shown below and overleaf is very encouraging for both the $k - \varepsilon$ and SST turbulence models. However it can be easily seen that yet again the $k - \varepsilon$ turbulence model follows the utilised experimental results better than the SST turbulence model, as was also the case of the thermal analysis of Table 4-3. It is for this reason the $k - \varepsilon$ turbulence model is be utilised for all future studies of the RHVT within this work.

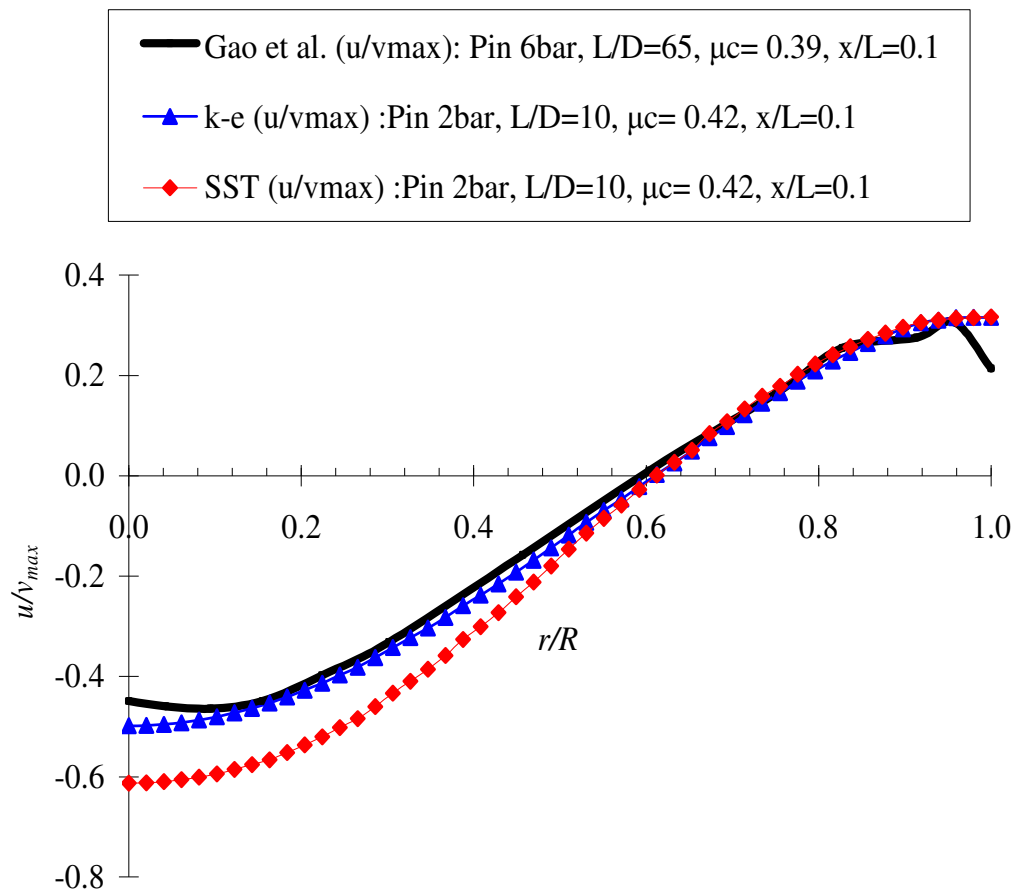


Fig. 4-32: Comparison of the computed variation of internal normalised axial velocity at normalised radial locations with experimental results from [7] at the inlet region within the RHVT, using both the $k - \varepsilon$ and SST turbulence models respectively.

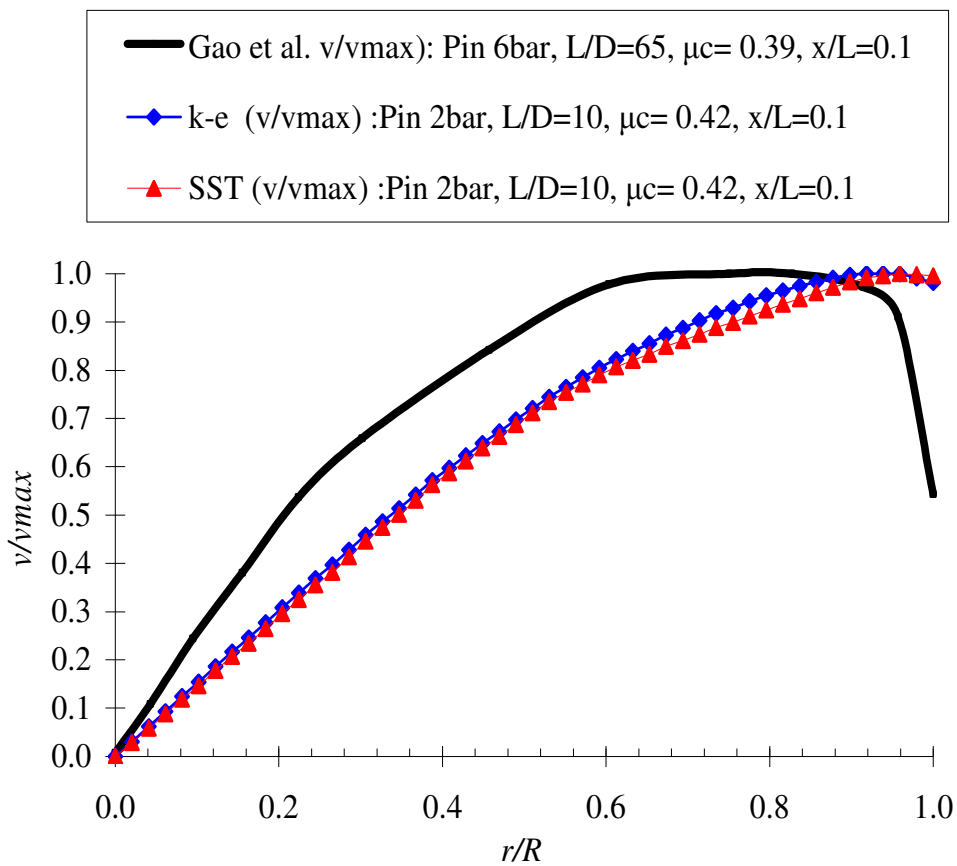


Fig. 4-33: Comparison of the computed variation of internal normalised tangential velocity at normalised radial locations with experimental results from [7] at the inlet region within the RHVT, using both the $k-\varepsilon$ and SST turbulence models respectively.

4.8 Summary

In this section a mesh independent solution was found for the computation RHVT model utilised. This preceded an investigation to find the optimum performing turbulence model for studying the flowfield characteristics of the RHVT. It was found that for the hardware available to the author that the $k-\varepsilon$ turbulence model gave the best results when compared to known experimental results, as already illustrated on a mesh of approximately 8.5 million elements. Once it was established that the $k-\varepsilon$ turbulence model was the optimum performing turbulence model this study of the RHVT moved on to an investigation into the mode of heat transfer within the RHVT. This is the subject of the next section of this work.

5 Investigation into the Mode of Heat Transfer

5.1 Introduction

Now that the known characteristics of the RHVT have been verified on a reliable computational mesh and turbulence model, can this study begin to investigate the mode of heat transfer within the RHVT. As already suggested this investigation will begin with a focus on the hypothesis that the function of secondary flow within the RHVT is to act as a conventional heat pump.

5.2 Secondary Flow

The first analysis of the numerical results of this CFD study of the RHVT is to quantify the influence of secondary flow within the tube. Namely, whether or not its function is to operate analogous to a refrigeration cycle as suggested by Ahlborn et. al. and illustrated earlier in Section 2.3.1. Before suggesting its influence, this secondary flow had to be captured, and it can be seen that a region of recirculating secondary flow is present within the RHVT, as can be seen in Fig. 5-1 and Fig. 5-2 for the boundary conditions stipulated earlier along with a stagnation point location as also shown in Fig. 5-1.

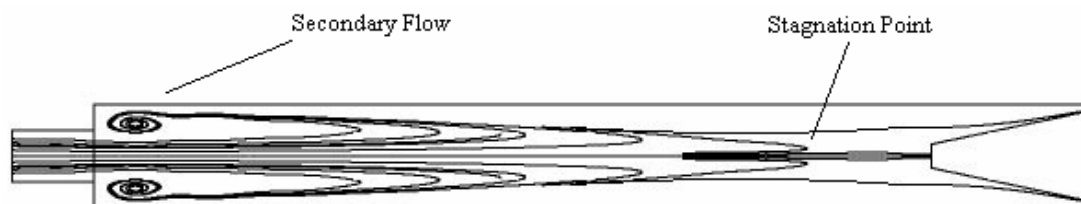


Fig. 5-1: Predicted streamline plot along the central axis show a successfully captured secondary flow within the RHVT, for $\mu_c=0.4$, $P_{in}=2\text{Bar}$ and $L/D=10$.

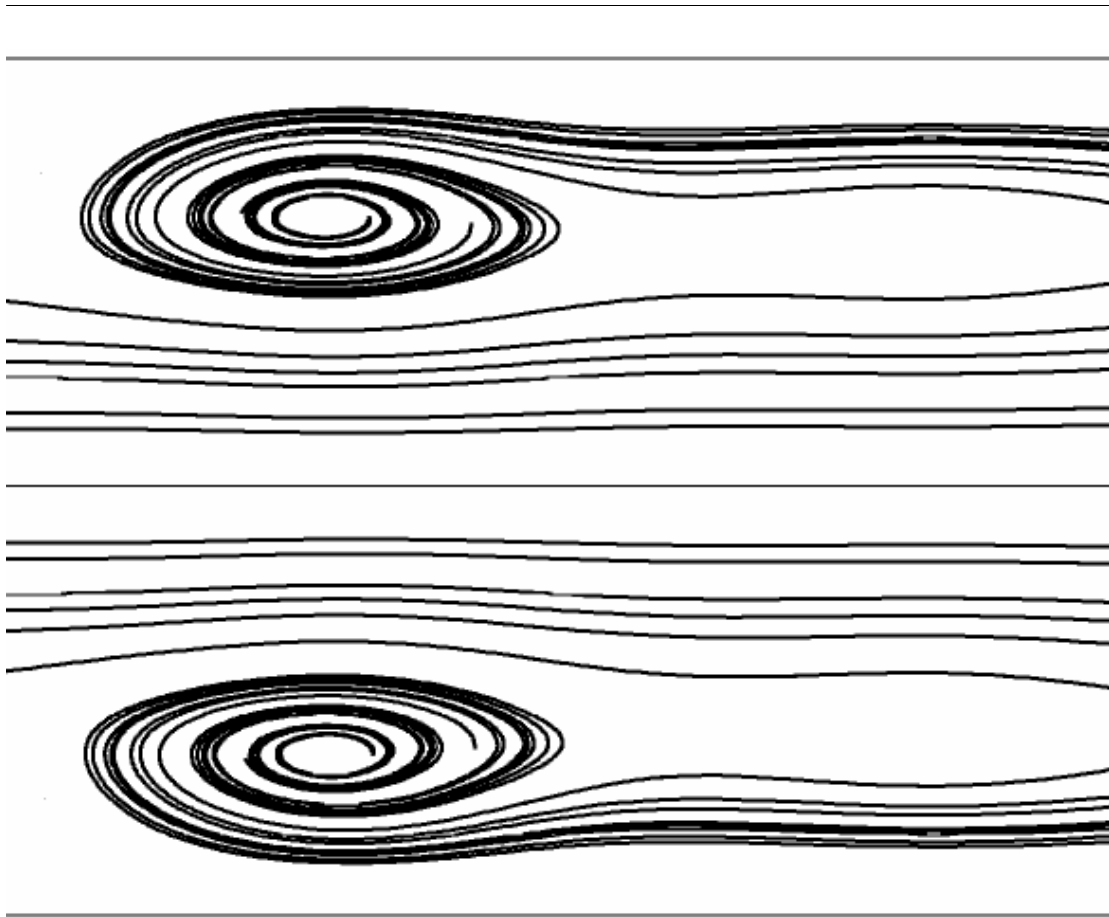


Fig. 5-2: Zoomed in view of the secondary flow within the RHVT, for $\mu_c=0.4$, $P_{in}=2\text{Bar}$ and $L/D=10$.

5.2.1 Relationship to Temperature Output

Following the successful capture of secondary flow, its relationship to temperature output was established by encouraging smaller and larger regions of recirculation by varying the ratio of cold diameter to vortex tube diameter, i.e. d_c/D . The captured secondary flows at the entrance region are shown below in Fig. 5-3.

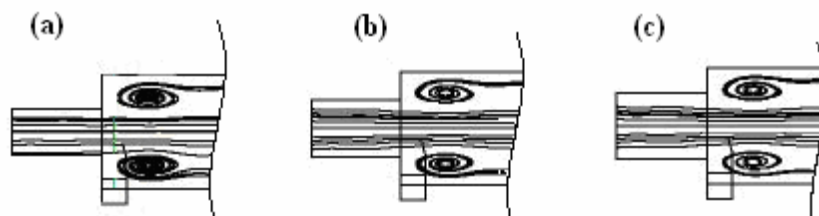


Fig. 5-3: Secondary flow captured at the entrance region of similar vortex tubes and the same original boundary conditions of Section 6.3 for (a) $d_c/D=0.4$, (b) $d_c/D=0.5$ and (c) $d_c/D=0.6$.

Restricting the flow out of the cold outlet has led to stronger recirculation for the narrow outlet in case (a) as can be seen in Fig. 5-3 above. This restriction of flow out of the cold outlet also leads to colder total temperature outputs in comparison to a

higher temperature outputs for the widening of the cold outlet, as recorded in the table below.

d_c/D	$T_{s,c} - T_{s,in}$ (K)	$T_{o,c} - T_{o,in}$ (K)
0.4	-3.5	-10.0
0.5	-5.6	-8.4
0.6	-5.6	-7.8

Table 5-1: Thermal output of a RHVT subject to values of $P_{in}=2\text{Bar}$, $L/D=10$, using (a) $d_c/D=0.4$, (b) $d_c/D=0.5$ and (c) $d_c/D=0.6$ respectively.

Such results were expected, as by restricting and expanding the cold outlet has resulted in smaller and larger cold fractions (μ_c) respectively, leading to similar temperature distribution predicted by the experimental results shown in Fig.1.7. Contour plots of these results are given below in Fig. 5-4, Fig. 5-5 and Fig. 5-6.

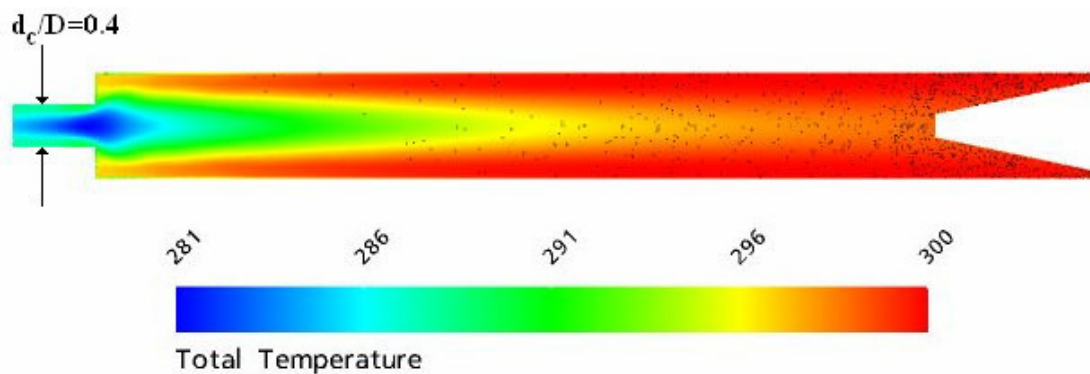


Fig. 5-4: Total temperature contour plot along the central axis of the RHVT, for $d_c/D=0.4$, $\mu_c=0.38$, $P_{in}=2\text{Bar}$ and $L/D=10$.

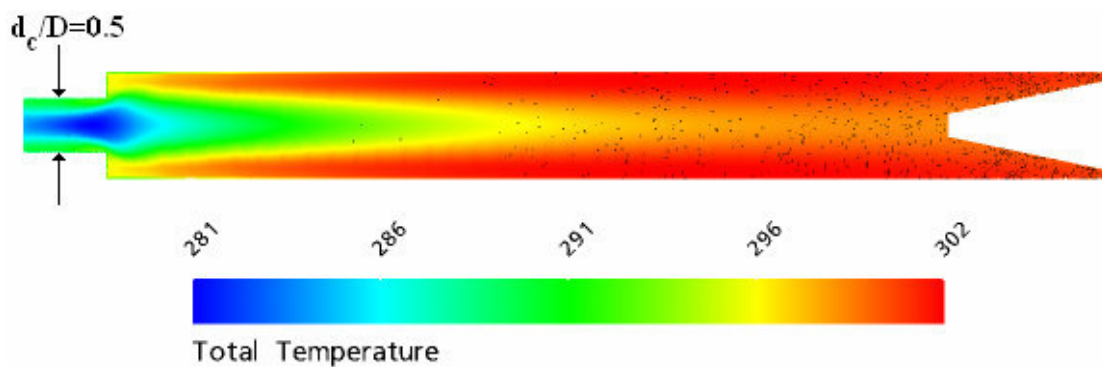


Fig. 5-5: Total temperature contour plot along the central axis of the RHVT, for $d_c/D=0.5$, $\mu_c=0.38$, $P_{in}=2\text{Bar}$ and $L/D=10$.

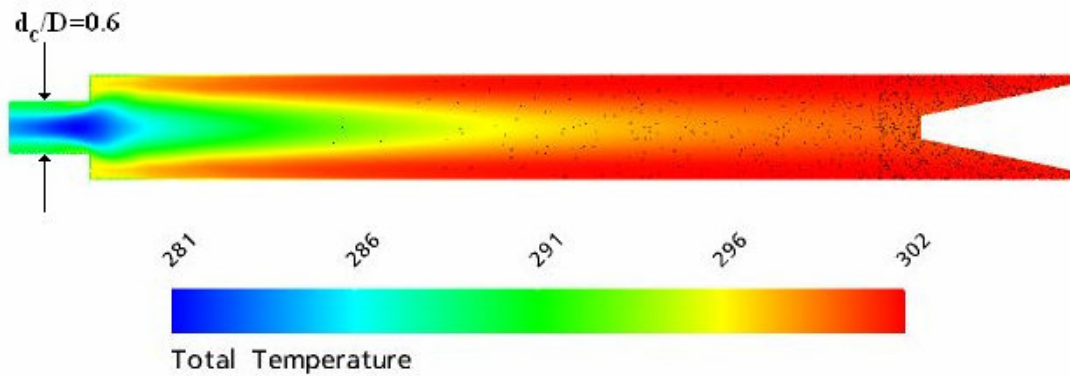


Fig. 5-6: Total temperature contour plot along the central axis of the RHVT, for $d_c/D=0.6$, $\mu_c=0.42$, $P_{in}=2\text{Bar}$ and $L/D=10$.

5.2.2 Thermodynamic Influence of Secondary Flow

The thermodynamic influence of secondary flow has been investigated in the figure below, in which the secondary flow streamlines have been superimposed onto a contour plot of the variance of density within the RHVT.

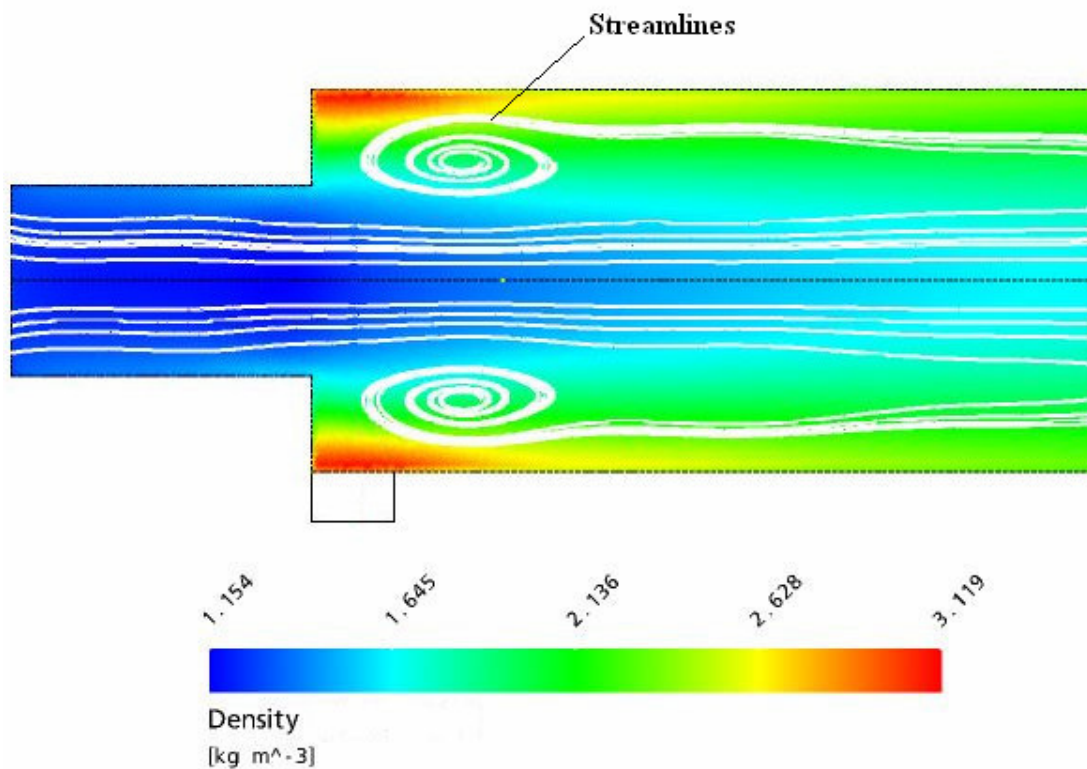


Fig. 5-7: Density contour plot along the central axis at the entrance region of the RHVT, for $\mu_c=0.4$, $P_{in}=2\text{Bar}$, $L/D=10$ and $d_c/D=0.5$, with streamlines of the secondary flow superimposed on the plot.

In the figure above it can be easily observed that there is no evidence of expansion or contraction of the fluid flow in the vicinity of the recirculatory region. Such variance of density (or pressure and temperature) in this region is paramount to support the

theory of secondary flow acting as a refrigeration loop. The reason being that for any compressible fluid, density variance is related to temperature according to the ideal gas law of Equation 3.6. i.e. $P = \rho RT_s$. As this is the case not only for density but also for the static temperature, total temperature and pressure contour plots shown below in Fig. 5-8, it can be now observed that there is no variation of these variables in tandem with secondary flow in the entrance region, sufficient to prove Ahlborn et al.'s refrigeration theory. As a direct result of this, this study will now move on to ascertain if there is any evidence of frictional heat transfer within the RHVT.

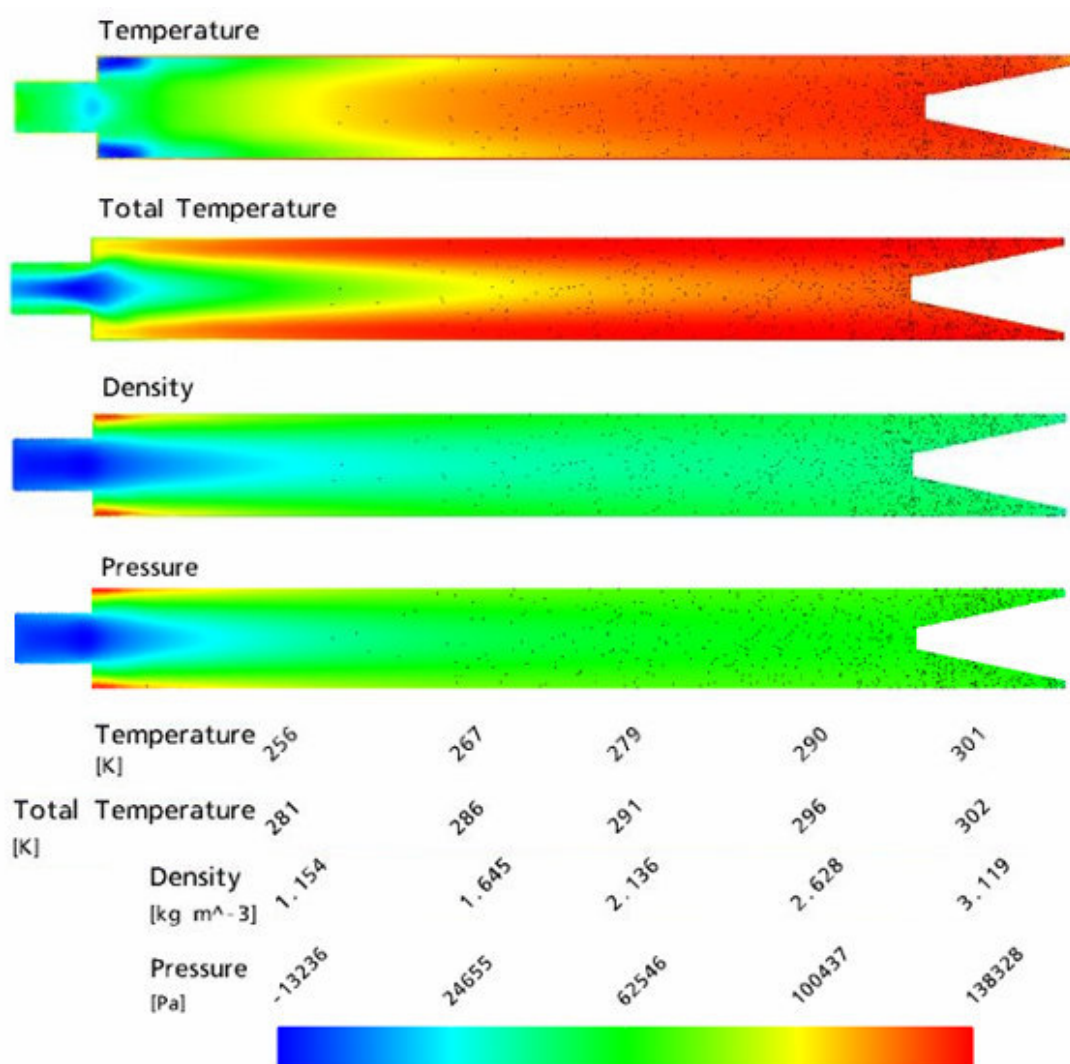


Fig. 5-8: Static temperature, total temperature, density and pressure contour plots along the central axis of the RHVT, for $\mu_c=0.4$, $P_{in}=2\text{Bar}$, $L/D=10$ and $d_c/D=0.5$.

5.3 Rotary Work due to Friction

As previously discussed in Section 2.4, the main component of work due to friction of fluid layers impinging on each other occurs in the $r - \theta$ plane. This was expressed as the rate of flow of work per unit area of the surface i.e.

$$\dot{W}_{ij} = \tau_{ij} \mathbf{U} \quad (5.1)$$

where for this case the relevant stress:

$$\tau_{r\theta} = \mu \left(\frac{\partial v}{\partial r} - \frac{v}{r} \right) \quad (5.2)$$

Therefore, the rotational work per unit area can be written as:

$$\dot{W}_{r\theta} = \mu \left(\frac{\partial v}{\partial r} - \frac{v}{r} \right) (u + v + w) \quad (5.3)$$

A user defined function of this rotational stress and work per unit area (due to friction) has been developed by the author within the post – processing package of ANSYS CFX 10, where this has enabled the development of contour plots of these variables across planes within the RHVT. The results of which are shown overleaf where the rotational stress and work per unit area across the central axis of the RHVT are presented in Fig. 5-9 and Fig. 5-10.

From Fig. 5-10, shown overleaf, it can be seen that there is distinct evidence of a flux of rotary work at the inlet region of the RHVT which suggests evidence to support the long held theory that the source of heat migration is due to friction. Furthermore this region of rotary work is only visible where there is a reversal in flow towards the cold outlet, supporting the theory that the length of the vortex tube should only be long enough to encompass the stagnation point as suggested earlier in Section 1.5.2.

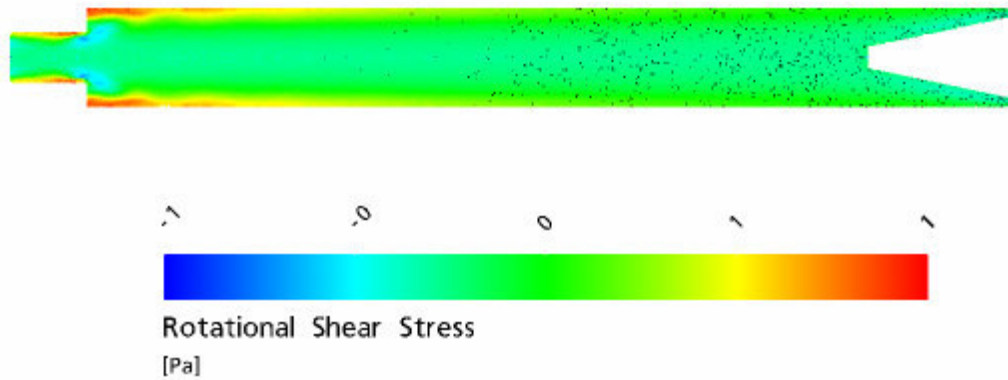


Fig. 5-9: Rotational shear stress along the central axis of the RHVT for $\mu_c=0.4$, $P_{in}=2\text{Bar}$, $L/D=10$ and $d_c/D=0.5$.

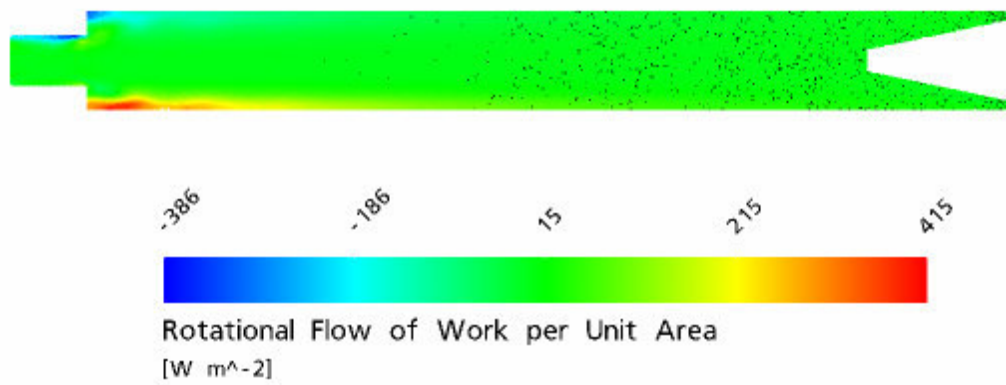


Fig. 5-10: Rotational flow of work per unit area along the central axis of the RHVT for $\mu_c=0.4$, $P_{in}=2\text{Bar}$, $L/D=10$ and $d_c/D=0.5$.

6 Conclusions

This computational study of the RHVT has shown that CFD techniques are well suited to analysing the highly complex flows contained within the RHVT. The computed flow fields compare favourably to previous experimental results and have shown that the utilised ANSYS CFX 10 software is capable of calculating the following:

- A comparable cold outlet total temperature drop i.e. $\Delta T_{o,c} = T_{o,in} - T_{o,c}$.
- Confirmation of the presence of secondary flow.
- Confirmation of a location of a stagnation point in the flow.

In addition to solving for the above properties of the RHVT, the CFD model has proven extremely successful at capturing and proving previously known flow - field characteristics of the vortex tube such as:

- The tangential velocity distribution at the entrance region.
- The axial velocity profile at the entrance region.

Such is the successful nature of the calculated results of the flows within the vortex tube, the author has been able to draw a conclusion as to the mode of heat transfer driving the cold and hot total temperature compressed air flow out of the tube.

Additionally, it was shown conclusively that there can be no longer any confusion as to the nature of the temperature measured by experimental researchers, as in Section 4.7.1 it was proven that the total temperature of the compressed air obeyed the adiabatic mixing equation of Section 1.5.1 fundamental to the 1st Law of Thermodynamics.

It has been shown that although there is a secondary flow region within the RHVT, it has been suggested that its presence is superfluous to the source of the energy separation. Evidence of this has been shown in Fig. 5-7 where there exists no correlation between the secondary flow streamlines and that of the analogous heat pump forwarded by Ahlborn et al. [17]

What has been shown is that there is evidence of rotary work due to friction within the RHVT. Such an outcome leads the author to support this long established

frictional heat transfer theory forwarded by the many authors, previously discussed in Section 2.4.

6.1 Recommendations for Future Work

It can be also concluded that the state-of-the-art CFD package when used along with the $k-\varepsilon$ turbulence model is well suited to further studies of the RHVT. Currently the only limitation of this technology is the required RAM to operate the CFD model of the RHVT successfully. However as hardware capabilities of computers continue to improve, with the current emergence of 64-Bit processors, and the associated availability of larger capacity RAM chips, can a mesh convergence study similar to the study published herein be completed to a cold temperature output a close as possible to that of the experimental researchers. In addition to this the entire experimental RHVT may be modelled without the need to shorten the length of the RHVT CFD model, as quantified in Sections 1.5.2 and 4.4.

At such a time the author recommends that the rotary work due to friction present within the RHVT should be analysed further. The author also recommends that this variable be predefined in the physics pre-processor and be made subject to stringent convergence criteria in the solution stage of CFD analysis. Such a process would lead to sharper contour plots to those of Fig. 5-9 and Fig. 5-10, and hence a greater scope to make additional conclusions to support frictional heat transfer theory.

7 References

- [1] Fulton, C.D., Ranque's Tube, *Journal of the American Society of Refrigeration Engineering*, Vol. 5, 1950, pp. 473-479.
- [2] Stong, C. L., The "Hilsch" Vortex Tube, *The Amateur Scientist*, Heinemann Educational Books, Chapter IX, Section 4, 1962, pp. 514-519.
- [3] AiRTEX International Ltd., How Vortex Tubes Work, www.airtexinternational.com.
- [4] Ranque, G. L., Method and Apparatus for Obtaining from a Fluid under Pressure Two Currents of Fluids at Different Temperatures, *U.S. Patent No. 1952281*, 1934.
- [5] Exair, Vortex Tubes and Spot Cooling Products, www.exair.com.
- [6] Hilsch, R., The Use of the Expansion of Gases in a Centrifugal Field as a Cooling Process, *Review of Scientific Instruments*, Vol. 18, No. 2, 1947, pp. 108-113.
- [7] Gao, C. M., *Experimental Study on the Ranque – Hilsch Vortex Tube*, Technische Universiteit Eindhoven, 2005.
- [8] Eastop, T.D. and McConkey, A., Applied Thermodynamics for Engineering Technologists, *Prentice Hall*, 5th Edition, 1993.
- [9] Cockerill, T. T., Fluid Mechanics and Thermodynamics of a Ranque-Hilsch Vortex Tube, MSc, *University of Cambridge*, 1995.
- [10] Promvong, P. and Eiamsa-ard, S., Investigation of the Thermal Separation in a Vortex Tube Refrigerator, *Science Asia*, Vol. 31, 2005, pp. 215-223.
- [11] Soni, Y., A Parametric Study of the Ranque-Hilsch Tube, University of Idaho, 1973.
- [12] Aljuwayhel, N. F., Nellis, G. F., and Klein, S. A., Parametric and Internal Study of the Vortex Tube using a CFD Model, *International Journal of Refrigeration*, Vol.28, 2005, pp. 442-450.
- [13] ITW Air Management, Vortec Air Guns, www.vortec.com.
- [14] P.A. Hilton Ltd., Refrigeration, www.p-a-hilton.co.uk.
- [15] Ahlborn, B. K. and Groves, S., Secondary Flow in a Vortex Tube, *Fluid Dynamics Research*, Vol. 21, 1997, pp. 73-86.

-
- [16] Ahlborn, B. K. and Gordon, J.M., The Vortex Tube as a Classic Thermodynamic Refrigeration Cycle, *Journal of Applied Physics*, Vol. 88, No. 6, 2000, pp. 3645-3653.
- [17] Ahlborn, B. K., Keller, J. U. and Rebhan, E., The Heat Pump in a Vortex Tube, *Journal of Non – Equilibrium Thermodynamics*, Vol. 23, 1998, pp. 159-165.
- [18] Gao, C. M., Bosschaart, K. J., Zeegers, J. C. H., and de Waele, A.T.A.M., Experimental Study on a Simple RHVT, *Cryogenics*, Vol. 45, 2005, pp. 173-183.
- [19] Bruun, H. H., Experimental Investigation of the Energy Separation in Vortex Tubes, *Journal Mechanical Engineering Science*, Vol. 11, No. 6, 1969, pp. 567-582.
- [20] Lewins, J. and Bejan, A., Vortex Tube Optimization Theory, *Energy*, Vol. 24, 1999, pp. 931-943.
- [21] Fröhlingsdorf, W. and Unger, H., Numerical Investigations of the Compressible Flow and the Energy Separation in the Ranque – Hilsch Vortex Tube, *International Journal of Heat and Mass Transfer*, Vol. 42, 1999, pp. 415-422.
- [22] Deissler, R.G. and Perlmutter, M., Analysis of the Flow and Energy Separation in a Vortex Tube, *International Journal of Heat and Mass Transfer*, Vol. 1, 1960, pp. 173-181.
- [23] Young, J. and Mc Cutcheon, A.R.S., The Performance of Ranque–Hilsch Vortex Tube, *The Chemical Engineer*, November, pp. 522–528.
- [24] Kurosaka, M., Acoustic Streaming in Swirling Flow and the Ranque – Hilsch Vortex Tube Effect, *Journal of Fluid Mechanics*, 1982, pp. 124-139.
- [25] McDuffie, N. G., Resonance in a Ranque – Hilsch Vortex Tube, *18th Joint National Heat Transfer Conference, American Society of Mechanical Engineers Publication No. 79-HT-16*, 1979.
- [26] Hartnett, J. P. and Eckert, E. R. G., Experimental Study of the Velocity and Temperature Distribution in a High – Velocity Vortex Type Flow, *Journal of Heat Transfer*, 1957, pp. 751-758.
- [27] Stephan, K., Lin, S., Durst, M., Huang, F. and Seher, D., An Investigation of Energy Separation in a Vortex Tube, *International Journal of Heat and Mass Transfer*, Vol. 26, No. 3, 1983, pp. 341-348.
- [28] Camiré, J., Experimental Investigation of Vortex Tube Concepts, *Université Laval*, 1995.

-
- [29] Behera, U., and Paul, P. J., CFD Analysis and Experimental Investigations towards Optimizing the Parameters of RHVT, *International Journal of Heat and Mass Transfer*, Vol.48, 2005, pp. 1961-1973.
- [30] Skye, H. M., Nellis, G. F., and Klein, S. A., Comparison of CFD Analysis to Empirical Data in a Commercial Vortex Tube, *International Journal of Refrigeration*, Vol.29, 2006, pp. 71-80.
- [31] Colgate, S. A. and Buchler, J. R., Coherent Transport of Angular Momentum – The Ranque – Hilsch Tube as a Paradigm in Astrophysical Turbulence and Convection, *Annals of New York Academy Sciences*, Vol. 898, 2000, pp. 105-112.
- [32] Versteeg, H. K. and Malalasekera, W., An Introduction to Computational Fluid Dynamics, The Finite Volume Method; *Longman Scientific & Technical*, 1st Edition, 1995.
- [33] ANSYS CFX 10 – Solver, Release 10.0: Theory, *ANSYS CFX 10.0 Support Documentation*, ANSYS Inc., 2005.
- [34] Anderson, J.D., Computational Fluid Dynamics: The Basics with Applications, *McGraw – Hill*, 1995.
- [35] ANSYS CFX 10, Release 10.0: Installation and Overview, *ANSYS CFX 10.0 Support Documentation*, ANSYS Inc., 2005.
- [36] Saidi, M. H. and Valipour, M. S., Experimental Modelling of a Vortex Tube Refrigerator, *Applied Thermal Engineering*, Vol. 23, 2003, pp. 1971-1980.
- [37] Hoffmann, K. A., Fundamental Equations of Fluid Mechanics, *Engineering Education System*, 1996.

A Turbulence and Turbulence Modelling

A.1 Introduction

As part of the studies in completing the numerical analysis of the RHVT additional coursework essential to the understanding of the basics of CFD was conducted. These studies began with a report on turbulence and turbulence modelling as follows, which formed an additional submission (to this thesis) to the Department of Mechanical Engineering, D.I.T. Bolton St.

A.2 Turbulence

The analysis of any fluid flow domain is generally classified by two different fluid flow regimes that have been termed laminar and turbulent flow.



Fig. A-1: Laminar and Turbulent Flows of Water from a tap.

The classic illustration to describe the common occurrence of laminar flow and the onset to turbulence is by looking at water flowing out of a tap as shown in Fig. A-1. As the flow rate of water is gradually increased the flow will eventually lead to a turbulent structure as in the picture above. In a laminar flows particles of fluid move smoothly along well – defined, relatively simple paths, or in layers without mixing. Turbulent flows on the other hand have pronounced random, chaotic characteristics with much particle mixing, and are best defined in terms of their statistical properties such as averages and deviations from that average. Generally, it can be expected that very slow flows are laminar and the viscous stresses produced, play a very important retarding part in governing the flow. As the speed of the flow is increased most flows become unstable and change to a turbulent nature, where inertial forces play a

significant role in displacing this fluid. When the motion of a fluid particle is disturbed, its inertia will tend to carry it on in the new direction, but the viscous forces due to the surrounding fluid will tend to make it conform to the motion of the rest of the stream. In a laminar flow the viscous shear stresses are sufficient to eliminate the effect of these deviations; however in turbulent flow they are inadequate. The criterion which determines whether flow will be laminar or turbulent is therefore the ratio of the inertial force to the viscous force acting on the particle, this ratio is known as the Reynolds number, and is given as:

$$\text{Re} = \frac{\text{Inertial Force}}{\text{Viscous Force}} = \frac{\rho UL}{\mu} \quad (\text{A.1})$$

where for this case L is the length of the region of interest respectively. Experimentation can yield values of Reynolds number at which transition to turbulence occurs. Turbulent flows occur more frequently in nature and in many instances a turbulent flow is preferable to a laminar flow as particles of fluid which are initially separated by a long distance can be brought closer together by the eddying motions in turbulent flows as can be seen for example in Fig. A-2 below. As a consequence, heat, mass and momentum are very effectively exchanged.

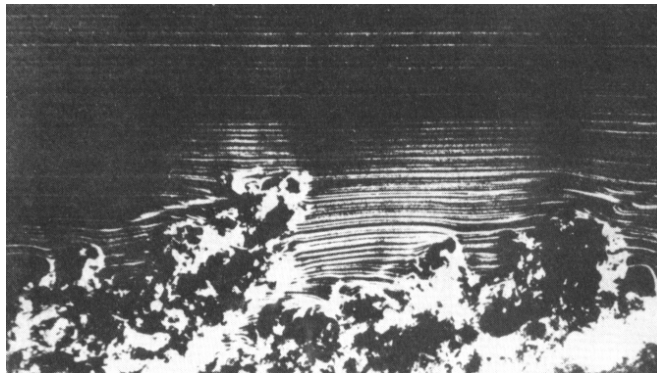


Fig. A-2: Magnified view of a Turbulent Boundary Layer [32]

The random nature of a turbulent flow renders computations based on a complete description of the motion of all the fluid particles impossible. Instead the velocity and other properties of the fluid are decomposed into a steady mean value with a fluctuating component superimposed on it, as for example in the simple illustration in Fig. A-3 overleaf.

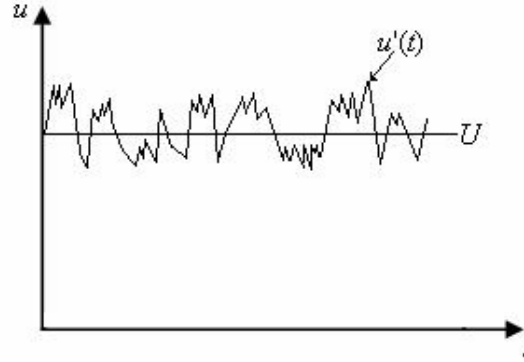


Fig. A-3: Mean velocity U and fluctuating velocity u' of the total velocity u .

Such an analysis of a fluid flow property as this has led to a means of studying the influence of turbulence on the mean flow properties of the flow, where the mean Φ , of a flow property φ , can be defined as follows:

$$\Phi = \frac{1}{\Delta t} \int_0^{\Delta t} \varphi(t) dt \quad (\text{A.2})$$

Flow properties are time dependent and can be thought of as the sum of a steady mean component and a time varying fluctuating component with zero mean value as follows

$$\varphi(t) = \Phi + \varphi'(t) \text{ and } \int_0^{\Delta t} \varphi'(t) dt = 0 \quad (\text{A.3})$$

To illustrate the influence of turbulence fluctuations on mean flow properties of fluid flow, the components of velocity and pressure in the Cartesian form of the compressible Navier – Stokes equations, (3.1) – (3.5), are replaced with the sum of a mean and fluctuating component e.g. u is replaced with $U + u'$ etc. the result of which is given by the Reynolds Averaged Navier – Stokes (RANS) equations below:

$$\frac{\partial \rho}{\partial t} + \text{div}(\rho \mathbf{U}) = 0 \quad (\text{A.4})$$

$$\frac{\partial \rho U}{\partial t} + \text{div}(\rho U \mathbf{U}) = -\frac{\partial P}{\partial x} + \text{div}(\mu \text{ grad } U) + \left[-\frac{\partial(\overline{\rho u'^2})}{\partial x} - \frac{\partial(\overline{\rho u'v'})}{\partial y} - \frac{\partial(\overline{\rho u'w'})}{\partial z} \right] \quad (\text{A.5})$$

$$\frac{\partial \rho V}{\partial t} + \text{div}(\rho V \mathbf{U}) = -\frac{\partial P}{\partial y} + \text{div}(\mu \text{ grad } V) + \left[-\frac{\partial(\overline{\rho u'v'})}{\partial x} - \frac{\partial(\overline{\rho v'^2})}{\partial y} - \frac{\partial(\overline{\rho v'w'})}{\partial z} \right] \quad (\text{A.6})$$

$$\frac{\partial \rho W}{\partial t} + \text{div}(\rho W \mathbf{U}) = -\frac{\partial P}{\partial z} + \text{div}(\mu \text{grad } W) + \left[-\frac{\partial(\rho \overline{u'w'})}{\partial x} - \frac{\partial(\rho \overline{v'w'})}{\partial y} - \frac{\partial(\rho \overline{w'^2})}{\partial z} \right] \quad (\text{A.7})$$

$$\frac{\partial \rho h_o}{\partial t} - \frac{\partial P}{\partial t} + \text{div}(\rho h_o \mathbf{U}) = \text{div}(\lambda \text{grad } T_s) + \left[-\frac{\partial(\rho \overline{u'h'_s})}{\partial x} - \frac{\partial(\rho \overline{v'h'_s})}{\partial y} - \frac{\partial(\rho \overline{w'h'_s})}{\partial z} \right] \quad (\text{A.8})$$

Where u' , v' and w' are the fluctuating x , y and z components of the velocity vector \mathbf{U} respectively and h'_s is the fluctuating component of the static specific enthalpy, h_s . Also a scalar transport equation can be derived by an analogous formation of the RANS equations, note the pressure gradient term has been incorporated into the div diffusion term below

$$\frac{\partial \rho \Phi}{\partial t} + \text{div}(\rho \Phi \mathbf{U}) = \text{div}(\Gamma_\Phi \text{grad } \Phi) + \left[-\frac{\partial(\rho \overline{u'\phi'})}{\partial x} - \frac{\partial(\rho \overline{v'\phi'})}{\partial y} - \frac{\partial(\rho \overline{w'\phi'})}{\partial z} \right] \quad (\text{A.9})$$

By introducing time average components new additional terms that involve products of the fluctuating velocities, have been introduced. Their role is reflected as additional turbulent stresses to the pressure and viscous stresses acting upon the mean velocity components U , V and W , on the RHS of the RANS equations. To clarify these stresses they are as follows:

$$\tau_{xx}^R = -\rho \overline{u'^2}, \quad \tau_{yy}^R = -\rho \overline{v'^2}, \quad \tau_{zz}^R = -\rho \overline{w'^2}, \quad \tau_{xy}^R = \tau_{yx}^R = -\rho \overline{u'v'}, \quad \tau_{xz}^R = \tau_{zx}^R = -\rho \overline{u'w'}, \quad \text{and}$$

$$\tau_{yz}^R = \tau_{zy}^R = -\rho \overline{v'w'}.$$

Theses extra stresses are called the Reynolds stresses, this name is merely a pseudonym for the terms above as it is only dimensionally correct to call these terms, stresses.

A.3 Turbulence Modelling

As the original Navier – Stokes equations (3.1) – (3.4) (less the energy equation (3.5) which is not warranted for purpose of illustrating the concepts of turbulence modelling) plus the ideal gas law (3.6) form a closed mathematical system of equations i.e. an equal number of unknown variables as there is equations, these equations can be solved iteratively. However as a result of time – averaging of the equations (3.1) – (3.4), six additional unknowns have been formed and as in any system of simultaneous equations of independent variables, there must be an equal amount of equations as there are variables, in order to solve for each variable in turn.

This leads to the necessity of turbulence modelling which develops computational procedures of predicting the Reynolds stresses, in order to close the RANS equations to find a solution for all the variables. Some of the most popular turbulence models that will be summarised in turn are given below:

1. Prandtl's mixing model.
2. The $k - \varepsilon$ model.
3. The $k - \omega$ model.
4. The SST model by Menter.
5. Reynolds stress equation model.

A.3.1 Boussinesq Hypothesis

Many turbulence models are based upon the Boussinesq Hypothesis [32]. It was experimentally observed by Boussinesq that turbulence decays unless there is shear in isothermal incompressible flow and was also found to increase as the main rate of deformation increases. Based on this observation an analogy is drawn between the viscous stresses and the Reynolds stresses in the RANS equations. As the viscous stresses can be equated to gradients of the fluid velocity by Newtons Law of Viscosity as follows:

$$\tau_{ij} = \mu e_{ij} = \mu \left(\frac{\partial u_i}{\partial x_j} + \frac{\partial u_j}{\partial x_i} \right) \quad (\text{A.10})$$

in a similar fashion Reynolds stresses are linked to the mean rates of deformation in the relationship below.

$$\tau_{ij}^R = -\rho \overline{u'_i u'_j} = \mu_t E_{ij} = \mu_t \left(\frac{\partial U_i}{\partial x_j} + \frac{\partial U_j}{\partial x_i} \right) = \rho \nu_t \left(\frac{\partial U_i}{\partial x_j} + \frac{\partial U_j}{\partial x_i} \right) \quad (\text{A.11})$$

In the above formula a new proportionality variable μ_t , the turbulent viscosity, and its associated turbulent kinematic viscosity, ν_t , have been introduced. The turbulent viscosity is not a homogeneous term. It is however assumed to be isotropic in the formation of turbulence models based on Boussinesq hypothesis. This assumption is valid for many fluid flows, but not all, e.g. flows with strong separation or swirl. Due consideration of the rate of deformation is warranted here as it is given in tensor

notation e_{ij} above. This rate of decomposition of a fluid element in a turbulent flow can be decomposed into a mean and fluctuating component as follows

$$e_{ij} = E_{ij} + e'_{ij} \tag{A.12}$$

The components of which appear frequently in turbulent modelling theory.

A.3.2 Prandtl's Mixing Length Model

This model is based on the Boussinesq hypothesis, and use of this simple model is limited to academic fields, including here where formation of its theory helps to develop an understanding of more advanced models. The mixing length model attempts to describe the Reynolds stresses by means of simple algebraic formulae for μ_t as a function of position.

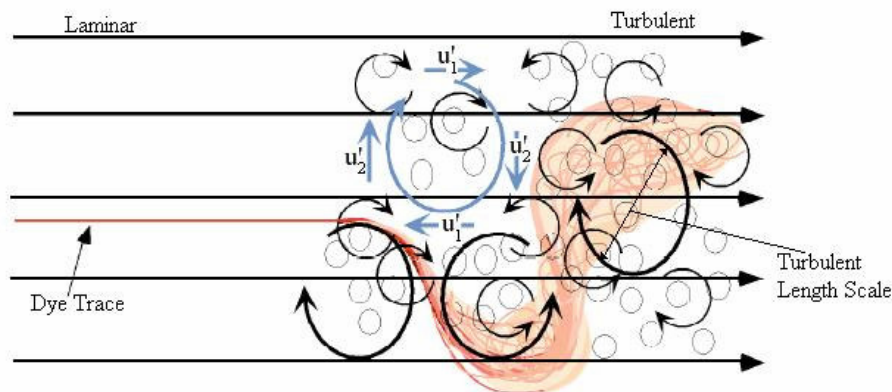


Fig. A-4: Dye trace injected into a parallel mean flow. In the developing turbulent flow eddies of many sizes are superimposed onto the mean flow. An example of the turbulent length scale has been highlighted.

The model assumes on dimensional grounds that the turbulent kinematic viscosity ν_t , which has dimensions m^2/s , is proportional to a product of a turbulent velocity scale ϑ (m/s) and a length scale ℓ (m) as illustrated in Fig. A-4, sufficing to describe the effects of turbulence as follows

$$\nu_t = C\vartheta\ell \tag{A.13}$$

C is a dimensionless constant to equate the proportional quantities above.

It is correct to say that most of the kinetic energy of turbulence is contained in the largest eddies within the turbulent flow, and therefore the turbulence length scale illustrated above is characteristic of these eddies which interact with the mean flow. The mixing length model is used in simple two dimensional flow calculations, where

it can be argued that the only significant Reynolds stress is $\tau_{xy}^R = \tau_{yx}^R = -\rho \overline{u'v'}$ with the only significant mean velocity gradient being $\partial U / \partial y$. For such a flow regime it is therefore dimensionally correct to state that, if the eddy length scale is ℓ , the turbulent velocity scale ϑ , can be stated as:

$$\vartheta = c\ell \left| \frac{\partial U}{\partial y} \right| \quad (\text{A.14})$$

with c a dimensional constant. The absolute value is to ensure that the velocity scale is always a positive quantity irrespective of the sign of the velocity gradient. Combination of equations (A.13), (A.14), and absorption of constants which appear in the two formulae into a new length scale, an adjustable mixing length ℓ_m , we obtain Prandtl's mixing length model

$$\nu_t = \ell_m^2 \left| \frac{\partial U}{\partial y} \right| \quad (\text{A.15})$$

Noting that in this mixing length model the only significant mean velocity gradient is $\partial U / \partial y$, hence the Reynolds stress τ_{xy} can be described in the following manner

$$\begin{aligned} \tau_{xy}^R &= -\rho \overline{u'_i u'_j} = \rho \nu_t \left(\frac{\partial U}{\partial y} + \frac{\partial V}{\partial x} \right) \\ \tau_{xy}^R &= \rho \nu_t \left(\frac{\partial U}{\partial y} \right) = \rho \ell_m^2 \left| \frac{\partial U}{\partial y} \right| \frac{\partial U}{\partial y} \end{aligned} \quad (\text{A.16})$$

If, in the flow regime of interest, the convection and diffusion of turbulence properties can be neglected, it is possible to express the influence of turbulence on the mean flow in terms of the mixing length. When using this model the effects of turbulence changes can be accounted for by varying the adjustable mixing length ℓ_m . The advantages and disadvantages of this turbulence model are given below in Table A-1 from [32].

Advantages	Disadvantages
<ul style="list-style-type: none"> • Easy to implement and cheap in terms of computing resources. • Good predictions for shear layers: mixing layers, and boundary layers. 	<ul style="list-style-type: none"> • Completely incapable of describing flows with separation and recirculation. • Only calculates mean flow properties and turbulent shear stresses.

Table A-1: Advantages and disadvantages of Prandtl's Mixing Length Model [32].

A.3.3 The $k - \varepsilon$ Model

If convection and diffusion are not negligible, as is the case for example in recirculating flows, a compact algebraic prescription for the mixing length is no longer feasible. The way forward is to consider statements regarding the dynamics of turbulence. A useful method of analysing a turbulent flow regime is to consider the level of kinetic energy in the flow field which is analogous to the inertial forces leading to a high Reynolds number characteristic of turbulent flows. Kinetic energy in a turbulent flow interacts with the flow by inducing a turbulent chaotic behaviour. Similarly the flow field can act to dissipate this kinetic energy and hence dampen out this turbulent flow regime. This is the premise behind the $k - \varepsilon$ model, which focuses on the mechanisms that affect turbulent kinetic energy.

The instantaneous kinetic energy, k , of a turbulent flow can be viewed as the sum of the mean kinetic energy $K=1/2(U^2+V^2+W^2)$ and the turbulent kinetic energy $k'=1/2(\overline{u'^2}+\overline{v'^2}+\overline{w'^2})$. An equation for the mean kinetic energy K can be obtained by multiplying the $x -$ component of the Reynolds equation by U , the $y -$ component equation by V and the $z -$ component equation by W . By adding all of these results together, the time - average equation governing the mean kinetic energy of the flow can be established. Similarly an equation for the turbulent kinetic energy k can be obtained by multiplying each of the compressible Navier - Stokes equations by appropriate fluctuating velocity components e.g. the $x -$ component equation multiplied by u' etc. and addition of all the results, followed by a repeat of this process on the Reynolds equations, subtraction of the two resulting equations along with re-arrangement yields an equation for turbulent kinetic energy k . Both equations for the mean kinetic energy and turbulent kinetic energy are given as follows

$$\frac{\partial(\rho K)}{\partial t} + \text{div}(\rho K \mathbf{U}) = \text{div}\left(-P\mathbf{U} + 2\mu\mathbf{U}E_{ij} - \rho\mathbf{U}\overline{u'_i u'_j}\right) - 2\mu\overline{E_{ij} \cdot E_{ij}} - \rho\overline{u'_i u'_j} \cdot E_{ij} \quad (\text{A.17})$$

$$\frac{\partial(\rho k)}{\partial t} + \text{div}(\rho k \mathbf{U}) = \text{div}\left(-\overline{p' \mathbf{u}'} + 2\mu\overline{\mathbf{u}' e'_{ij}} - \rho \frac{1}{2}\overline{u'_i \cdot u'_i u'_j}\right) - 2\mu\overline{e'_{ij} \cdot e'_{ij}} + \rho\overline{u'_i u'_j} \cdot E_{ij} \quad (\text{A.18})$$

where the behaviour of each term in the two above equations can be viewed as:

$$\begin{array}{cccccc}
 \text{Rate of} & & \text{Transport} & & \text{Transport} & & \text{Transport} & & \text{Transport} \\
 \text{change} & + & \text{of K or k by} & = & \text{of K or k by} & + & \text{of K or k by} & + & \text{of K or k by} \\
 \text{of K or k} & & \text{convection} & & \text{pressure} & & \text{viscous stresses} & & \text{Reynolds stress} \\
 & & & & \text{Rate of} & & \text{Turbulence} & & \\
 & & & & \text{dissipation} & - & \text{production} & & \\
 & & & & \text{of K or k} & & \text{of K or k} & &
 \end{array}$$

These equations are similar to normal transport equations, however they do contain some significant extra terms whose function warrants discussion such as the turbulence production terms in both the mean and turbulent kinetic energy equations. As these terms are equal but opposite in sign, the turbulence production term hence destroys the mean kinetic flow energy, inducing turbulent flow behaviour. The viscous dissipation term $-2\mu\overline{e'_{ij}\cdot e'_{ij}}$ of the turbulent kinetic energy is caused by work done by the smallest eddies against viscous stresses. It leads to the rate of dissipation per unit mass, which is of vital importance in the study of turbulence dynamics and is denoted by

$$\varepsilon = 2\nu\overline{e'_{ij}\cdot e'_{ij}} \tag{A.19}$$

This term is always the main turbulent destruction term in the turbulent kinetic energy equation. It contains many unknown and immeasurable terms as follows

$$\varepsilon = 2\nu\overline{e'_{ij}\cdot e'_{ij}} = 2\nu\left(\overline{e'^2_{11}} + \overline{e'^2_{22}} + \overline{e'^2_{33}} + 2\overline{e'^2_{12}} + 2\overline{e'^2_{13}} + 2\overline{e'^2_{23}}\right) \tag{A.20}$$

A complete understanding of what, ε , the rate of dissipation per unit mass means can be obtained from analysis of the viscous dissipation term $-2\mu\overline{e'_{ij}\cdot e'_{ij}}$. It can be observed from the viscous dissipation term that if one concentrates solely on $\mu\cdot\overline{e'_{ij}}$, it can be seen that this product is always a viscous stress. As it is also understood that a viscous stress has a dissipative effect in a fluid flow, and as this product $\mu\cdot\overline{e'_{ij}}$ is multiplied by a further rate of decomposition to give $\mu\overline{e'_{ij}\cdot e'_{ij}}$, it can be deduced that the term has a viscous dissipative function within a turbulent fluid flow, and as such its effect is to reduce the turbulence of the flow.

Consequently due to the fact that ε is immeasurable, and that it is an important measure of the level to turbulent kinetic energy, the standard $k - \varepsilon$ model equations have been developed so as to have calculable model equations to determine ε and therefore k , based on an understanding of the relevant processes causing changes to these two variables, in that k is the turbulent kinetic energy in the flow and concurrently ε is rate at which this energy is dissipated.

In a similar manner to the mixing length model a velocity scale ϑ , and length scale ℓ , representative of the large scale turbulence, is defined in relation to k (m/s)² and ε (m²/s³) as $\vartheta = k^{1/2}$ (m/s) and $\ell = k^{3/2}/\varepsilon$ (m). The turbulent viscosity can be now specified as

$$\mu_t = C \rho \vartheta \ell = \rho C_\mu \frac{k^2}{\varepsilon} \quad (\text{A.21})$$

where C_μ is a newly introduced dimensionless constant. To compute values of k and ε the following standard modelled transport equations are used. It should be noted that the structure of each equation on the LHS follows conventional practice of transport equations.

$$\frac{\partial(\rho k)}{\partial t} + \text{div}(\rho k \mathbf{U}) = \text{div} \left[\frac{\mu_t}{\sigma_k} \text{grad } k \right] + 2\mu_t E_{ij} \cdot E_{ij} - \rho \varepsilon \quad (\text{A.22})$$

$$\frac{\partial(\rho \varepsilon)}{\partial t} + \text{div}(\rho \varepsilon \mathbf{U}) = \text{div} \left[\frac{\mu_t}{\sigma_\varepsilon} \text{grad } \varepsilon \right] + C_{1\varepsilon} \frac{\varepsilon}{k} 2\mu_t E_{ij} \cdot E_{ij} - C_{2\varepsilon} \rho \frac{\varepsilon^2}{k} \quad (\text{A.23})$$

However the RHS of both equations have been developed to be in their most usable form. Equations (A.22) and (A.18) are somewhat different but both describe the same transport of turbulent kinetic energy. Equations (A.22) and (A.23) are modelled from exact forms of their transport equations respectively. In words the two above equations obey familiar transport equation structure as follows

Rate of change of k or ε	+	Transport of k or ε by convection	=	Transport of k or ε by diffusion	+	Rate of production of k or ε
				-		Rate of destruction of k or ε

The inclusion of adjustable constants suffices to dampen out any discrepancies in the computed results.

Turbulent transport terms such as $div[(\mu_t/\sigma_k)grad k]$ in Equation (A.22) are representative of the transport terms of the scalar transport equation, where the ratios (μ_t/σ_k) and (μ_t/σ_ϵ) are an approach at stipulating values of the diffusivities of k and ϵ respectively, analogous to the dissipative viscosity terms necessary in the RANS equations. The form of these ratios can be justified as follows:

$$\text{Prandtl Number} = \frac{\text{kinematic viscosity}}{\text{thermal diffusivity}} = \frac{\nu}{k} \quad (\text{A.24})$$

similarly

$$\sigma_k = \frac{\text{turbulent viscosity}}{\text{turbulent kinetic energy diffusivity}} \quad (\text{A.25})$$

$$\text{turbulent kinetic energy diffusivity} = \frac{\mu_t}{\sigma_k}$$

As the pressure terms of the exact equations cannot be measured their effect is accounted for in both equations within the turbulent transport term. Significantly the immeasurable dissipation term $-2\mu\overline{e'_{ij} \cdot e'_{ij}}$ in the exact turbulent kinetic equation is accounted for with a tangible expression for the calculable mean kinetic energy dissipation $2\mu_t E_{ij} \cdot E_{ij}$ in Equation (A.17). The model equation for ϵ assumes that its production and destruction terms are proportional to the production and destruction terms of the model equation for k . Adoption of such forms of equations ensures that ϵ increases rapidly if k increases rapidly and that it decreases sufficiently fast to avoid non-physical negative values of turbulent kinetic energy if k decreases. To compute the Reynolds stresses with the $k - \epsilon$ model the following relationship is used

$$-\rho\overline{u'_i u'_j} = \mu_t \left(\frac{\partial U_i}{\partial x_j} + \frac{\partial U_j}{\partial x_i} \right) - \frac{2}{3} \rho k \delta_{ij}; \quad \delta_{ij} = \begin{cases} 1 & \text{if } i = j \\ 0 & \text{if } i \neq j \end{cases} \quad (\text{A.26})$$

The extra term on the RHS involving δ_{ij} serves to make the formula applicable to the normal Reynolds stresses for which $i = j$, i.e. $\tau_{xx}^R = -\rho\overline{u'^2}$, $\tau_{yy}^R = -\rho\overline{v'^2}$ and $\tau_{zz}^R = -\rho\overline{w'^2}$. Should an incompressible flow be considered along with only the first term of Equation (A.26), if all of the normal stresses are added together, the following is obtained with acknowledgment that the compressible continuity equation is equal to zero:

$$2\mu_t E_{ij} = 2\mu_t \left[\frac{\partial U}{\partial x} + \frac{\partial V}{\partial y} + \frac{\partial W}{\partial z} \right] = 2\mu_t \text{div}\mathbf{U} = 0 \quad (\text{A.27})$$

As this is certainly not the case for the three normal stresses it can be shown that the for any flow the sum of the normal Reynolds stresses is equal to minus twice the turbulence kinetic energy per unit volume as follows:

$$\text{Turbulent K.E.} = \frac{1}{2} \rho \mathbf{u}^2$$

$$\begin{aligned} \text{Turbulent K.E.} \\ \text{per unit volume} &= \frac{1}{2} \rho \mathbf{u}^2 = \frac{1}{2} \rho (\overline{u^2} + \overline{v^2} + \overline{w^2}) \end{aligned}$$

$$\begin{aligned} \text{Sum of normal} \\ \text{Reynolds stresses} &= -\rho (\overline{u^2} + \overline{v^2} + \overline{w^2}) \end{aligned}$$

Hence in Equation (A.26) an equal third of the turbulent kinetic energy is allocated to each normal stress component to ensure that the computed normal Reynolds stresses have a physically correct value.

Finally in the $k - \epsilon$ equations there are five adjustable constants, values of which have been arrived at by comprehensive data fitting for a wide range of turbulent flows:

$$C_\mu = 0.09; \sigma_k = 1.00; \sigma_\epsilon = 1.30; C_{1\epsilon} = 1.44; C_{2\epsilon} = 1.92$$

The advantages and disadvantages of this turbulence model are given below in Table A-2 from [32].

Advantages	Disadvantages
<ul style="list-style-type: none"> • Simplest turbulence model for which only initial and/or boundary conditions need to be supplied. • Excellent performance for many industrially relevant flows. • Well established; the most widely validated turbulence model 	<ul style="list-style-type: none"> • More expensive to implement than mixing length model due to two extra PDEs • Poor performance in a variety of important cases such as: <ol style="list-style-type: none"> 1. Some unconfined flows. 2. Flows with large extra strains e.g. swirling flows.

Table A-2: Advantages and disadvantages of the $k - \epsilon$ model [32].

A.3.4 The $k - \omega$ Model

Another two equation turbulence model is the $k - \omega$ model which involves a modified version of the k equation in the $k - \varepsilon$ model, and an inverse time scale associated with the turbulence, ω . The reasoning behind the formulation of this model is to close equations (A.26) and (A.22) further; this is in preference to using an equation for the turbulent viscosity based on dimensional reasoning with added adjustable constants such as in the mixing length and the $k - \varepsilon$ models equations (A.15) and (A.21). The basis of the theory of this model is from the fact that as k appears in the relationship given by equation (A.26) it is therefore plausible that $\nu_t \propto k$. As the dimensions of ν_t are $(\text{length})^2/(\text{time})$ while the dimensions of k are $(\text{length})^2/(\text{time})^2$, by dimensional reasoning a relationship between these terms is formed if a unit, in this case ω , of dimensions of $1/(\text{time})$ is introduced so that the kinematic turbulent viscosity can be calculated from

$$\nu_t = \frac{k}{\omega} \quad (\text{A.28})$$

An expression for ν_t is calculated by division of the two following equations for k and ω .

$$\frac{\partial \rho k}{\partial t} + U_j \frac{\partial \rho k}{\partial x_j} = \tau_{ij} \frac{\partial \rho U_i}{\partial x_j} - \beta^* \rho k \omega + \text{div} [(\mu + \sigma^* \mu_t) \text{grad } k] \quad (\text{A.29})$$

$$\frac{\partial \rho \omega}{\partial t} + U_j \frac{\partial \rho \omega}{\partial x_j} = \alpha \frac{\omega}{k} \tau_{ij} \frac{\partial \rho U_i}{\partial x_j} - \beta \rho \omega^2 + \text{div} [(\mu + \sigma \mu_t) \text{grad } \omega] \quad (\text{A.30})$$

Values for coefficients in the above equations are given as follows:

$$\begin{aligned} \alpha &= 0.52; \quad \beta = \beta_o f_\beta; \quad \beta^* = \beta_o^* f_\beta; \quad \sigma = 1/2; \quad \sigma^* = 1/2; \\ \beta_o &= 0.072; \quad f_\beta = \frac{1+70\chi_\omega}{1+80\chi_\omega}; \quad \chi_\omega \equiv \left| \frac{\Omega_{ij} \Omega_{jk} S_{ki}}{(\beta_o^* \omega)^3} \right|; \\ \beta_o^* &= 0.09; \quad f_{\beta^*} = \left\{ \begin{array}{ll} 1, & \chi_k \leq 0 \\ \frac{1+680\chi_k^2}{1+400\chi_k^2}, & \chi_k > 0 \end{array} \right\}; \quad \chi_k \equiv \frac{1}{\omega^3} \frac{\partial k}{\partial x_j} \frac{\partial \omega}{\partial x_j}; \\ \varepsilon &= \beta^* \omega k; \quad \ell = k^{1/2} / \omega \end{aligned}$$

where Ω_{ij} and S_{ij} are the mean – rotation and mean – strain – rate tensors, respectively defined by

$$\Omega_{ij} = \frac{1}{2} \left(\frac{\partial U_i}{\partial x_j} - \frac{\partial U_j}{\partial x_i} \right); S_{ij} = \frac{1}{2} \left(\frac{\partial U_i}{\partial x_j} + \frac{\partial U_j}{\partial x_i} \right) \quad (\text{A.31})$$

Once values for k and ω are known a value for the turbulent kinematic viscosity is obtained from Equation (A.28) along with the required Reynolds stresses from Equation (A.26) as normal. The advantages and disadvantages of this turbulence model are given below in Table A-3 from [32].

Advantages	Disadvantages
<ul style="list-style-type: none"> • Incorporates modifications for low Re number effects, compressibility, and shear flow spreading as in far wakes, mixing layers, and is thus applicable to wall-bounded flows and free shear flows 	<ul style="list-style-type: none"> • Suffers from some of the same drawbacks of the $k - \epsilon$ model such as the assumption that μ_t is isotropic. • Highly sensitive to ω specified in the free stream.

Table A-3: Advantages and disadvantages of the $k - \omega$ model [32].

A.3.5 SST Model by Menter

Menter [32], proposed that the $k - \omega$ model has a disadvantage of being highly sensitive to ω in the freestream. For this reason Menter has since proposed combining the $k - \omega$ model in the inner region of boundary layers and the standard $k - \epsilon$ model in the outer region of boundary layers and the free stream. The following transport equations for the Shear Stress Transport (SST) model are in fact dual transport equations for calculating values for k and ω from the $k - \omega$ model or the $k - \epsilon$ model transported to $k - \omega$ formulation, with use of a blending function F_1 which is designed to be one near and zero away from surfaces.

$$\frac{Dk}{Dt} = \frac{\tau_{ij}}{\rho} \frac{\partial U_i}{\partial x_j} + \frac{\partial}{\partial x_j} \left[(v + \sigma_k v_t) \frac{\partial k}{\partial x_j} \right] - \beta^* \omega k \quad (\text{A.32})$$

$$\frac{D\omega}{Dt} = \frac{\gamma}{\rho v_t} \tau_{ij} \frac{\partial U_i}{\partial x_j} + \frac{\partial}{\partial x_j} \left[(v + \sigma_\omega v_t) \frac{\partial \omega}{\partial x_j} \right] + 2(1 - F_1) \sigma_{\omega 2} \frac{1}{\omega} \frac{\partial k}{\partial x_j} \frac{\partial \omega}{\partial x_j} \quad (\text{A.33})$$

The inner constants given by

$$\sigma_{k1} = 0.85; \sigma_{\omega1} = 0.5; \beta_1 = 0.0750; \beta^* = 0.09$$

$$n = 0.41; \gamma_1 = \frac{\beta_1}{\beta^*} - \sigma_{\omega1} \frac{n^2}{\sqrt{\beta^*}}; a_1 = 0.31$$

and the outer constants given by

$$\sigma_{k2} = 1; \sigma_{\omega2} = 0.856; \beta_2 = 0.0828; \beta^* = 0.09$$

$$n = 0.41; \gamma_2 = \frac{\beta_2}{\beta^*} - \sigma_{\omega2} \frac{n^2}{\sqrt{\beta^*}}$$

The constants for the inner model ϕ_1 and outer model ϕ_2 , are mixed to give new usable constants ϕ using the blending function F_1 as follows

$$\phi = F_1\phi_1 + (1 - F_1)\phi_2 \quad (\text{A.34})$$

where

$$F_1 = \tanh(\arg_1^4)$$

$$\arg_1 = \min \left[\max \left(\frac{\sqrt{k}}{0.09\omega y}; \frac{500\nu}{y^2\omega} \right); \frac{4\sigma_{\omega2}k}{CD_{k\omega}y^2} \right] \quad (\text{A.35})$$

where y is the distance to the wall and

$$CD_{k\omega} = \max \left(2\sigma_{\omega2} \frac{1}{\omega} \frac{\partial k}{\partial x_j} \frac{\partial \omega}{\partial x_j}, 10^{-20} \right) \quad (\text{A.36})$$

Finally the turbulent kinetic viscosity for this turbulence model is defined as

$$\nu_t = \frac{a_1 k}{\max(a_1\omega; \Omega F_2)} \quad (\text{A.37})$$

where

$$F_2 = \tanh(\arg_2^2)$$

$$\arg_2 = \max \left(2 \frac{\sqrt{k}}{0.09\omega y}; \frac{500\nu}{y^2\omega} \right) \quad (\text{A.38})$$

This modified turbulent viscosity accounts for the transport of principal turbulent shear stresses, as a result of using either the $k - \epsilon$ or $k - \omega$ models depending on location within the flow field with use of the blending function in the SST model.

A.3.6 Reynolds Stress Equation Models

In addition to the RANS equations used as a basis for turbulence modelling theory, an additional equation can be obtained if moments of the compressible Navier – Stokes equations are taken. This is carried out by multiplying each term of the compressible Navier – Stokes equations independently by the fluctuating components, u'_i and u'_j , and taking a time average of the sum of the two respective products of each term in turn. The resulting equation for the transport of Reynold stresses in the form of $R_{ij} = -\tau_{ij}^R / \rho = \overline{u'_i u'_j}$ is

$$\frac{DR_{ij}}{Dt} = P_{ij} + D_{ij} - \varepsilon_{ij} + \Pi_{ij} + \Omega_{ij} \quad (\text{A.39})$$

where each term describes:

Rate of change of R_{ij}	+	Transport of R_{ij} by convection	=	Rate of production of R_{ij}	+	Transport of R_{ij} by diffusion	-	Rate of dissipation of R_{ij}
				Transport of R_{ij} due to + turbulent pressure-strain interactions	+	Transport of R_{ij} due to rotation		

The Reynolds stress equation comprises six partial differential equations, one each for the transport of the six independent Reynolds stresses, $\tau_{xx}^R = \overline{u_1'^2}$, $\tau_{yy}^R = \overline{u_2'^2}$, $\tau_{zz}^R = \overline{u_3'^2}$, $\tau_{xy}^R = \tau_{yx}^R = \overline{u_1' u_2'}$, $\tau_{xz}^R = \tau_{zx}^R = \overline{u_1' u_3'}$, $\tau_{yz}^R = \tau_{zy}^R = \overline{u_2' u_3'}$. Obviously this turbulence model does not need any isotropic assumptions of the turbulent viscosity, as was the basis of the two equation models. This model follows μ_t throughout the flow domain. The Reynolds stress equation model does not use exact forms of each term in the derivation of the Reynolds stress transport equation above; it incorporates simpler analogous forms of some of the RHS terms. However the production term can be given in its exact form, as terms contained within it are measurable.

$$P_{ij} = - \left(R_{im} \frac{\partial U_j}{\partial x_m} + R_{jm} \frac{\partial U_i}{\partial x_m} \right) \quad (\text{A.40})$$

The diffusion term is modelled by the assumption that the rate of transport of the Reynolds stresses by diffusion is proportional to the gradients of the Reynolds stresses as follows, similar to diffusion terms within the scalar transport equation:

$$D_{ij} = \frac{\partial}{\partial x_m} \left(\frac{v_t}{\sigma_k} \frac{\partial R_{ij}}{\partial x_m} \right) = \text{div} \left(\frac{v_t}{\sigma_k} \text{grad} (R_{ij}) \right) \quad (\text{A.41})$$

The dissipation rate is modelled by assuming isotropy of the small dissipative eddies, and it is set that it is affected by the normal Reynolds stresses only and in an equal measure.

$$\varepsilon_{ij} = \frac{2}{3} \varepsilon \delta_{ij}; \quad \delta_{ij} = \begin{cases} 1 & \text{if } i = j \\ 0 & \text{if } i \neq j \end{cases} \quad (\text{A.42})$$

where ε is the dissipation rate of turbulent kinetic energy as stated already by (A.19), hence

$$\varepsilon_{ij} = \frac{4}{3} \overline{v e'_{ij} \cdot e'_{ij}} \delta_{ij} \quad (\text{A.43})$$

As the dissipation rate, ε_{ij} , contains immeasurable fluctuating rate of deformation terms contained within the dissipation rate of turbulent kinetic energy ε , a further model equation is required for ε and this is simply given by equation (A.23) used within the $k - \varepsilon$ model.

The pressure-strain interactions constitute, at the same time, the most difficult term and the most important one to model accurately. Their effect on the Reynolds stresses is caused by two distinct processes: pressure fluctuations due to eddies interacting with each other and pressure fluctuations due to the interaction of an eddy with a region of flow of different mean velocity. The overall effect of the pressure-strain term is to re-distribute energy amongst the normal Reynolds stresses so as to make them more isotropic and to reduce the Reynolds shear stresses. A comprehensive model that accounts for all these effects is in the following form:

$$\Pi_{ij} = -C_1 \frac{\varepsilon}{k} \left(R_{ij} - \frac{2}{3} k \delta_{ij} \right) - C_2 \left(P_{ij} - \frac{2}{3} P \delta_{ij} \right) \quad (\text{A.44})$$

with $C_1 = 1.8$, $C_2 = 0.6$ and k , the turbulent kinetic energy, is calculated by adding the three normal Reynolds stresses together

$$k = \frac{1}{2}(R_{11} + R_{22} + R_{33}) = \frac{1}{2}(\overline{u_1^2} + \overline{u_2^2} + \overline{u_3^2}) \quad (\text{A.45})$$

The rotational term is given by

$$\Omega_{ij} = -2\omega_k (R_{jm}e_{ikm} + R_{im}e_{jkm})$$

$$e_{ijk} = \left\{ \begin{array}{l} 1 \text{ if } i \neq j \neq k \text{ and in cyclic order} \\ -1 \text{ if } i \neq j \neq k \text{ and in anti-cyclic order} \\ 0 \text{ if any two indices are the same} \end{array} \right\} \quad (\text{A.46})$$

where ω_k is a rotation vector about the k – plane i.e. the direction of rotation is about the k – plane. The advantages and disadvantages of this turbulence model are given below in Table A-4 from [32].

Advantages	Disadvantages
<ul style="list-style-type: none"> • Potentially the most general of all classical turbulence models • Only initial and/or boundary conditions need to be supplied • Very accurate calculation of mean flow properties and all Reynolds stresses for many simple and more complex flows. 	<ul style="list-style-type: none"> • Very large computing costs due to seven extra partial differential equations. • Not as widely validated as the mixing length and $k - \epsilon$ models. • Performs just as poorly as the $k - \epsilon$ model in some flows owing to identical problems with the ϵ-equation modelling.

Table A-4: Advantages and disadvantages of the Reynolds Stress Equation Model [32].

A.4 Summary

In this section the turbulence models introduced have been devised as a means of closing the RANS – Stokes equations, as these models allow for calculation of the Reynolds stresses. It was shown that the resulting mathematical expressions of turbulence models are quite complicated, and it should be noted that all the models contain adjustable constants a result of which any CFD calculations based on these models should never be accepted without any validation against experimental or theoretical results available. Apart from the main CFD study of the RHVT an additional report was submitted to the Department of Mechanical Engineering, Bolton St. This report was a preliminary validation of the ANSYS CFX 10 software and is included as follows in a study of flat plate boundary layers.

B CFD Analysis of Flat Plate Boundary Layers

B.1 Introduction

Before an analysis of the RHVT was conducted an additional report was submitted in order to demonstrate the authors proficiency in using and understanding the ANSYS CFX CFD package. An appropriate problem for which there is a theoretical solution in place was selected. The problem addressed was the classic example of boundary layer formation due to fluid flow over a flat – plate.

B.2 Boundary Layers

Boundary layers are a concept based on the idea to divide a fluid flow into two regions: an outer flow region that is inviscid and/or irrotational, and an inner flow region called a boundary layer. The boundary layer is a very thin region of flow near a solid wall where viscous forces and rotationality cannot be ignored.

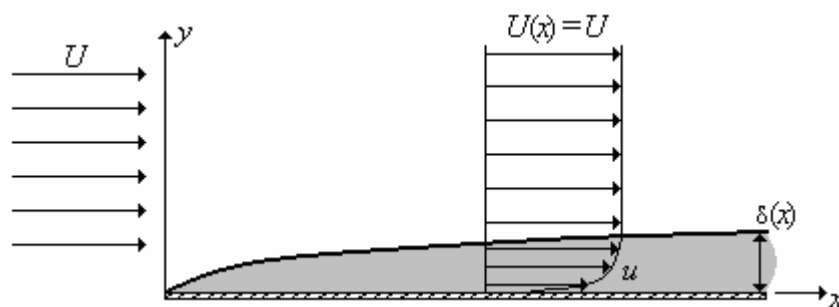


Fig. B-1: Boundary layer formation over a flat plate.

By convention the thickness, δ , of boundary layer formed at some location along the plate is usually defined as the distance away from the wall at which the velocity component parallel to the wall is 99% of the fluid speed outside the boundary layer. It turns out that for a given fluid and plate, the higher the free stream speed U , the thinner the boundary layer. The local Reynolds number for this flow is based on the distance x along the plate,

$$\text{Re}_x = \frac{\rho U x}{\mu} = \frac{U x}{\nu} \quad (\text{B.1})$$

As the flow moves along the plate to larger and larger values of x , Re_x increases linearly with x . At some point, infinitesimal disturbances in the flow begin to grow,

and the boundary layer cannot remain laminar and it begins a transition towards turbulent flow. In this case for a smooth flat plate with a uniform free stream, the transition process begins at a critical Reynolds number, $Re_{x, \text{critical}} \cong 1 \times 10^5$, and continues until the boundary layer is fully turbulent at the transition Reynolds number, $Re_{x, \text{transition}} \cong 3 \times 10^6$. In real – life engineering flows, transition to turbulent flow usually occurs more abruptly and much earlier than the values given for a smooth flat plate with a calm free stream. Factors such as roughness along the surface, free – stream disturbances, acoustic noise, flow unsteadiness, vibrations, and curvature of the wall contribute to an earlier transition location. Because of this, an engineering critical Reynolds number of $Re_{x, \text{cr}} \cong 5 \times 10^5$ is often used to determine whether a boundary layer is most likely laminar or most likely turbulent.

B.2.1 The Laminar Boundary Layer Equations

These boundary layer equations are derived from the Navier – Stokes equations with simplifications based on the significance and magnitude of each term contained within these equations. In order to quantify each of the terms both the x and y momentum equations are non-dimensionalised based on appropriate length and velocity scales within the boundary layer. The order of magnitude of each variable is:

$$u \approx U, P - P_\infty \approx \rho U^2, \frac{\partial}{\partial x} \approx \frac{1}{L}, \frac{\partial}{\partial y} \approx \frac{1}{\delta} \quad (\text{B.2})$$

where u and P are the axial velocity and pressure distribution within the boundary layer and where U , P_∞ and L are the free stream velocity and pressure and the length of the flat plate respectively. Applying the orders of magnitude in Equation (B.2) to the incompressible continuity equation in two dimensions we obtain an order of magnitude of the velocity component v as follows:

$$\begin{aligned} \frac{\partial u}{\partial x} + \frac{\partial v}{\partial y} = 0 \rightarrow \frac{U}{L} + \frac{v}{\delta} = 0 \\ v \approx \frac{U\delta}{L} \end{aligned} \quad (\text{B.3})$$

Since $\delta/L \ll 1$ in a boundary layer, therefore the velocity component v has a much smaller value than u within a boundary layer. The following non-dimensional variables within the boundary layer can now be stipulated

$$x^* = \frac{x}{L}, y^* = \frac{y}{\delta}, u^* = \frac{u}{U}, v^* = \frac{vL}{U\delta}, P^* = \frac{P - P_\infty}{\rho U^2} \quad (\text{B.4})$$

These non-dimensional variables are substituted into the y-momentum equation given below as follows:

$$\underbrace{u}_{\frac{\partial}{\partial x^*} \frac{v^* U \delta}{L^2}} \frac{\partial v}{\partial x} + \underbrace{v}_{\frac{v^* U \delta}{L} \frac{\partial}{\partial y^*} \frac{v^* U \delta}{L \delta}} \frac{\partial v}{\partial x} = - \underbrace{\frac{1}{\rho} \frac{\partial P}{\partial y}}_{\frac{1}{\rho} \frac{\partial P^* \rho U^2}{\partial y^*} \frac{1}{\delta}} + v \underbrace{\frac{\partial^2 v}{\partial x^2}}_{\frac{\partial^2 v^* U \delta}{\partial x^{*2} L^3}} + v \underbrace{\frac{\partial^2 v}{\partial x^2}}_{\frac{\partial^2 v^* U \delta}{\partial y^{*2} L \delta^2}}$$

which after rearrangement yields

$$u^* \frac{\partial v^*}{\partial x^*} + v^* \frac{\partial v^*}{\partial y^*} = - \left(\frac{L}{\delta} \right)^2 \frac{\partial P^*}{\partial y^*} + \left(\frac{v}{UL} \right) \frac{\partial^2 v^*}{\partial x^{*2}} + \left(\frac{v}{UL} \right) \left(\frac{L}{\delta} \right)^2 \frac{\partial^2 v^*}{\partial y^{*2}} \quad (\text{B.5})$$

It can be observed quite easily that the last two terms on the right hand side have negligible influence as $Re_L = UL/\nu \gg 1$, and therefore they can be neglected. Also since $L \gg \delta$, the pressure gradient term is of order of magnitude greater than the advective terms on the left of the equation, hence this pressure gradient is set to zero, and the non-dimensional y – momentum equation reduces to $\partial P^*/\partial y^* \cong 0$ or in terms of physical variables, the normal pressure gradient through a boundary layer

$$\partial P/\partial y \cong 0 \quad (\text{B.6})$$

And, therefore, while the pressure may vary along the wall in the x – direction, there is negligible change in pressure in the direction normal to the wall.

In the x – component of the momentum equation since P is not a function of y , $\partial P/\partial x$ can be replaced by dP/dx , and along with introduction of non-dimensional terms in a similar manner as was done with the y – component of the momentum equation, the x – component can be resolved to the following form

$$u \frac{\partial u}{\partial x} + v \frac{\partial u}{\partial y} = - \frac{1}{\rho} \frac{dP}{dx} + \nu \frac{\partial^2 u}{\partial y^2} \quad (\text{B.7})$$

Note that this time the last term on the RHS cannot be neglected as to do so would be neglect all viscous terms and the resulting equation would be a Euler inviscid equation. Furthermore as the pressure across the boundary layer is the same as that outside the boundary layer, i.e. $\partial P/\partial y \cong 0$, by applying the Bernoulli equation

$P/\rho + 0.5U^2$ to the outer flow region, and differentiating with respect to x , a relationship between the pressure gradient and the velocity gradient in the x – direction is obtained

$$\frac{1}{\rho} \frac{dP}{dx} = -U \frac{dU}{dx} \quad (\text{B.8})$$

This relationship results in the boundary layer equations for steady, incompressible, laminar flow in the xy – plane.

$$\begin{aligned} \frac{\partial u}{\partial x} + \frac{\partial v}{\partial y} &= 0 \\ u \frac{\partial u}{\partial x} + v \frac{\partial u}{\partial y} &= U \frac{dU}{dx} + \nu \frac{\partial^2 u}{\partial y^2} \end{aligned} \quad (\text{B.9})$$

However in laminar boundary layers over an infinitesimally thin semi – infinite flat plate, a uniform free stream U flows parallel to the flat plate. This outer fluid flow in the inviscid region outside the boundary layer, develops a very thin boundary layer along the wall, it is so thin that it has negligible effect on the outer flow in such a way that the velocity is of a constant value.

$$U(x) = V = \text{constant} \quad (\text{B.10})$$

When this is applied to the boundary layer equations it is easily seen that $dU/dx = 0$; which means that there is no pressure gradient term contained within the x – momentum boundary equation, which now becomes

$$\begin{aligned} \frac{\partial u}{\partial x} + \frac{\partial v}{\partial y} &= 0 \\ u \frac{\partial u}{\partial x} + v \frac{\partial u}{\partial y} &= \nu \frac{\partial^2 u}{\partial y^2} \end{aligned} \quad (\text{B.11})$$

The required four boundary conditions are as follows

$$\begin{aligned} u &= 0 \text{ at } y = 0 & u &= U \text{ as } y \rightarrow \infty \\ v &= 0 \text{ at } y = 0 & u &= U \text{ for all } y \text{ at } x = 0 \end{aligned} \quad (\text{B.12})$$

These boundary layer equations can be solved numerically using Blasius's assumption of similarity in that no matter how much one zooms in or out on a laminar boundary layer the same flow pattern is always observed. Blasius introduced a similarity variable η that combines independent variables x and y into one non-dimensional independent variable,

$$\eta = y\sqrt{\frac{U}{\nu x}} \tag{B.13}$$

and he solved for a non-dimensionalised form of the x – component of velocity,

$$f' = \frac{u}{U} = \text{function of } \eta \tag{B.14}$$

Subsequently from the Continuity Equation (B.11) an expression for the variation of the vertical velocity in the y-direction is obtained as follows [34]

$$\frac{v}{U} = \frac{1}{2}\sqrt{\frac{\nu}{Ux}}(\eta f' - f) \tag{B.15}$$

When Equations (B.13) and (B.14) are substituted into Equations (B.11), subject to the boundary conditions of Equation (B.12), ordinary differential equations for nondimensional speeds u/U and v/U are obtained using conventional Runge – Kutta numerical techniques, the results of which are shown in the table below

η	f	u/U	v/U	η	f	u/U	v/U
0.0	0.0000	0.0000	0.0000	1.8	0.5295	0.5748	0.0007
0.1	0.0017	0.0332	0.0000	2.0	0.6500	0.6298	0.0008
0.2	0.0066	0.0664	0.0000	2.2	0.7812	0.6813	0.0010
0.3	0.0149	0.0996	0.0000	2.4	0.9223	0.7290	0.0011
0.4	0.0266	0.1328	0.0000	2.6	1.0725	0.7725	0.0013
0.5	0.0415	0.1659	0.0001	2.8	1.2310	0.8115	0.0014
0.6	0.0597	0.1989	0.0001	3.0	1.3968	0.8460	0.0016
0.8	0.1061	0.2647	0.0001	3.5	1.8377	0.9130	0.0019
1.0	0.1656	0.3298	0.0002	4.0	2.3057	0.9555	0.0021
1.2	0.2380	0.3938	0.0003	4.5	2.7901	0.9795	0.0022
1.4	0.3230	0.4563	0.0004	5.0	3.2833	0.9915	0.0023

Table B-1: Solution of the Blasius laminar flat plate boundary layer in similarity variables.

Plots of the variation of the axial and vertical velocities versus the similarity variable are given in Fig. B-2, and are a useful reference when analysing the shape of the velocity distribution that is to be captured by ANSYS CFX 10.

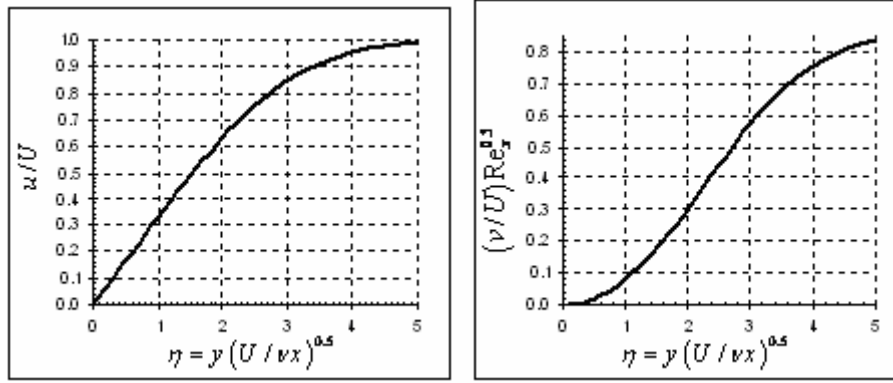


Fig. B-2: Axial and vertical velocity distributions versus Blasius similarity variable.

Another quantity of interest is a measure of the shear stress along the flat plate, as when any object moving through free stream it is the drag developed across this object that is of most importance i.e. it is the one of the major costs of propelling any object. This shear stress at the wall can be found quite easily from Newton’s law of viscosity

$$\tau_w = \mu \left. \frac{\partial u}{\partial y} \right|_{y=0} \tag{B.16}$$

A value for this can be obtained from derivation of the similarity results above in Table B.1, and finding that the slope at the wall is

$$\left. \frac{d(u/U)}{d\eta} \right|_{\eta=0} = f''(0) = 0.332 \tag{B.17}$$

Substitution of Equation (B.17) into Equation (B.16) along with transformation of similarity variables back to physical variables, obtains the shear stress as

$$\tau_w = 0.332 \frac{\rho U^2}{\sqrt{Re_x}} \tag{B.18}$$

Equation (B.18) can be non – dimensionalised by defining a skin friction coefficient which when intergrated gives a value for the total friction on a flatplate

$$C_{f,x} = \frac{\tau_w}{0.5\rho U^2} = \frac{0.664}{\sqrt{Re_x}} \tag{B.19}$$

It can be shown quite easily that by taking logs of both sides of Equation (B.19), this expression for the skin coefficient can be expressed on a graph as a straight line, as follows:

$$C_{f,x} = \frac{0.664}{\sqrt{\text{Re}_x}} = 0.664 \text{Re}_x^{-0.5}$$

$$\text{Log}(C_{f,x}) = \text{Log}(0.664 \text{Re}_x^{-0.5}) \quad (\text{B.20})$$

$$\text{Log}(C_{f,x}) = -0.5 \text{Log}(\text{Re}_x) + \text{Log}(0.664)$$

where this new expression for skin coefficient above in Equation (B.20) is of the form of the simple equation of a straight line, $y = mx + b$. A simplified expression for skin coefficient is computed and plotted in order to substantiate the results obtained, with ANSYS CFX 10, in Fig. B-17 and B-19, as we now know that logarithm of the skin coefficient of a flat plate boundary layer flow regime must vary proportionally to the logarithm of the Reynolds number of the same flow, by the following reduction of Equation B.20:

$$0.5 \text{Log}(C_{f,x}) = \text{Log}(\text{Re}_x) \quad (\text{B.21})$$

B.2.2 Turbulent Flat Plate Boundary Layer

Expressions for the boundary layer profile shape and other properties of the turbulent boundary layer are obtained empirically. Note that turbulent flows are inherently unsteady, and the instantaneous velocity profile shape varies with time. Thus all turbulent expressions discussed here represent time-averaged values. One common empirical approximation for the time-averaged velocity profile of a turbulent flat plate boundary layer is the one-seventh-power law

$$\begin{aligned}\frac{u}{U} &\cong \left(\frac{y}{\delta}\right)^{1/7} \quad \text{for } y \leq \delta, \\ \frac{u}{U} &= 1 \quad \text{for } y > \delta\end{aligned}\tag{B.20}$$

However the approximate turbulent boundary layer velocity profile shape of Equation (B.20) is not physically meaningful very close to the wall since it predicts that the slope is infinite at $y = 0$. This large slope at the wall leads to a very high wall shear stress and, therefore correspondingly high skin friction along the surface of the plate. Another common approximation is the log-law, a semi-empirical expression that is commonly expressed in a variable, non-dimensionalised by a characteristic velocity called the friction velocity, u_* , and it is as follows:

$$\frac{u}{u_*} = \frac{1}{\kappa} \ln \frac{yu_*}{\nu} + B\tag{B.21}$$

where κ and B are adjustable variables and were the friction velocity is given by:

$$u_* = \sqrt{\frac{\tau_w}{\rho}}\tag{B.22}$$

Unfortunately, the law suffers from the fact that it does not work very close to the wall as $\ln 0$ is undefined, and it also deviates from experimental values very close to the boundary layer edge. Nevertheless, it applies across nearly the entire turbulent flat plate boundary layer and is useful because it relates the velocity profile shape to the local value of wall shear stress through Equation (B.22). An expression that is valid all the way to the wall has been developed and is called after its originator, Spalding's law of the wall [37],

$$\frac{yu_*}{\nu} = \frac{u}{u_*} + e^{-\kappa B} \left[e^{\kappa(u/u_*)} - 1 - \kappa(u/u_*) - \frac{[\kappa(u/u_*)]^2}{2} - \frac{[\kappa(u/u_*)]^3}{6} \right] \quad (\text{B.23})$$

Usual values taken for κ and B are, $\kappa = 0.4$ to 0.41 and $B = 5.0$ to 5.5 . Instead of a physical plot with linear axes, a semi-log plot of non-dimensional variables is often drawn to magnify the near wall region; these variables are y^+ and u^+ , and are defined as follows

$$y^+ = \frac{yu_*}{\nu}; \quad u^+ = \frac{u}{u_*} \quad (\text{B.24})$$

A plot of Spalding’s law of the wall is shown below. The region very close to the wall $0 < y^+ < 5$ or 6 is called the viscous sub-layer. In this region, turbulent fluctuations are suppressed due to the close proximity of the wall, and the velocity profile is nearly linear, as can be seen in the region where u^+ and y^+ are equal.

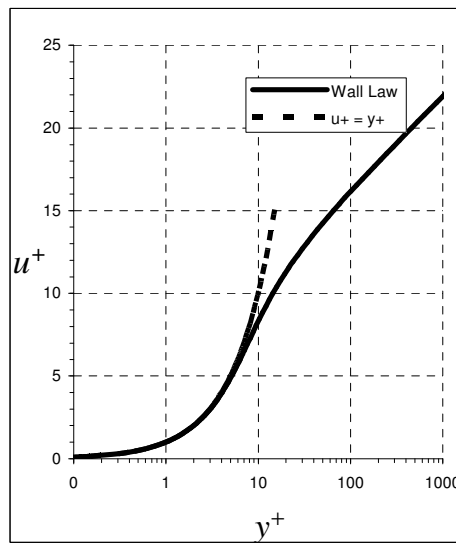


Fig. B-3: Spaldings law of the wall distribution.

B.3 CFD Solution

This CFD study of boundary layers began with drawing up the flow domain that will discretised into a mesh.

B.3.1 The Flow Domain

The flow domain setup and drawn for both the laminar and turbulent problems has been arrived at in such a way to mimic as closely as possible a two – dimensional

theoretical problem onto a three – dimensional flow regime. In order to achieve this, the dimensions of the flat plate have been stipulated as:

- 1m long
- 0.01m wide
- 0.2m fluid flow height.

The narrow width used is a direct result of not needing a wide domain for what is essentially a two – dimensional problem, and the fluid flow height is selected as a multiple of the maximum boundary thickness at the end of the plate, to compress effects such as accelerating the axial flow due to the boundary layer effectively creating a divergence in the flow. A basic illustration of this problem is given below.

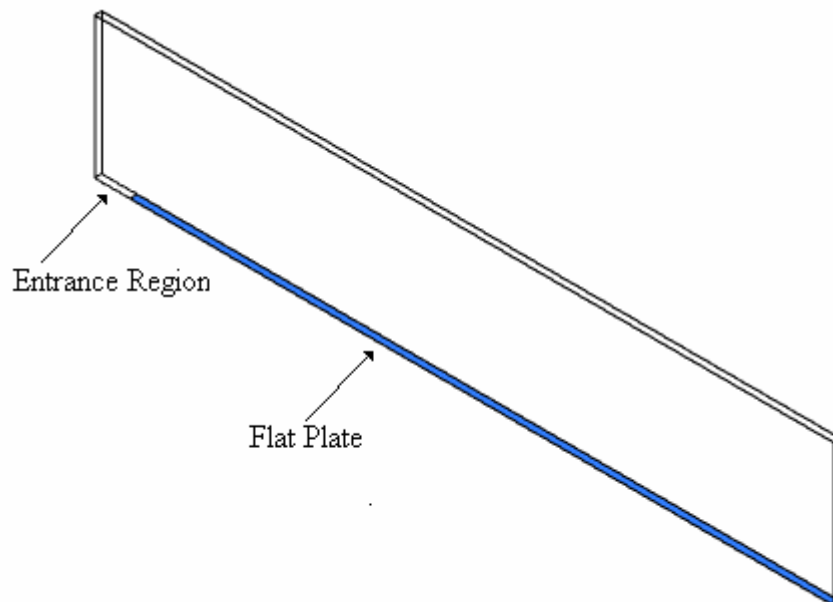


Fig. B-4: The flow domain.

The flat plate is shown highlighted as blue in the picture above, with an short entrance region included beforehand. The inlet and outlet are located perpendicular to the axial x-direction respectively. Two side faces are located perpendicular to the z-direction, and a completely inviscid region is located at uppermost face in the y-direction.

B.3.2 The Mesh

The meshes used in solving for the laminar and turbulent boundary layer profiles have been adapted from one set of solver results to the next so as to ensure that a refined inflationary layer growing from the flat plate and the entrance region fully covers the captured boundary layer as shown in the picture below. The inflationary layer can be seen as a logarithmic growth in cells from the flat plate up to the unstructured mesh as shown along with the boundary layer velocity contours leading to an inviscid region of constant velocity in red. Importantly the inflationary layer is quite dense at the flat plate, where for the panned out view it appears as a black line.

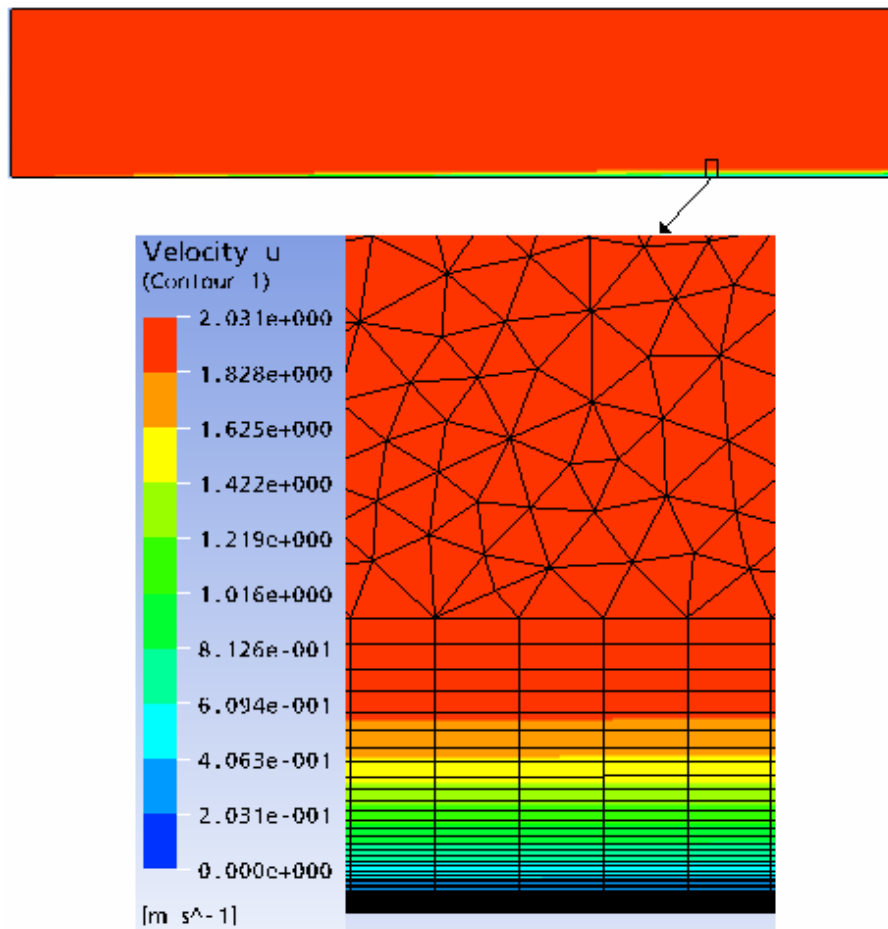


Fig. B-5: Close up of the final mesh for the laminar solution showing the inflationary layer and course inviscid region cells.

Shown overleaf are illustrations of just some of the meshes used, leading up to the final results for the laminar solution, in Fig. B-6, Fig. B-7, Fig. B-8 and Fig. B-9. Also shown overleaf is the final mesh used for the turbulent solution, as can be seen in Fig. B-10 and Fig. B-11.

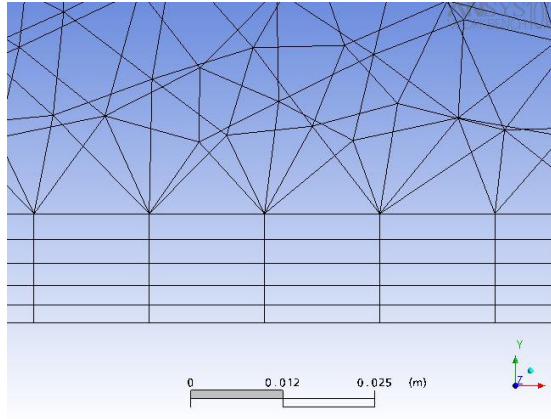


Fig. B-6: Inflation layer of the initial mesh used for the laminar solution. Total number of elements = 161560.

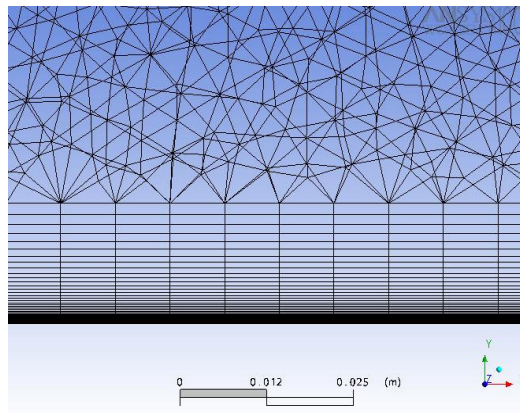


Fig. B-7: Inflation layer of an intermediate mesh used for the laminar solution. Total number of elements = 390076.

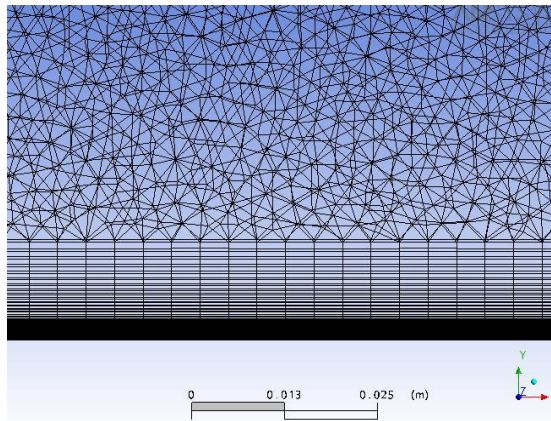


Fig. B-8: Inflation layer of the final mesh used for the laminar solution. Total number of elements = 882324.

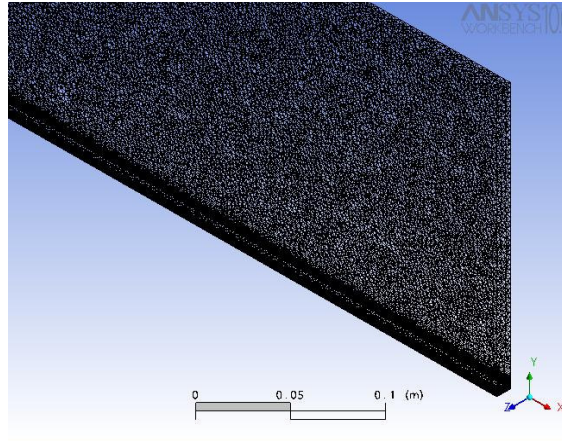


Fig. B-9: Panned out view of the final mesh, as an illustration of the density of elements required for a very accurate solution.

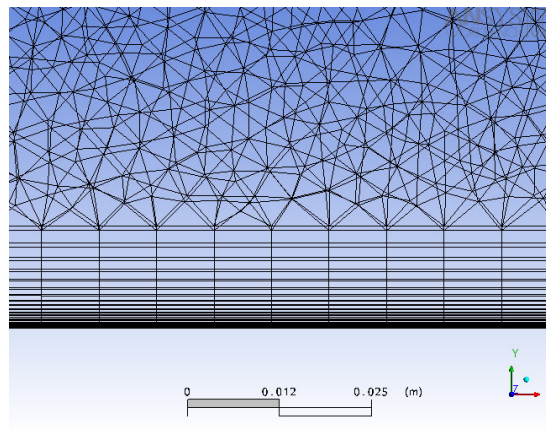


Fig. B-10: Inflation layer of the final mesh used for the turbulent solution. Total number of elements = 330538.

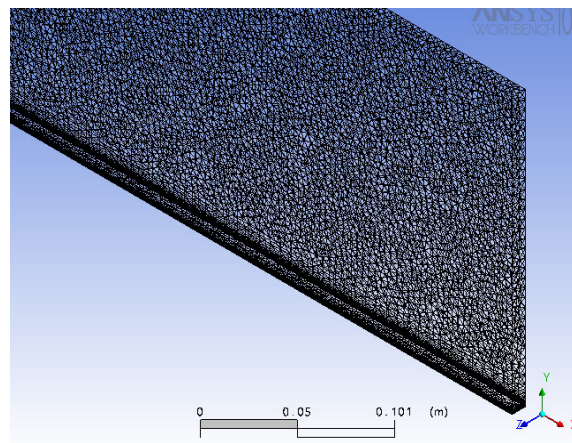


Fig. B-11: Panned out view of the final mesh used for the turbulent solution.

B.3.3 The Boundary Conditions

The boundary conditions specified for the laminar boundary layer problem follow criteria necessary so as to obtain a flow regime similar to the theoretical flow field specified for Blasius's solution above.

- The flat plate – at the flat plate a no – slip condition was selected.
- The inlet – at the inlet a constant velocity of 2m/s in the axial direction is used as the Reynolds number for this speed and plate length of 1m is,

$$\text{Re}_x = \frac{U_\infty L}{\nu} = \frac{2(1)}{1.516 * 10^{-5}} = 131926 \quad (\text{B.25})$$

which is quite a conservative choice for the velocity as transition to turbulent flow is said to occur at a critical Reynolds number, $\text{Re}_{critical} = 5 \times 10^5$.

- The outlet – the value of the relative static pressure is specified as 0atm gauge so as to ensure a theoretical zero pressure gradient in the axial direction as defined by Equation (B.11). In Ansys CFX 10 a reference static pressure for a flow domain from which all other pressure stipulations relate to must be specified. In this case the reference static pressure of 1atm was selected, and hence by specifying a relevant static pressure at the outlet of the flow of 0atm meant that the pressure there was no different than anywhere else within the flow.

- Symmetry boundary conditions – have been specified at the two side faces located at the lowest and highest displacement in the z-direction, and the small entrance region before the flat plate. A symmetry plane defines a plane of both geometric and flow symmetry, and as such it will not effect conditions of the flow field of the flow field in its vicinity.

- Inviscid region – initially the inviscid boundary located at the highest face in the vertical direction was first specified as being free slip and later had a free stream velocity equal to inlet velocity in order to not affect the flow in that region. However later on in the final solution, this boundary condition was specified as an outlet so as to improve the appearance of the constant axial velocity required, as can be seen in Fig. B-12 which focuses in on velocity contours in a very narrow bandwidth of 1.98m/s to 2.03m/s.

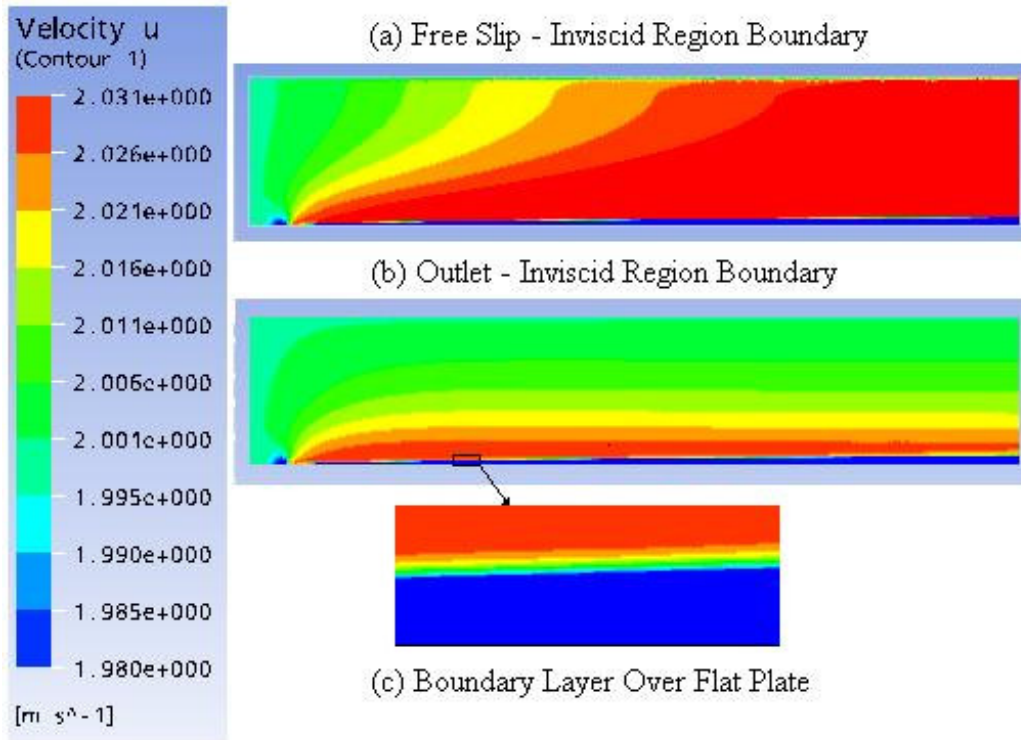


Fig. B-12: Axial velocity contours for a very narrow bandwidth of 1.98 to 2.031m/s for (a) free slip and (b) outlet, inviscid region boundary conditions.

The maximum value of axial velocity is 2.03m/s and is a result of channelling effects of the flow within the flow domain. Theoretically the only way of eliminating this slight inaccuracy is to make the domain infinitely long in the vertical y-direction. This is due to the large displacement effect caused by viscosity and the no – slip condition. In essence the flow velocity near the plate is so small the rest of the flow sees it as a blockage around which the flow must be diverted and hence accelerate as an overshoot in the axial velocity.

The same boundary conditions have been used for the turbulent solution except for one obvious notable exception for the inlet boundary condition.

- The Inlet – At the inlet a constant velocity of 15m/s in the axial direction is used as the Reynolds number for this speed and plate length of 1m is,

$$Re_x = \frac{UL}{\nu} = \frac{15(1)}{1.516 \cdot 10^{-5}} \approx 1,000,000 \tag{B.26}$$

which is well above the transition region, Re_x criteria.

The turbulence model selected was the Shear Stress Transport model, with an additional wall function chosen so as to ensure that the viscous sub – layer was captured. This model was picked in preference to the $k-\epsilon$ model as there is no facility within ANSYS CFX 10 for the $k-\epsilon$ model to cater for the viscous sub – layer due to a

requirement of highly refined near-wall grid resolution. Such an approach according to ANSYS CFX 10 literature often leads to numerical instability.

B.3.4 Convergence

When studying the results of one mesh refinement to the next, for the laminar solution, it was observed that the axial velocity varied little, whereas the vertical velocity changed more substantially between these refinements. However velocity distribution plots offered only a visual analysis of how well the solution had converged, a value of the wall shear stress at a particular location offered a numerical analysis of convergence. The wall shear stress near the end of the plate at $x=0.9\text{m}$ was selected, as from Equation (B.18) it can be seen that the value of the wall shear decays to the power of $\frac{1}{2}$ along the plate length, so its smallest and hence hardest to capture value was at the rear of the plate.

$$\begin{aligned}\tau_w &= 0.332 \frac{\rho U^2}{\sqrt{\text{Re}_x}} = 0.332 \frac{\rho_{air} U^2}{\sqrt{\frac{Ux}{\nu_{air}}}} \\ &= 0.332 \frac{1.204(2^2)}{\sqrt{\frac{2(0.9)}{1.516 \times 10^{-5}}}} = 0.00464 \text{ Pa}\end{aligned}\tag{B.27}$$

The results of the problem have been accepted to be quite close to the most accurate solution as possible. Convergence of the solution was accepted when the shear stress at the specified location remained constant to four decimal places from one mesh refinement to the next. Values of the wall shear stress at 0.9m along the plate varied from 0.005142 (Pa) to 0.004678 (Pa) using $5,000$ and $600,000$ elements respectively. The reason for such a substantial increase in elements was due to refining the inflation layer to capture all of the boundary layer and also by increasing the number of cells within the inflation layer to as high a value as possible to have as accurate a solution for the vertical velocity distribution as possible.

An additional judgement of how well the solution has converged within ANSYS CFX 10 numerical solver is obtained from the residual plot outputted from the solver during its run. The residual plots in Fig. B-13 and Fig. B-14 show the residuals of each calculated variable throughout the domain normalised for the purpose of monitoring the solution and setting convergence criteria. As can be seen overleaf the laminar solution is highly converged with a residual target of $1.00\text{E}-07$,

compared to $1.00E-05$ for the turbulent solution, the main reason for this was to capture the laminar axial velocity distribution. Less emphasis was given to judging the convergence of the turbulent solution as accurate results were obtained relatively easily compared to the laminar solution, with significantly less cells and run – times. Speculating as to a potential reason for this, it could be accepted that the developers of the ANSYS CFX 10 package focused the meshing and solver components of the software to solve for more prevailing turbulent flow problems in the most efficient manner achievable to the detriment of potential laminar solutions.

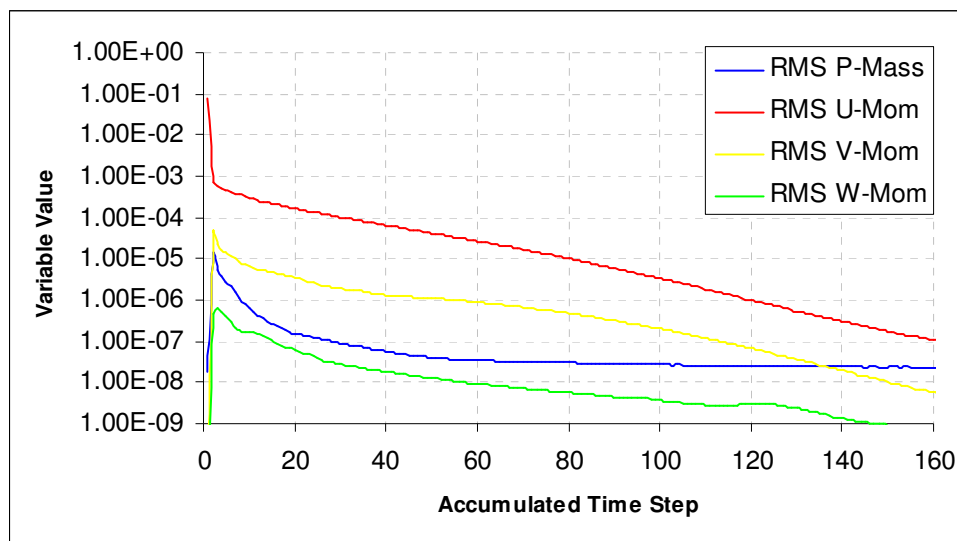


Fig. B-13: Residual plot of mass and velocity components for the final laminar solution.

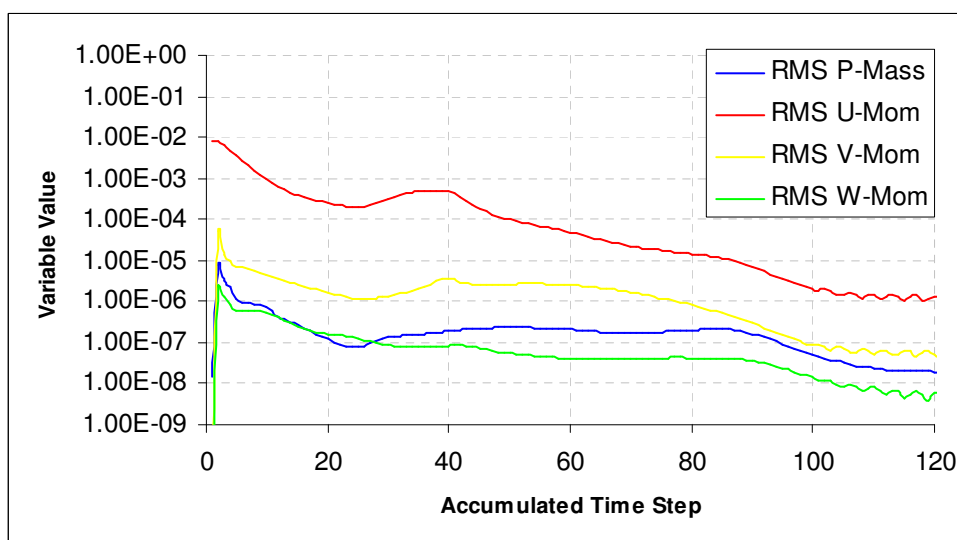


Fig. B-14: Residual plot of mass and velocity components for the final turbulent solution.

B.4 The Results

The plotted results have been non-dimensionalised to allow comparison with the theoretical solutions regardless of axial location along the flat plate. In the figures below the CFD predictions compare very well to the theoretical solutions. The turbulent solution of u^+ against y^+ appear to be distorted from the theoretical solution as boundary layer approaches the free stream. However these results are accurate as the theoretical solution does not take into account that the u^+ values are limited by the constant velocity in the free stream.

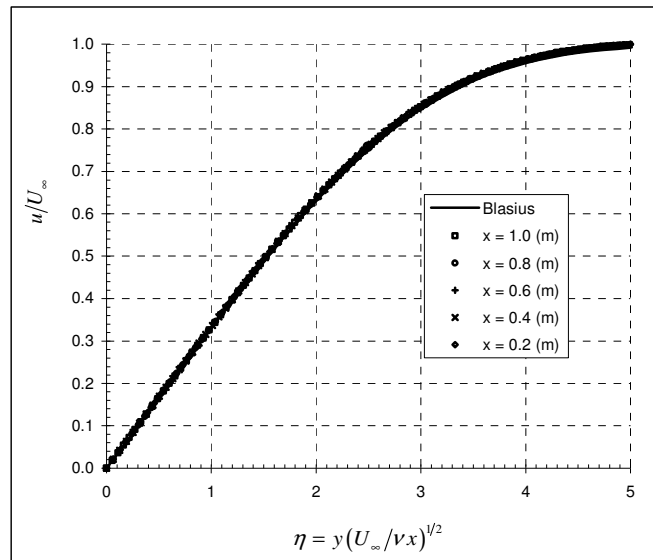


Fig. B-15: Comparison of computed axial velocity profiles with Blasius theoretical profile for laminar flow over a flat plate.

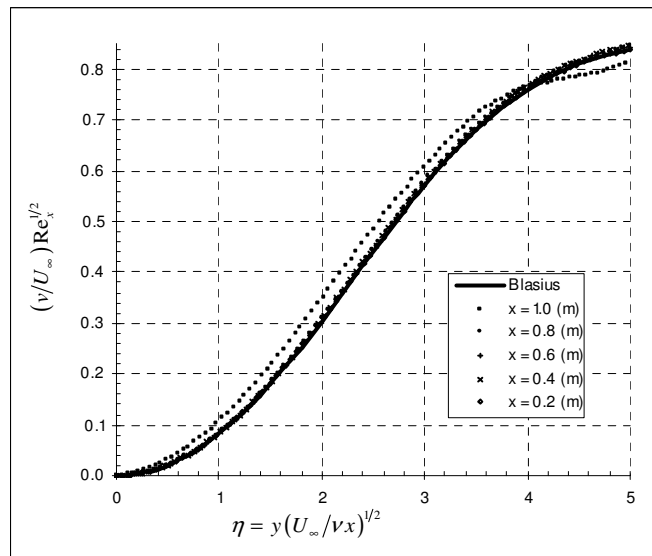


Fig. B-16: Comparison of computed vertical velocity profiles with Blasius theoretical profile for laminar flow over a flat plate.

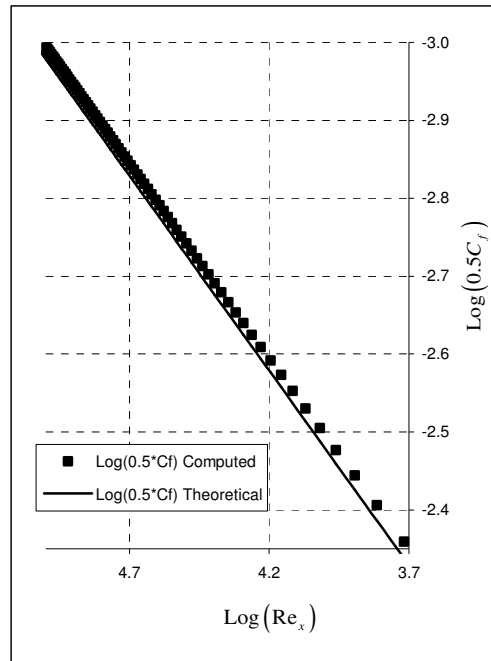


Fig. B-17: Comparison of the computed skin friction coefficient with the theoretical solution for laminar flow over a flat plate.

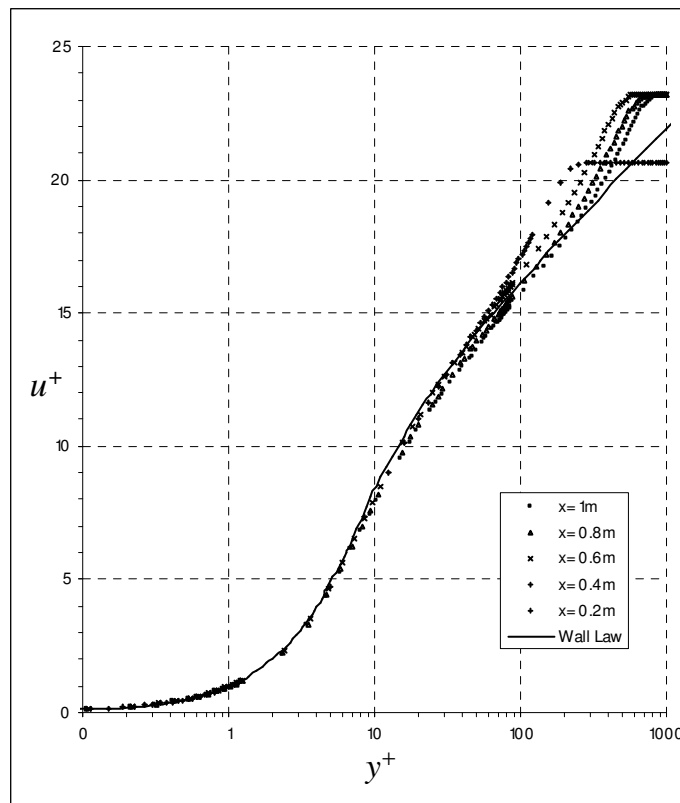


Fig. B-18: Comparison of computed axial velocity profiles with Spalding's law of the wall solution for turbulent flow over a flat plate.

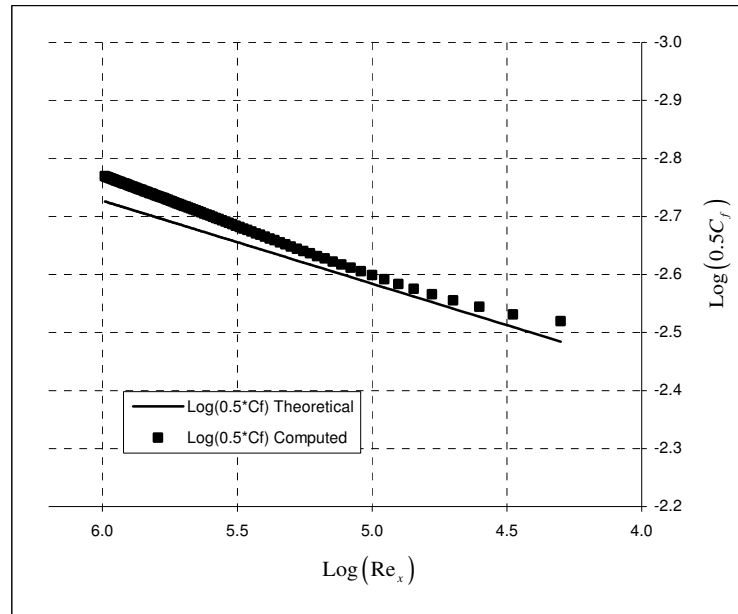


Fig. B-19: Comparison of the computed skin friction coefficient with the theoretical solution for turbulent flow over a flat plate.

B.5 Summary

Overall the results shown above are very successful and the set – out objective of demonstrating the authors ability of using the ANSYS CFX 10 package accurately and efficiently have clearly been achieved.

C Solver Output File for Mesh No. 2

C.1 Introduction

Included below is a summary of the parameters, including the boundary conditions, turbulence model and convergence criteria, specified in the ANSYS CFX 10 – Physics Pre-Processor module and as run within the ANSYS CFX 10 – Solver as follows:

This run of the CFX-10.0 Solver started at 11:51:56 on 9 Jan 2007 by user ronan.oliver

Setting up CFX-5 Solver run ...

LIBRARY:

MATERIAL: Air Ideal Gas

Material Description = Air Ideal Gas (constant Cp)

Material Group = Air Data, Calorically Perfect Ideal Gases

Option = Pure Substance

Thermodynamic State = Gas

PROPERTIES:

Option = General Material

ABSORPTION COEFFICIENT:

Absorption Coefficient = 0.01 [m⁻¹]

Option = Value

DYNAMIC VISCOSITY:

Dynamic Viscosity = 1.831E-05 [kg m⁻¹ s⁻¹]

Option = Value

EQUATION OF STATE:

Molar Mass = 28.96 [kg kmol⁻¹]

Option = Ideal Gas

SPECIFIC HEAT CAPACITY:

Option = Value

Reference Pressure = 1 [atm]

Reference Specific Enthalpy = 0. [J/kg]

Reference Specific Entropy = 0. [J/kg/K]

Reference Temperature = 25 [C]

Specific Heat Capacity = 1.0044E+03 [J kg⁻¹ K⁻¹]

Specific Heat Type = Constant Pressure

THERMAL CONDUCTIVITY:

Option = Value

Thermal Conductivity = $2.61\text{E-}2$ [W m⁻¹ K⁻¹]

RUN DEFINITION:

Definition File = D:/My Documents/RHVT/mesh2_001.def

Initial Values File = D:/My Documents/RHVT/mesh1_001.res

Interpolate Initial Values = On

Run Mode = Full

FLOW:

DOMAIN: RHVT

Domain Type = Fluid

Fluids List = Air Ideal Gas

BOUNDARY: Cold Outlet

Boundary Type = OUTLET

Location = Cold Outlet

BOUNDARY CONDITIONS:

FLOW REGIME:

Option = Subsonic

MASS AND MOMENTUM:

Option = Static Pressure

Relative Pressure = 0 [Pa]

BOUNDARY: Hot Outlet

Boundary Type = OUTLET

Location = Hot Outlet

BOUNDARY CONDITIONS:

FLOW REGIME:

Option = Subsonic

MASS AND MOMENTUM:

Option = Static Pressure

Relative Pressure = 50000 [Pa]

BOUNDARY: Inlet Nozzle

Boundary Type = INLET

Location = Inlet Nozzle

BOUNDARY CONDITIONS:

FLOW DIRECTION:

Option = Zero Gradient

FLOW REGIME:

Option = Subsonic

HEAT TRANSFER:

Option = Total Temperature

```
Total Temperature = 296.5 [K]
MASS AND MOMENTUM:
  Option = Static Pressure
  Relative Pressure = 2 [bar]
TURBULENCE:
  Option = Medium Intensity and Eddy Viscosity Ratio
BOUNDARY: Periodic Side 1
  Boundary Type = INTERFACE
  Location = Periodic Side 1
BOUNDARY CONDITIONS:
  HEAT TRANSFER:
    Option = Conservative Interface Flux
  MASS AND MOMENTUM:
    Option = Conservative Interface Flux
  TURBULENCE:
    Option = Conservative Interface Flux
BOUNDARY: Periodic Side 2
  Boundary Type = INTERFACE
  Location = Periodic Side 2
BOUNDARY CONDITIONS:
  HEAT TRANSFER:
    Option = Conservative Interface Flux
  MASS AND MOMENTUM:
    Option = Conservative Interface Flux
  TURBULENCE:
    Option = Conservative Interface Flux
BOUNDARY: RHVT Wall
  Boundary Type = WALL
  Location = RHVT Wall
BOUNDARY CONDITIONS:
  HEAT TRANSFER:
    Option = Adiabatic
  WALL INFLUENCE ON FLOW:
    Option = No Slip
  WALL ROUGHNESS:
    Option = Smooth Wall
DOMAIN MODELS:
  BUOYANCY MODEL:
    Option = Non Buoyant
DOMAIN MOTION:
  Option = Stationary
```

REFERENCE PRESSURE:
Reference Pressure = 1 [atm]

FLUID MODELS:

COMBUSTION MODEL:
Option = None

HEAT TRANSFER MODEL:
Include Viscous Work Term = On
Option = Total Energy

THERMAL RADIATION MODEL:
Option = None

TURBULENCE MODEL:
Option = k epsilon

TURBULENT WALL FUNCTIONS:
Option = Scalable

DOMAIN INTERFACE: Periodic
Boundary List1 = Periodic Side 1
Boundary List2 = Periodic Side 2
Connection Type = Automatic
Interface Type = Periodic
Periodic Type = Rotational

AXIS DEFINITION:
Option = Coordinate Axis
Rotation Axis = Coord 0.1

OUTPUT CONTROL:

RESULTS:
File Compression Level = Default
Option = Standard

SIMULATION TYPE:
Option = Steady State

SOLUTION UNITS:
Angle Units = [rad]
Length Units = [m]
Mass Units = [kg]
Solid Angle Units = [sr]
Temperature Units = [K]
Time Units = [s]

SOLVER CONTROL:

ADVECTION SCHEME:
Option = Upwind

CONVERGENCE CONTROL:
Length Scale Option = Conservative

```

Maximum Number of Iterations = 10000
Timescale Control = Auto Timescale
CONVERGENCE CRITERIA:
  Residual Target = 1e-05
  Residual Type = MAX
DYNAMIC MODEL CONTROL:
  Global Dynamic Model Control = On
Starting Interpolation onto different mesh:

```

```

25.0% complete
50.0% complete
75.0% complete
100.0% complete

```

```

+-----+
|                               Job Information                               |
+-----+

```

```

Run mode:      serial run

Host computer: CPL1ST-ROLIVER
Job started:   Tue Jan  9 11:52:23 2007

```

```

+-----+
| Memory Allocated for Run (Actual usage may be less) |
+-----+

```

Data Type	Kwords	Words/Node	Words/Elem	Kbytes	Bytes/Node
Real	32881.6	382.95	73.93	128443.7	1531.82
Integer	14170.3	165.03	31.86	55352.7	660.14
Character	2336.2	27.21	5.25	2281.4	27.21
Logical	40.0	0.47	0.09	156.2	1.86
Double	608.0	7.08	1.37	4750.0	56.65

```

+-----+
| Total Number of Nodes, Elements, and Faces |
+-----+

```

Domain Name : VT

```

Total Number of Nodes           =      85863
Total Number of Elements        =     444770

```

Total Number of Tetrahedrons = 444770
 Total Number of Faces = 39182

```

+-----+
|           The Equations Solved in This Calculation           |
+-----+
    
```

Subsystem : Momentum and Mass

U-Mom
 V-Mom
 W-Mom
 P-Mass

Subsystem : Heat Transfer

H-Energy

Subsystem : TurbKE and Diss.K

K-TurbKE
 E-Diss.K

CFD Solver started: Tue Jan 9 11:52:33 2007

```

+-----+
|           Convergence History           |
+-----+
    
```

=====

OUTER LOOP ITERATION = 1 CPU SECONDS = 6.391E+00

```

+-----+
| Equation | Rate | RMS Res | Max Res | Linear Solution |
+-----+
| U-Mom    | 0.00 | 3.2E-03 | 6.8E-02 | 3.3E-03 OK |
| V-Mom    | 0.00 | 3.0E-03 | 1.5E-01 | 2.6E-03 OK |
| W-Mom    | 0.00 | 3.4E-03 | 2.0E-01 | 2.8E-03 OK |
| P-Mass   | 0.00 | 3.4E-03 | 1.7E-01 | 8.5 1.1E-02 OK |
+-----+
| H-Energy | 0.00 | 3.0E-03 | 1.4E-01 | 5.4 5.6E-03 OK |
+-----+
| K-TurbKE | 0.00 | 1.2E-02 | 2.4E-01 | 5.4 1.4E-03 OK |
| E-Diss.K | 0.00 | 2.0E-02 | 8.1E-01 | 8.0 2.8E-04 OK |
    
```

=====

OUTER LOOP ITERATION = 2 CPU SECONDS = 5.031E+01

Equation	Rate	RMS Res	Max Res	Linear Solution
U-Mom	0.70	2.2E-03	4.6E-02	3.9E-03 OK
V-Mom	0.55	1.7E-03	5.5E-02	3.6E-03 OK
W-Mom	0.53	1.8E-03	7.3E-02	4.3E-03 OK
P-Mass	0.35	1.2E-03	1.0E-01	8.5 8.2E-03 OK
H-Energy	0.54	1.6E-03	1.1E-01	5.4 9.7E-03 OK
K-TurbKE	0.35	4.2E-03	6.9E-02	5.4 2.0E-03 OK
E-Diss.K	0.10	2.1E-03	6.5E-02	8.0 4.4E-04 OK

=====

OUTER LOOP ITERATION = 850 CPU SECONDS = 3.533E+04

Equation	Rate	RMS Res	Max Res	Linear Solution
U-Mom	1.00	4.0E-08	2.4E-06	6.4E-04 OK
V-Mom	1.00	4.5E-08	1.6E-06	4.4E-04 OK
W-Mom	1.00	4.0E-08	4.8E-07	5.3E-04 OK
P-Mass	1.00	7.4E-09	8.4E-08	8.5 1.4E-03 OK
H-Energy	0.99	1.2E-07	1.2E-05	5.4 1.8E-03 OK
K-TurbKE	1.00	7.0E-07	5.5E-05	5.4 5.0E-05 OK
E-Diss.K	1.00	3.2E-07	3.1E-05	8.0 2.9E-06 OK

```
=====
OUTER LOOP ITERATION = 851                      CPU SECONDS = 3.537E+04
```

```
-----
```

Equation	Rate	RMS Res	Max Res	Linear Solution
U-Mom	0.98	3.9E-08	1.5E-06	6.7E-04 OK
V-Mom	1.01	4.5E-08	1.3E-06	4.4E-04 OK
W-Mom	1.02	4.0E-08	7.3E-07	5.2E-04 OK
P-Mass	1.01	7.4E-09	9.6E-08	8.5 1.4E-03 OK
H-Energy	0.99	1.2E-07	1.2E-05	5.4 2.0E-03 OK
K-TurbKE	1.00	7.0E-07	5.5E-05	5.4 5.0E-05 OK
E-Diss.K	1.00	3.2E-07	3.1E-05	8.0 2.9E-06 OK

```
-----
```

```
=====
OUTER LOOP ITERATION = 852                      CPU SECONDS = 3.541E+04
```

```
-----
```

Equation	Rate	RMS Res	Max Res	Linear Solution
U-Mom	1.00	3.9E-08	1.6E-06	5.9E-04 OK
V-Mom	1.00	4.5E-08	1.2E-06	3.8E-04 OK
W-Mom	0.98	4.0E-08	6.5E-07	4.5E-04 OK
P-Mass	0.99	7.4E-09	1.1E-07	8.5 1.4E-03 OK
H-Energy	0.99	1.2E-07	1.2E-05	5.4 2.4E-03 OK
K-TurbKE	1.00	7.0E-07	5.5E-05	5.4 5.0E-05 OK
E-Diss.K	1.00	3.2E-07	3.1E-05	8.0 2.9E-06 OK

```
-----
```

```
=====
OUTER LOOP ITERATION = 853                      CPU SECONDS = 3.545E+04
-----
```

Equation	Rate	RMS Res	Max Res	Linear Solution
U-Mom	1.00	3.9E-08	1.7E-06	6.3E-04 OK
V-Mom	0.99	4.5E-08	1.4E-06	4.5E-04 OK
W-Mom	1.00	4.0E-08	9.5E-07	6.5E-04 OK
P-Mass	1.01	7.4E-09	8.4E-08	8.5 1.4E-03 OK
H-Energy	0.97	1.2E-07	8.6E-06	5.4 1.7E-03 OK
K-TurbKE	1.00	7.0E-07	5.5E-05	5.4 5.0E-05 OK
E-Diss.K	1.00	3.2E-07	3.1E-05	8.0 3.0E-06 OK

CFD Solver finished: Tue Jan 9 21:48:19 2007

CFD Solver wall clock seconds: 3.5746E+04

Execution terminating:

all maximum residual AND global imbalances
are below their target criteria.

```
-----
|                               Job Information                               |
-----
```

Host computer: CPL1ST-ROLIVER

Job finished: Tue Jan 9 21:48:31 2007

Total CPU time: 3.550E+04 seconds

```
or: (          0:          9:          51:    39.312 )
     (    Days:    Hours:    Minutes:    Seconds )
```

End of solution stage.

This run of the CFX-5 Solver has finished.